

Synthesis and characterization of nanostructures for catalysis



Candidate:
Alessandra Santini

Supervisor: Prof. Antonio Miotello
Co-supervisor: Dott. Nainesh Patel

Department of Physics
Universita' degli Studi di Trento

A thesis submitted for the degree of
Doctor of Philosophy in Physics

December 2012

Abstract

Catalysts are of great importance in many different fields, including the energy and the environmental sectors. It is important to produce them with simple preparation technique and to enhance the catalysts surface-to-volume ratio. The work undertaken in this thesis concerns the synthesis of nanostructures by Pulsed Laser Deposition (PLD) and R.F. sputtering deposition and the tailoring of their structures by varying deposition parameters. We synthesized Cobalt oxide nanoparticles (NPs) by PLD and studied the influence of the deposition parameters (i.e. substrate temperature, target-to-substrate distance and partial pressure of Oxygen in the chamber) on the final structure and crystalline phase of the NPs. The deposited NPs can be divided in two main categories: small NPs having a diameter of about 5 nm, and big NPs of size ranging from 50 to 400 nm. Depending on the value chosen for the deposition parameters, small NPs have CoO- or Co_3O_4 crystalline phase, and NPs can have a core/shell structure. The phase composition of the core and of the shell also vary according to the deposition conditions. We synthesized thin film of Co-B NPs by PLD. Depending on the energy density, the laser process is able to produce well-dispersed spherical Co NPs partially embedded within B-based film matrix in a single-step deposition. The small size, the polycrystalline nature of Co NPs, and the presence of Boron matrix is important for catalytic performance of the Co-B film. The catalytic activity of the Co-B has been tested in hydrolysis of chemical hydrides (ammonia borane and sodium borohydride). PLD deposition of C-film, to serve as support for Co-B NPs, was performed at different Ar pressures (from 10 to 50 Pa) to tailor film roughness in order to investigate the role of porous and irregular C-surface on supporting Co-B NPs acting as catalysts. The measured hydrogen generation rate attained with C-supported Co-B catalyst film is

higher than both unsupported-Co-B film and conventional Co-B powder. Multilayer ITO/Cr-doped- TiO_2 thin films have been synthesized by radio-frequency magnetron sputtering in order to sensitize TiO_2 in visible light and to lower the charge recombination rate in the Cr-doped- TiO_2 . When the multilayer films were exposed to visible light, we observed that the photocurrent increases as function of the number of bilayers by reaching the maximum with 6-bilayers of ITO/Cr-doped- TiO_2 . The superior photocatalytic efficiency of the 6-bilayers film implies higher hydrogen production rate through water-splitting.

Spontaneous growth of Lead nanowires (NWs) have been observed in composite Al-Pb film deposited by R.F. sputtering deposition. The parameters of deposition and the storage of the Al-Pb films after deposition has been changed in order to understand the growth process of NWs. Evolution of NWs growth was also observed inside a SEM chamber. We propose that a stress-driven mechanism and the corrosion occurring on the films surface in environment atmosphere are the cause of NWs growth.

Contents

List of Figures	v
List of Tables	xi
1 Introduction on nanomaterials	1
1.1 Overview of the thesis	2
1.2 What are nanomaterials?	3
1.3 Properties of nanomaterials	4
1.4 Synthesis of nanomaterials	5
1.4.1 Vapor processing synthesis of nanoparticle	6
1.4.1.1 Chemical Vapor Condensation (CVC)	6
1.4.1.2 Arc Discharge Method	6
1.4.1.3 Laser Pyrolysis	7
1.4.1.4 Pulsed laser deposition	7
1.4.2 Liquid processing synthesis of nanoparticles	7
1.4.2.1 Microemulsion method	7
1.4.2.2 Hydrothermal method	8
1.4.2.3 Sol-Gel Method	8
1.4.3 Solid processing synthesis of nanoparticles	8
1.4.4 Synthesis of nanowires	8
1.4.4.1 Nanowire Template Assisted Growth by Pressure Injec- tion	9
1.4.4.2 Electrochemical deposition	9
1.4.4.3 Vapor deposition	10
1.4.5 VLS Methods for Nanowires Synthesis	10

CONTENTS

1.4.6	Other methods for nanowires synthesis	10
	References	12
2	Pulsed laser deposition technique	13
2.1	Primary processes of laser ablation	14
2.1.1	Ballistic process	14
2.1.2	Electron sputtering	15
2.1.3	Thermal-spike sputtering	16
2.2	Secondary processes of laser ablation	17
2.2.1	Collision-free flow	17
2.2.2	The Knudsen layer	17
2.2.3	Beyond the Knudsen layer	18
2.3	Plasma formation	18
2.3.1	Inverse bremsstrahlung	18
2.3.2	Photo-ionization processes	19
2.4	Plume expansion	19
2.5	Growth of the film	20
	References	22
3	Experimental set-up	23
3.1	Pulsed Laser Deposition apparatus	23
3.1.1	Laser energy calibration	26
3.1.1.1	Determination of the fluence	27
3.2	R.F. sputtering apparatus	29
3.3	Apparatus for measurement of hydrogen	30
4	Co-B nanoparticles synthesized by PLD	33
4.1	Introduction	33
4.2	Synthesis of the samples	34
4.3	Characterization of the films	35
4.3.1	SEM results	35
4.3.2	TEM results	36
4.3.2.1	Co-B film deposited at 1 J/cm^2	36
4.3.2.2	Co-B film deposited at 3 J/cm^2	41

4.3.2.3	Co-B film deposited at $9 J/cm^2$	43
4.3.2.4	Summary of TEM results	44
4.3.3	XPS results	45
4.3.3.1	XPS on the powders	45
4.3.3.2	XPS on the films	47
4.3.3.3	Summary of XPS results	50
4.3.4	AFM results	50
4.4	Discussion on samples characterization	51
4.5	Catalytic activity measurements	54
4.6	Improvement in catalytic activity	57
4.6.1	Synthesis and characterization of the samples	57
4.6.2	Catalytic activity measurements	59
References		61
5	Cobalt oxide nanoparticles synthesized by PLD	63
5.1	Introduction	63
5.2	Synthesis of the samples	64
5.3	Characterization of the films	66
5.3.1	Different substrate temperature	66
5.3.2	Different oxygen partial pressure	68
5.3.3	Different target-to-substrate distance	76
5.3.4	Different post-deposition treatment	77
5.4	Discussion on sample characterization	81
5.4.1	Different substrate temperatures	85
5.4.2	Different oxygen partial pressure	85
5.4.3	Different target-to-substrate distance	88
5.4.4	Different post-deposition treatment	90
5.5	Final remarks	91
References		93
6	TiO_2-doped Cr/ITO multilayer thin films by R.F. sputtering	97
6.1	Introduction	97
6.2	Synthesis of the samples	99
6.3	Characterization of the films and photocatalytic activity measurements	101

CONTENTS

6.4	Discussion on sample characterization	108
	References	115
7	Synthesis and characterization of Pb nanowires	119
7.1	Introduction	119
7.2	Results and Discussion	120
7.2.1	Pb concentration	120
7.2.2	Focus on nanowires	122
7.2.3	Substrate material	125
7.2.4	Deposition time	125
7.2.5	Al/Pb sputtering deposition	127
7.2.6	Pb doped Al	132
7.2.7	XRD results	133
7.2.8	XPS results	133
7.3	Discussion on deposition parameters influence on NWs formation	134
7.4	Different storage conditions	136
7.5	Discussion on different storage conditions	140
7.6	In-situ NWs growth	141
7.7	Discussion on NWs in-situ SEM growth	143
7.8	Conclusion	144
	References	146
8	Concluding remarks and perspectives	149
A	R.F. Sputtering deposition	153
B	Scanning electron microscopy	157
C	Transmission electron microscopy	159
D	X-ray Photoelectron Spectroscopy	165

List of Figures

3.1	A schematic 3D view of the laser deposition apparatus	24
3.2	A schematic of the a) vacuum system, b)by-pass system	25
3.3	View of the PLD chamber	25
3.4	Measurement of the optical losses	27
3.5	Measurement of the crater size on Al target for different number of pulses (N)	28
3.6	Gaussian profile of the laser beam and consequent crater shape	28
3.7	R.F. sputtering apparatus	30
3.8	Schematic diagram of the experimental apparatus for GV analysis	31
4.1	SEM micrographs of Co-B powders	35
4.2	Co-B film deposited at different fluences	37
4.3	Co-B NPs	38
4.4	Typical EDX spectrum on a shell of a NP deposited at $3 J/cm^2$	38
4.5	Bright field TEM images of Co-B film deposited at $1 J/cm^2$	38
4.6	STEM images a the core/shell NP	39
4.7	a) Selected Area Electron Diffraction (SAED) and, b) the relative radi- ally averaged intensity function of small NPs obtained at $1 J/cm^2$	40
4.8	Different region where EDX compositional spectra were acquired	40
4.9	Bright field TEM images acquired at different tilt of the sample stage	41
4.10	Bright field TEM on the small NPs for $3 J/cm^2$	42
4.11	EDX spectrum of the shell of one NP for $3 J/cm^2$	43
4.12	STEM images of core/shell NP obtained at $9 J/cm^2$	44
4.13	XPS survey (from 1200 to 0 ev) of the Co-B powders	46
4.14	O1s spectra of XPS spectrum for sample at $12 J/cm^2$)	48

LIST OF FIGURES

4.15	C1s spectra of XPS spectrum for sample at $12 J/cm^2$)	48
4.16	B1s spectra of XPS spectrum for sample at $12 J/cm^2$)	49
4.17	Co2p spectra of XPS spectrum for sample at $12 J/cm^2$)	49
4.18	XPS fit peaks area vs fluence	51
4.19	AFM images of samples at a) 1, b) 3, c) 9, d) $12 J/cm^2$	52
4.20	Hydrolysis of SBH solution (0.025 M) at 298K	55
4.21	Hydrolysis of AB solution (0.025 M) at 298K	56
4.22	SEM micrographs of carbon film and Co-B supported C film deposited under different Ar gas pressure	58
4.23	Hydrolysis of B (0.025 M) with Co-B film on carbon film Co-B supported C film deposited under different Ar gas pressure	60
5.1	SEM micrographs of Co oxide films produced at different temperature .	66
5.2	X-ray diffraction pattern of Co oxide films NPs synthesized by PLD at different temperatures	67
5.3	Raman spectra of Co oxide films NPs synthesized by PLD at different temperatures	69
5.4	SEM micrographs of Co oxide films produced at different P_{O_2}	70
5.5	Raman spectra of Co oxide films NPs synthesized by PLD at different P_{O_2}	71
5.6	FT-IR absorption spectra of Co oxide films NPs synthesized by PLD at different P_{O_2}	72
5.7	BF-TEM images of a core/shell NP	73
5.8	BF-TEM images of a core/shell NP with an incomplete shell	73
5.9	HR-TEM images small NPs	74
5.10	HR-TEM images of the shell surrounding big NPs	74
5.11	STEM images of small NPs dispersed on the carbon support	75
5.12	BF-TEM images of two kind of big NPs: a) core/shell NPs, b) amorphous cobalt oxide NPs	75
5.13	BF-TEM images with region analyzed by EDX evidenced : 1) small NPs, 1) big	76
5.14	SEM micrographs of Co oxide films produced at different d_{t-s}	77
5.15	Raman spectra of Co oxide films NPs synthesized by PLD at different d_{t-s}	78

LIST OF FIGURES

5.16 FT-IR absorption spectra of Co oxide films NPs synthesized by PLD at different d_{t-s}	79
5.17 HRTEM images of small NPs with reported experimental $d(\text{\AA})$	80
5.18 SEM micrographs of Co oxide films produced at different conditions	81
5.19 Raman spectra of Co oxide films NPs synthesized by PLD at different treatment	82
5.20 FT-IR absorption spectra of Co oxide films NPs synthesized by PLD at different conditions	83
5.21 BF-TEM images of a big NPs with not spherical shape	84
5.22 HR-TEM images of a core/shell (Co-hcp/Co oxide) NPs	84
5.23 SEM micrographs magnification of cobalt oxide NPs	85
6.1 XRD spectra of undoped and Cr-doped TiO_2 films	102
6.2 UV-VIS absorption spectra of undoped and Cr-doped TiO_2 films	103
6.3 Tauc plot of undoped and Cr-doped TiO_2 films	103
6.4 SEM Images, in back scattering mode, of ITO/Cr9-doped TiO_2 multilayer films	107
6.5 Photocurrent and thickness of each Cr9-doped TiO_2 layer as a function of number of bilayers	107
6.6 A) Schematic representation of the photocurrent transient curve. Normalized plot of current-time dependence for: B) pure TiO_2 , C) single bilayer, and D) 6-bilayers of ITO/Cr9-doped TiO_2 multilayer film	110
6.7 Hydrogen evolution, as a function of time, from water-splitting by using sputter-deposited pure TiO_2 and 6-bilayers of ITO/Cr9-doped TiO_2 multilayer film in photoelectrochemical cell containing two electrolytes of different pH	113
7.1 ALPb film: low Pb Concentration	121
7.2 ALPb film: mid Pb Concentration	121
7.3 ALPb film: high Pb Concentration	122
7.4 In plan general view of ALPb film	123
7.5 Lateral view	123
7.6 Magnified NW	124
7.7 Elemental composition of NWs	124

LIST OF FIGURES

7.8	AlPb: focus on grain boundary	125
7.9	Copper substrate	126
7.10	SiO_2 substrate	126
7.11	Silicon substrate	126
7.12	Stainless steel substrate	127
7.13	AlPb film: 1min deposition time	127
7.14	AlPb film: 3min deposition time	128
7.15	AlPb film: 5min deposition time	128
7.16	AlPb film: 7min deposition time	128
7.17	AlPb film: 10min deposition time	129
7.18	AlPb film: 15min deposition time	129
7.19	AlPb film: 40min deposition time	129
7.20	AlPb film: 60min deposition time	130
7.21	Pb whisker on Al:	130
7.22	Pb hillock on Al:	131
7.23	Top view of Pb on Al:	131
7.24	Pb film doped Al: surface	132
7.25	Pb film doped Al: micro-structures	132
7.26	XRD of AlPb films	133
7.27	XPS spectrum related to the:	134
7.28	AlPb film: as-deposited sample:	137
7.29	AlPb film: ambient atmosphere:	137
7.30	AlPb film: low vacuum:	138
7.31	AlPb film: argon atmosphere:	138
7.32	AlPb film: oxygen atmosphere:	139
7.33	AlPb film: annealing in vacuum:	139
7.34	AlPb film: dry atmosphere:	140
7.35	E-beam irradiated area of the AlPb films:	142
7.36	In-situ NWs growth	142
7.37	Measured length (symbols) of a single NW vs. e-beam irradiation time .	143
7.38	Schematic representation of NWs growth	145
A.1	Schematic of the sputtering deposition apparatus	155

LIST OF FIGURES

B.1 Schematic diagram of a SEM	157
C.1 Schematic diagram of a TEM	160
C.2 The two principal modes of TEM operation	161

LIST OF FIGURES

List of Tables

4.1	areal density of the NPs obtained at $1 J/cm^2$ as a function of their dimensions	39
4.2	Results of EDX compositional spectra for $1 J/cm^2$ sample	41
4.3	areal density of the NPs obtained at $3 J/cm^2$ as a function of their dimensions	42
4.4	Results of EDX compositional spectra for $3 J/cm^2$ sample	43
4.5	areal density of the NPs obtained at $9 J/cm^2$ as a function of their dimensions	43
4.6	Results of EDX compositional spectra for $9 J/cm^2$ sample	44
6.1	TiO_2 optical band gap and doping energy level values for undoped and Cr-doped TiO_2 films deposited by RF-magnetron sputtering with several Cr concentration	104
6.2	Photo-voltage and photocurrent measured for different numbers of ITO/ TiO_2 bilayers	112
7.1	Quantitative results of EDS analysis on NWs	123

LIST OF TABLES

1

Introduction on nanomaterials

Today we are living in an industrialized environment and while taking advantage of its benefits, we are also facing major disadvantages. Industrial wastewaters contain several potentially toxic chemicals that often contaminate the surface water and soil. Pollution of aquatic and soil can result in uptake and accumulation of toxic chemicals in food chains and also harm to the flora and fauna of affected habitats [1]. Moreover the industrial sector, together with the electric power distribution to the end-user, represents the biggest contribution to the emission of greenhouses gas (GHG). Approximately two-thirds of the industrial sector's emissions result from the combustion of fossil fuels and from the industrial processes of each sector. The remaining one-third of industrial sector GHG emissions results from the off-site generation of electricity purchased by the sector [2]. Industrial energy also includes natural gas and petroleum products (naphtha and natural gas liquids) used as feedstocks to produce non-energy products, such as plastics. In aggregate, the industrial sector uses more energy than any other end-use sector, consuming about one-half of the world's total delivered energy [3].

So global energy resources will be facing a major breakdown due to increasing requirement for energy. The search for clean renewable energy becomes of fundamental importance to try solving these problems. Hydrogen, with its high gravimetric energy density, is a promising route to store renewable energy. Moreover, there is almost zero emission of environment pollutants when hydrogen is used as a fuel in proton exchange membrane fuel cell (PEMFC). However we are still searching for a fast and clean method to supply hydrogen . Moreover to have the complete life cycle of hydrogen fuel clean and renewable it is very important to produce hydrogen gas by using clean

1. INTRODUCTION ON NANOMATERIALS

and renewable energy sources such as solar and wind. Hydrogen can be produced from some chemical hydrides, by either hydrolysis or thermolysis, with an end product which is nontoxic and environmentally safe [4, 5]. The hydrolysis reaction can be effectively controlled by heterogeneous catalyst. Clearly the role of catalyst is crucial also in the photocatalytic water-splitting, and finally catalyst are essential in photodegradation of organic dyes in waste water treatment.

The general purpose of catalysts is to increase the speed of a given reaction. This is achieved through kinetic means and does not directly affect the thermodynamic properties of a chemical system. Nanomaterials are more effective than conventional catalysts for two main reasons: their high surface to volume ratio, favorable for chemical reactions and their characteristic properties due to the small size (that will be discussed sooner).

So it is essential to find easy and cheap technique to synthesize nanostructures. We synthesized nanoparticles (by pulsed laser deposition technique), thin films (having thickness of hundred of nm) and nanowires (by R.F. sputtering deposition technique). The mechanisms of formation of nanoparticles and nanowire have been investigated and measurements of their catalytic activity have been performed.

1.1 Overview of the thesis

In the next section of this chapter we will briefly describe the properties of nanomaterials and the processes for their synthesis. In chapter 2 we present the pulsed laser deposition mechanism. More in details interaction of the laser beam with the target, interaction of the ablated plume with the laser beam, expansion of the plume and mechanism of film growth on the substrate are described. In chapter 3 we discuss our works on Co-B nanoparticles produced by pulsed laser deposition. Synthesis of the nanoparticles and their characterization are explained. A discussion on the obtained results are reported, together with the catalytic activity measurements of the Co-B samples for production of hydrogen from chemical hydride. In chapter 4 we describe results on pulsed laser deposition of core/shell cobalt oxide nanoparticles. Mechanism involved on formation of the core/shell structures are proposed and discussed. In chapter 5 we discuss the synthesis of Pb nanowires by using R.F. sputtering deposition. A stress-mechanism induced growth process is proposed. In chapter 6 we present the

production of TiO_2 /ITO multilayer thin film by R.F. sputtering deposition and their application in photocatalytic water-splitting for hydrogen production.

1.2 What are nanomaterials?

On 18 October 2011, the European Commission adopted the following definition of a nanomaterial:

“A natural, incidental or manufactured material containing particles, in an unbound state or as an aggregate or as an agglomerate and where, for 50 % or more of the particles in the number size distribution, one or more external dimensions is in the size range 1 nm - 100 nm. In specific cases and where warranted by concerns for the environment, health, safety or competitiveness the number size distribution threshold of 50 % may be replaced by a threshold between 1 and 50 %.”

Nanomaterials are used in every-day consumer products to make them stronger, cleaner, more efficient, more aesthetic and so on [6].

improve their quality such as weight, strength, aesthetics and so on. They have a considerable impact in medical and pharmaceutical sector, bio-nanotechnology, biosensors, energy sector, including fuel cells, batteries and photovoltaics, environment sector including water treatment, automotive sector, aeronautics sector, construction sector, including reinforcement of materials, composite materials, electronics and optoelectronics, photonics [7].

Nanomaterials can be divided into three classes, according to the number of dimension which are not confined to the nanoscale range [8]:

- 0D nanomaterials: all dimension at nanoscale range. Example of 0D nanomaterials are nanoparticles, clusters, colloids, nanocrystals, and fullerenes. Electrons are confined in all three directions.
- 1D nanomaterials: two dimension at nanoscale range, other dimension not. They are generally cylinder-like objects like wires and tubes with diameters on the nanoscale and lengths typically in the micrometer range. Electrons may be confined in the transverse direction while they may be free to move in another one dimension along the structure.

1. INTRODUCTION ON NANOMATERIALS

- 2D nanomaterials: one dimension at nanoscale range, other two dimensions not. 2D nanomaterials may appear as thin films with thickness of the order of a few nanometers. Electrons may be confined in the direction perpendicular to film, while in the two dimensions parallel to the film the electrons behave like in a bulk material.

1.3 Properties of nanomaterials

Reducing the size of materials allows to a better packing of elements or information but, more important, allows the occurrence of novel optical, electric and magnetic properties. Nanomaterials behave differently respect to materials of a coarser structure because of two major effects: the high surface-to-volume ratio and the quantum size effect in the interior of nanocrystals. These characteristics strongly influence the physico-chemical properties of the materials.

First, in nanomaterials there is a large fraction of atoms at the surface. The surface atoms have lower coordination and unsatisfied bonds and reduced cohesive energy than bulk atoms. This affects thermodynamic properties of the materials such for example the melting temperature. [9].

In a wide range of materials a decrease in solid to liquid transition temperature with decreasing nanocrystal size has been observed. An explanation of these phenomena comes from the Lindemanns criterion which states that the melting temperature of a material is proportional to its cohesive energy. In nanomaterials the surface atoms contribute largely to the total cohesive energy so, according to what said before, the melting temperature is lower than that for bulk materials.

Other concepts of thermodynamics can break down, especially if the system considered consists of a single isolated cluster with a small numbers of atoms. The Gibbs phase rule loses its meaning because phases and components are not longer properly distinguishable [9]. Phase transitions are collective phenomena. So with a lower number of atoms in a cluster a phase transition is less well defined [9].

The other important effect of the nano-dimension of materials is the quantum size effect. In bulk materials atoms have their well established atomic orbitals. Depending on the extent of overlap in a solid they remain mostly unperturbed, as in noble gases, or they combine to extended band structures, as in metals or semiconductors. The core

orbitals are confined to a relatively small volume and remain localised (atom-like). Each of N atoms contributes with its atomic states to a band so that, although the width of a band increases slightly when more atoms are added, the density of states (DOS) within a band is basically proportional to the number of atoms of an ensemble with an extended band-like state. The band width amounts typically to a few eV. Thus, the DOS is on the order of N per eV, which is very large for a bulk amount of matter ($N \approx$ Avogadro's number, N_A) but low for small clusters. The DOS basically scales smoothly with size, but with a scaling law that is different from that found from surface effects. It is described to a first approximation by the "particle in a box" model, which will not be described in detail. The important point is the existence of a threshold in size where the gap between the highest occupied and the lowest unoccupied state (called the Kubo gap δ) equals the thermal energy. When electrons get thermally excited across the Kubo gap, a low temperature insulator becomes a semiconductor and at higher temperatures a metal; and also magnetic properties of small clusters can change dramatically [9].

1.4 Synthesis of nanomaterials

There are two possible approaches to the synthesis of nanomaterials: top-down and bottom-up. The bottom-up approach involves the construction of nanomaterials from basic building blocks, i.e. atoms and molecules [10]. Examples of bottom-up methods are quantum dot formation from epitaxial growth and formation of nanoparticles from colloidal dispersion. Top-down approaches start from larger structures to reduce them into smaller ones [10]. Typical examples of top-down methods are etching through the mask, ball milling and application of severe plastic deformation. Preparation of nanomaterials can be also classified into physical and chemical methods. The physical methods are based on subdivision of bulk metals, including mechanical crushing or pulverization of bulk material, arc discharge between metal electrodes, etc. The chemical methods are based on the reduction of metal ions or decomposition of precursors to form atoms, followed by aggregation of the atoms. However, it is notable that some methods can be considered as either chemical or physical routes depending on the media, precursors, and operating conditions such as milling. Finally, nanomaterials synthesis can be classified based on the process media, including vapor, liquid

1. INTRODUCTION ON NANOMATERIALS

and solid state processing routes. In this introduction we will describe only the synthesis processes for the structures studied in the presented work, i.e. nanoparticles and nanowires.

1.4.1 Vapor processing synthesis of nanoparticle

The vapor-phase synthesis of nanoparticles involves the generation of the vapor of the material of interest, followed by the condensation of clusters and nanoparticles from the vapor phase. The vapor may be generated by thermal, laser, electron beam, etc. evaporation. Different sources of energy can be used to decompose the precursor such as microwave plasma, laser pyrolysis, laser photolysis, combustion flame, etc [11].

1.4.1.1 Chemical Vapor Condensation (CVC)

In the CVC method the target materials are vaporized by heat source and then rapidly condensed. Chemical reactions occur between the vapor and other system components during the vaporization and condensation. A conventional CVC system is divided in two segments: a reaction chamber maintained at vacuum and a precursor delivery system operating at ambient pressure. A gas delivery system carries the precursor gas into the reaction chamber through a heated tubular reactor. Inside the heated tube, individual molecules start to decompose and combine to form small clusters or nanoparticles. At the outlet of the furnace tube, the gas containing nanoparticles expands quickly mitigating the particle growth and agglomeration. At the end, the nanoparticles condense on a cooled substrate from which they can be scraped off and collected [12]. The properties of particles synthesized by the gaseous reaction method depend on the physico-chemical characteristics of the reaction systems. Their properties are also affected by the reactor design, the heating method, the temperature gradient, preheating of the reactive gases, the method of introducing the gas into the reactor, the decomposition temperature of precursor, the heating temperature for vaporization of the precursor and so on [13]. The CVC method has been used to produce nanopowders of metals, oxides, carbides, nitrides, borides or their composites.

1.4.1.2 Arc Discharge Method

Metal precursors, usually packed inside a cave drilled into a graphite electrode, undergo arc vaporization employing another electrode furnished with a mixture of appropriate

catalysts. This method has been used to synthesize excellent high-quality carbon nanotubes structures. It is also used to obtain metal carbides, boron oxide-encapsulated magnetic nanocapsules, fullerenes and so on. Disadvantages of arc discharge method are the limited amount of material that can be produced by batch and the formation of a substantial amounts of nanoparticles with polyhedral shape and low aspect ratio [14].

1.4.1.3 Laser Pyrolysis

This method is based on the resonant interaction between laser photons and at least one gaseous species. Laser-driven pyrolysis is a general synthetic tool allowing the synthesis of uniform and controllable nanoscale particles ranging from 2 nm to 20 nm at rapid heating and cooling rate ($\approx 10^5 \text{ }^\circ\text{C s}^{-1}$). Nanotubes and iron carbides shell-structured nanoparticles have been produced through this method. However laser pyrolysis has the disadvantages of a low production rate and requires high energy consumption [14].

1.4.1.4 Pulsed laser deposition

We will discuss this technique in the next chapter, because we use this method to synthesize both Co-B and Co oxide nanoparticles. Here we want just to underline the advantage of laser vaporization over other heating methods, such as the production of a high-density vapor of any metal, the generation of a directional high-speed metal vapor from the solid target which can be useful for directional deposition of the particles, the control of the evaporation from specific spots on the target as well as the simultaneous or sequential evaporation of several different targets [11].

1.4.2 Liquid processing synthesis of nanoparticles

1.4.2.1 Microemulsion method

A microemulsion is an isotropic and thermodynamically stable single phase formed by at least three components; two of them are non miscible, and the third one, called surfactant, is characterized by amphiphilic properties. Depending on the proportion of the components, microdroplets can appear in form of oil-swollen micelles dispersed in the aqueous phase (O/W) or water-swollen micelles dispersed in oil (W/O). W/O microemulsion solutions are nanosized water droplets dispersed in the continuous oil

1. INTRODUCTION ON NANOMATERIALS

phase and stabilized by surfactant molecules. These surfactant-covered water pools offer a unique microenvironment for the formation of nanoparticles. Microemulsion is a simple method through which powders with well-defined and controlled properties, and uniform and size controllable nanoparticles may be obtained. By contrast it is an expensive method and surfactant can be adsorbed on the surface of nanoparticles. Moreover separation and removal of some solvents from products is difficult [14].

1.4.2.2 Hydrothermal method

It involves the reaction of high temperature-high pressure aqueous solutions, vapors, and/or fluids with solid materials. It permits to get well crystallized powders, homogeneous in size, shape, composition, as well as nanocrystals with high crystallinity. Many different oxides have been obtained using hydrothermal method. However it is difficult to control the process, so there are problems of reliability and reproducibility [14].

1.4.2.3 Sol-Gel Method

This method is based on inorganic polymerization reactions. This method allows excellent composition control, homogeneity of product and it is strongly promising for employment industrially on a large scale. But it is a very expensive method [14].

1.4.3 Solid processing synthesis of nanoparticles

Mechanical processing, in particular high-energy ball milling, is a convenient way to produce nanosized powders. In ball milling, powders are loaded together with several heavy balls in a container. By vigorously shaking or high speed rotation, a high mechanical energy will be applied on the powders. In this way it is possible to form alloying phase at low temperature. This is a simple and efficient method to obtain intermetallic nanoparticles or magnetic nanoparticles. However, ball milling requires high energy and long period of milling time. Furthermore the obtained particles have numerous defects and contamination [14].

1.4.4 Synthesis of nanowires

Nanowires (NWs) have two quantum confined directions so they can be used for electrical conduction application. There are two main techniques for the synthesis of

nanowires: the template-assisted synthesis and the vapor-liquid-solid (VLS) method. The template-assisted synthesis of nanowires method consists in filling a template containing very small cylindrical pores or voids with a chosen material, which will form the NWs. Templates commonly used include anodic alumina (Al_2O_3), nano-channel glass, ion track-etched polymers, and mica films [15]. The VLS method involves the absorption of source material from the gas phase into a liquid droplet of catalyst. Upon supersaturation of the liquid alloy, a nucleation event generates a solid precipitate of the source material. This seed serves as a preferred site for further deposition of material at the interface of the liquid droplet, promoting the elongation of the seed into a nanowire or a whisker, and suppressing further nucleation events on the same catalyst [15].

1.4.4.1 Nanowire Template Assisted Growth by Pressure Injection

The pressure injection technique is often employed for fabricating highly crystalline nanowires from a low-melting point material or when using porous templates with robust mechanical strength. The templates can be filled by pressure injecting the desired material in liquid form into the empty pores. The chemical stability and the mechanical properties of the template are important to maintain the integrity of the template working at high temperature and high pressure. Nanowires template assisted growth by pressure injection allow to growth metals nanowires (Bi, In, Sn and Al) and semiconductor nanowires (Se, Te, GaSb and Bi_2Te_3). The diameter, uniformity and density of the pore are important parameters for the synthesis of NWs. [15].

1.4.4.2 Electrochemical deposition

In the electrochemical methods, a thin conducting metal film is first coated on one side of the porous membrane to serve as the cathode for electroplating. The length of the deposited NWs can be controlled by varying the duration of the electroplating process. Via electrochemical deposition metal NWs (Bi, Co, Fe, Cu, Ni, Ag, Au), conducting polymers, superconductors (Pb), semiconductors (CdS) and superlattice nanowires with A/B constituents were synthesized. One advantage of the electrochemical deposition technique is the possibility of fabricating multilayered structures within NWs. By varying the cathodic potentials in the electrolyte containing two different kind of ions, different metal layers can be controllably deposited. In the electrochemical deposition

1. INTRODUCTION ON NANOMATERIALS

process, the chosen template has to be chemically stable in the electrolyte during the electrolysis process. The properties of templates are also essential for this technique because the presence of cracks and defects in the templates are detrimental to the nanowire growth [15].

1.4.4.3 Vapor deposition

Vapor deposition includes physical vapor deposition (PVD), chemical vapor deposition (CVD) and metallorganic chemical vapor deposition (MOCVD). Like electrochemical deposition, vapor deposition is usually capable of preparing smaller diameter (≤ 20 nm) NWs than pressure injection methods, since it does not rely on high pressure and surface tension involved to insert the materials into the pores. In the physical vapor deposition technique, the material to be filled is first heated to produce a vapor, which is then introduced through the pores of the template and cooled to solidify [15].

1.4.5 VLS Methods for Nanowires Synthesis

Since the liquid droplet catalyzes the incorporation of material from the gas source to the growing crystal, the deposit grows anisotropically as a whisker whose diameter is dictated by the diameter of the liquid alloy droplet. The NWs thus obtained are of high purity, except for the end containing the solidified catalyst as an alloy particle. A wide variety of elemental, binary, and compound semiconductor NWs has been synthesized by the VLS method, and relatively good control over the nanowire diameter and diameter distribution has been achieved. However, reduction of the average wire diameter to the nanometer scale requires the generation of nanosized catalyst droplets. But due to the balance between the liquid-vapor surface free energy and the free energy of condensation, the size of a liquid droplet, in equilibrium with its vapor, is usually limited to the micrometer range. This obstacle was overcome in recent years by using different methodologies to form the nanoscale island [15].

1.4.6 Other methods for nanowires synthesis

NWs may also be obtained by "bottom-up" approaches. Stress-induced crystalline bismuth NWs have been grown from sputtered films of layers of Bi and CrN. The NWs presumably grow from defects and cleavage fractures in the film, and are up to several

1.4 Synthesis of nanomaterials

millimeter in lengths with diameters ranging from 30 to 200 nm. While the exploration of this technique has only begun, stress-induced unidirectional growth should be applicable to a variety of composite lms. Stress-induced growth of NWs will be discussed later in this thesis because it is the mechanism behind the synthesis of Pb NWs discussed in this thesis.

REFERENCES

References

- [1] M.A. Fayidh, S. Babuskin, K. Sabina, M. Sukumar, and M. Sivarajan. *J. Microbial. Biochem. Technol.*, 3(4):060–066, 2011. 1
- [2] U.S. Environmental Protection Agency. *Working Draft*, May 2008. 1
- [3] U.S. energy information administration. *International energy outlook*, Report Number(DOE/EIA-0484), 2011. 1
- [4] T. Umegaki, J.M. Yan, X.B. Zhang, H. Shioyama, N. Kuriyama, and Q. Xu. *Int. J. Hydrogen Energy*, (34):2303–2311, 2009. 2
- [5] F.H. Stephens, V. Pons, and R.T. Baker. *Dalton Trans.*, (25):2613–2626, 2007. 2
- [6] European Commission Joint Research Centre Institute for Health and Consumer Protection. *JRC57894*, 2010. 3
- [7] D. Bhattacharyya, S. Singh, N. Satnalika, A. Khandelwal, and S.H. Jeon. *Int. J. of u- and e- Service, Science and Technology*, 2(3), 2009. 3
- [8] M. F. Ashby, P. J. Ferreira, and D. L. Schodek. Nanomaterials, nanotechnologies and design. *Butterworth-Heinemann*, 2009. 3
- [9] E. Roduner. *Chem. Soc. Rev.*, 35:583–592, 2006. 4, 5
- [10] C. Raab, M. Simk, U. Fiedeler, M. Nentwich, and A. Gatz. *NanoTrust-Dossier*, 006en, 2011. 5
- [11] G. Glaspell, V. Abdelsayed, K. M. Saoud, and M. S. El-Shall. *Pure Appl. Chem.*, 78(9):1667–1689, 2006. 6, 7
- [12] C. Suryanarayan and C.C. Koch. *Hyperfine Interactions*, 130:5–44, 2000. 6
- [13] A. Kato. Ultra-fine particles. *Exploratory Science and Technology*, pages 197–212, 1995. 6
- [14] A. Tavakoli, M. Sohrabi, and A. Kargari. *Chem. Pap.*, 61(3):151–170, 2007. 7, 8
- [15] M. S. Dresselhaus, Y.M. Lin, O. Rabinovich, M.R. Blackb, and G. Dresselhaus. *Nanowires*. 2003. 9, 10

2

Pulsed laser deposition technique

Pulsed laser deposition (PLD) is a physical deposition technique where a pulsed laser beam is focused onto a target material that is to be deposited. If the laser energy is high enough the target material is ablated forming a gas plasma called plume. The plume expands along the direction normal to the target surface reaching a substrate placed in front of the target. The pulse duration varies from ps to ns or longer duration. We discuss the ablation mechanism for laser with pulses of ns duration, further considerations should be made for shorter pulses.

The ablation process using lasers with pulses of ns or longer duration occurs in four different stages:

1. interaction of the laser beam with the target, and subsequent formation of the plume
2. interaction of the plume with the laser beam
3. expansion of the plume
4. growth of the film on the substrate

These stages overlap in time so it is difficult to have a complete explanation of all the PLD process. However there are models that explain each single stage [1].

In the first stage the electrons of the atomic system absorb the photons of the laser beam. The interaction of the laser beam with the target depends on several parameters including the absorption coefficient and reflectivity of the target material, the pulse duration, wavelength and fluence of the laser. The excited electrons transfer their

2. PULSED LASER DEPOSITION TECHNIQUE

energy to the lattice through electron-phonon interactions. The energy transfer to the lattice is very fast and is complete in about 10^{-12} s.

There is an energy threshold over which the ablation process can start.

Laser light absorption may be described by an exponential law:

$$I = (1 - R)I_0e^{-\mu x} \quad (2.1)$$

where I_0 is the intensity of the incident pulse, I is the intensity at distance x beneath the surface which is located at $x=0$, μ is the absorption coefficient, and R is the reflection coefficient. μ and R depend on the radiation frequency, on the electronic density (hence on temperature), on the state (amorphous or crystalline), and on the presence of possible contaminants on the target surface. Moreover, when both the laser intensity (between 10^7 and $10^8 W/cm^2$) and the pulse duration are high enough the target temperature reach a characteristic value well above the melting point beyond which metals loss the ordinary conductivity and becomes a dielectric, and so μ and R undergo a strong reduction. So laser pulse width and wavelength, target materials optical and thermal properties influence the ablation threshold [2]. When the fluence is high enough the ablation starts. Different mechanisms are involved in this process.

These are generally sub-divided into primary and secondary processes. The emission of particles from the surface is a primary mechanism, and the subsequent dynamics of particles is a secondary mechanism. The two are distinguished because if the flow of particles emitted is high enough and if the energy of incident particles is not too low, then the dynamics of particles emitted is independent of the processes that led to the release.

2.1 Primary processes of laser ablation

Primary processes can be subdivided into ballistic, thermal, electronic and macroscopic sputtering; their relative importance will depend on the nature of the target material, and on the laser excitation wavelength and pulse duration.

2.1.1 Ballistic process

In laser ablation it is not possible to have a direct momentum transfer, because the photons of the beam transfer negligible energy to the target atom. However there can

be indirect collisional effects with photons due to the interaction of the ablated plume with the laser beam. Ions in the plume are accelerated to as much as 100-1000eV and nearby surfaces are ion-bombarded, as indicated by the formation of conical structures on the target surface [3].

2.1.2 Electron sputtering

Electron sputtering comprises a group of processes which involve some form of excitation or ionization. It normally occurs in dielectrics and wide band-gap semiconductors but it can be observed also with metals due to surface plasmons [3]. In the first case the mean life of excited electronic state can be sufficiently is comparable to the time required for separation of the nuclei of a molecule under the action of the mutual repulsive force. So after an electronic excitation, a molecule can pass from one bond state to an antibond state. In metals the photons can excite the plasmons of the target, which in turn can cause the emission of atoms from the surface. The effect of the electron sputtering on laser ablation depends on pulse energy. For high fluences, dense electron excitation can lead to an increase of the vapor pressure increases by orders of magnitude or even render the lattice unbound. For low fluences, defects can form at and beneath the target surface. If the defects are on the surface there is the energetic expulsion of individual atoms [4]. There are no direct evidence of electron sputtering process, but particles emitted by this mechanism are characterized by a number of unusual features:

1. Existence of a threshold pulse energy density for particle emission;
2. Kinetic energies of the order of a few eV;
3. Rotational and vibrational energies appropriate to the real target temperature
4. High degree of directionality due to crystallographic orientation of the relevant defects (this comportment is not easily distinguishable from the forward peaking due to gas-dynamics);
5. A non-thermodynamic (i.e. excessive) yields of ions [3].

2. PULSED LASER DEPOSITION TECHNIQUE

2.1.3 Thermal-spike sputtering

Thermal-spike sputtering is a group of three processes that involve particle emission due to a transient high temperature. It dominates when using long (e.g. nanosecond duration) laser pulses, of sufficient duration to allow photon coupling with both the electronic and vibrational modes of the target material. Thermal-spike sputtering includes: normal vaporization, normal boiling and phase explosion. Normal vaporization consists of particle emission from the surface of the target due to a high temperature. It can occur with both insulators and metals and there is no temperature threshold for the presence of this process. However it is not important for low fluences or very short pulses.

Instead normal boiling process requires that the pulse length be sufficiently long for heterogeneous vapor nucleation to occur. Nucleation involves a region of the target extending from the surface to a depth related either to the absorption length or to the thermal diffusion length. Unlike normal vaporization, there is a temperature threshold, T_b . In this case the surface temperature is fixed at or somewhat above the boiling point T_b , and the temperature gradient at and beneath the surface is ≈ 0 . Since T_b will always exceed the target melting temperature, T_m , wavelike structures appear on the target surface after the laser beam irradiation. These indicate localized melting and are often considered as confirmatory evidence for the thermal sputtering occurrence.

When the laser fluence is sufficiently high and the pulse length sufficiently short (ns pulses), the target reaches a temperature equal to almost $0.90T_c$, at and beneath the surface, where T_c is the thermodynamical critical temperature. The rapidly heated system may undergo superheating that is the temperature of the liquids becomes higher than that of boiling under the given pressure. If so, the system shifts from the binodal into the region of the metastable states. However there is a limit for the superheating of the liquid: the spinode [3]. Near the critical point a liquid metal undergoes such as the decrease of density, mainly due to the intensified fluctuation of the specific volume, and the increase of the specific heat, mainly due to the increasing fluctuation of ΔH . The increasing nucleation prevents the liquid from approaching the spinodal, resulting in decay of the highly superheated liquid into a mixture of gas and droplets [5]. Like normal boiling there is again a temperature threshold, but it involves homogeneous vapor nucleation.

Finally there are some phenomena that go under the name of macroscopic sputtering. Exfoliation, whereby macroscopic flakes detach from the target as a result of the repeated thermal shocks, is one of this. It can arise when using target materials having high thermal expansion coefficients and a sufficiently high melting point that the thermal oscillations induced by repeated pulsed laser excitation do not exceed T_m [6]. Macroscopic particulate ejection can also arise in the case of porous targets, wherein the localised laser induced heating will cause very rapid expansion of any trapped gas pockets just below the surface and forcible ejection of the surface material[6].

2.2 Secondary processes of laser ablation

For low rates of vaporization the gas density may be low enough to not allow the achievement of thermal equilibrium through collisions between particles (collision-free flow). Increasing evaporation rate, the gas density increases and so the number of collisions. If the number of collision is sufficiently high there is the formation of a region in which particles can reach the local thermal equilibrium (Knudsen layer). At the end of the Knudsen layer we have a region where the gas dynamics obey the laws of fluid dynamics (unsteady adiabatic expansion). The equation of gas dynamic can be used to describe this expansion. For high evaporation rate there can be also a fraction of particles that go back to the target surface and which may recondense there.

2.2.1 Collision-free flow

In this situation each particles keep its original velocity, in the limit $t \gg \tau_l$ where τ_l is the pulse duration. The particles go into free flight and are described by whatever velocity distribution is appropriate to the primary sputtering mechanism. For particle emission by a thermal mechanism the velocity distribution of the particles must be given by a Maxwellian restricted to positive velocities, v_x , normal to the surface [2, 3].

2.2.2 The Knudsen layer

For high rate of vaporization the thermal emitted particles reach equilibrium after the first few collisions near the surface in a region termed the Knudsen layer (KL). KL is nearly fully developed after only 2-3 mean free paths. The particles emitted from the surface have initially only $v_x > 0$. In the KL region they develop negative velocities.

2. PULSED LASER DEPOSITION TECHNIQUE

But, mainly in order that momentum be conserved, the particles must also develop a positive center-of-mass (flow) velocity u_K . Without going into detail we mention that the velocity distribution of the particles then changes from the former Maxwell-Boltzmann form to a shifted Maxwellian in which the normal velocity v_x is replaced by $v_x - u_K$. The particles then show forward peaking with an angular distribution of the flux similar to $\cos^4(\theta)$ [2, 3].

2.2.3 Beyond the Knudsen layer

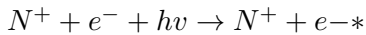
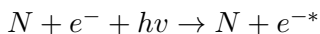
If the density of the gas at the boundary of the KL is high enough, then the particles enter in a so-called unsteady adiabatic expansion (UAE). In the UAE the mean free path of the particles is short, and the plasma behaves as a continuum fluid. Then we can use the flow equations of gas-dynamics [4].

2.3 Plasma formation

After the first stage of laser ablation the gas expansion is driven by the energy which is accumulated as thermal energy and energy which is stored as excitation and ionization in the initial layer. This energy is converted to kinetic energy of the atoms in the plume. After the laser pulse the plume propagation can essentially be considered as an adiabatic expansion [1]. We want to discuss now the second stage of the laser ablation. The expanding plume is heated by various absorption processes which attenuate the laser light that is transmitted through the plume to the solid/liquid surface. The principal mechanisms of laser absorption in the plume the laser are the inverse bremsstrahlung (IB) processes and direct single-photon processes.

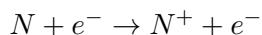
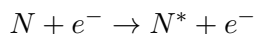
2.3.1 Inverse bremsstrahlung

IB involves absorption of photons by free electrons which are accelerated during collision with neutral (N) or ionized atoms. The cross section for IB via electron-neutral collisions is much smaller than that via electron-ion collisions, but can be important for the initial plume of a weakly ionized gas.



Also occur inelastic collisions between electrons and atoms in the plume that promote

further ionization of the neutrals:



More ions, more electrons and more IB process means more electrons with high energy and more possibilities for ionization by inelastic electron-atom collision. So the ionization rate increases and the plasma switches on.

2.3.2 Photo-ionization processes

For visible and UV laser light the photon energy is comparable to the ionization energy of excited atoms which are produced in the plume by electron-atom collision processes. In this case photon absorption takes place by photo-ionization processes. A number of studies of UV ablation of metal targets have shown that the plasma plume can achieve temperatures of a few eV and an ionization degree that exceeds 0.1 for moderate irradiation intensities ($I \approx 0.1 - 1 \text{GW/cm}^2$) [1].

These processes lead to a formation of a plasma composed of atoms, ions, electrons, photons. At the end of the laser pulse ions recombine with electrons and the excited states loss their potential energy by radiative emission. The plasma stops after total recombination.

2.4 Plume expansion

After the termination of the laser pulse the plume expands adiabatically in three dimensions. If the expansion takes place in vacuum, the shape and velocity distribution in the plume will reach asymptotically constant values. If the ablation takes place in a background gas, the high plume pressure initially drives the expansion as if it were occurring in vacuum. After several μs the plume expansion is entirely determined by the interaction of the plume atoms with the atoms and molecules of the background gas [1]. The theoretical description of the adiabatic expansion has been treated by Anisimov et al.[7] and Singh and Narayan [8], but we will not recall them.

The plume dynamics of a plume expanding in a background gas has been described buy Predtechensky et al. [9] and Arnold et al. [10]. In both the models, the ablated materials plume acts as a piston compressing the background gas during its expansion

2. PULSED LASER DEPOSITION TECHNIQUE

and driving it at supersonic velocity. A contact front is formed between the plume and the ambient gas. The initial expansion of an ablation plume in a background gas does not differ much from the expansion in vacuum, because the plume mass is large compared with the mass of the driven gas accumulated at the plume front [11]. The initial plume front velocity value is very close to that observed in a vacuum (10^6 cm s^{-1}) [7, 12]. The accumulated mass of the background on the plume front increases during the plume expansion. The mass of the plume and the adjacent background mass are considered confined into a hemispherical thin layer at the plume front [11]. Essentially, the plume expansion continues until the gas adjacent mass on the plume front is comparable to or bigger than the mass of the ablated species confined in the thin layer on the plume edge. Then a high counterpressure builds up in the ablated material near to the contact front between the plume and the background gas and the plume expansion velocity starts to slow down. The Predtechensky et al. and the Arnold et al. models differ in their basic hypothesis and physical assumption, but we will not describe them. [11].

As the plasma expands, it adiabatically cools to temperatures typically of 3000-5000 K, and the plasma species can have kinetic energies in a range as large as 1-500 eV, depending on the material, but is normally about 5-50 eV. The angular distribution of the plume has been fitted by many authors to a $\cos^n(\theta)$ function, with values of n ranging from 2 to more than 20. In general, n depends strongly on the laser fluence, and is lower when the plasma propagates into an ambient that is dense enough for there to be multiple collisions, which will broaden the angular distribution [13].

2.5 Growth of the film

The nucleation process and growth kinetics of the film depend on several growth deposition parameters including: laser fluence, substrate temperature, background pressure and rate of deposition. In PLD, a large supersaturation occurs on the substrate during the pulse duration due to the typical extremely high deposition rate (of the order of 10^{20} atoms $\text{cm}^{-2} \text{ s}^{-1}$ [14, 15]). This leads to a very large nucleation density on the surface as compared to other methods such as sputtering deposition. Depending on the deposition parameters three growth modes are possible: step-flow growth, layer-by-layer growth and 3D growth [11]. In step-flow growth mode, atoms on the surface diffuse to a step

edge before they nucleate a surface island. In the layer-by-layer growth mode, islands nucleate on the surface until a critical island density is reached. Then the islands begin to run into each other (coalescence). The coalescence forms a large density of pits on the surface. If additional material still arrives on the surface the atoms diffuse into these pits to complete the layer. This process is repeated for each subsequent layer. The 3D growth starts with the nucleation of island as for the layer-by-layer growth, but once an island is formed an additional island will nucleate on top of the 1st island. Therefore the growth does not persist in a layer by layer mode.

REFERENCES

References

- [1] C. R. Phipps. Laser ablation and its applications. *Springer Series in Optical Sciences*, 129(XX), 2007. 13, 18, 19
- [2] A. Peterlongo, A. Miotello, and R. Kelly. *Phys. Rev. E*, 50(6):4716, 1994. 14, 17, 18
- [3] R. Kelly and A. Miotello. *Nucl. Instr. and Meth. in Phys. Res. B*, 122(3):374, 1997. 15, 16, 17, 18
- [4] D.B. Chrisey and G.K. Hubler. Pulsed laser deposition of thin film. *John Wiley & Sons*, New York, 1994. 15, 18
- [5] N.M. Bulgakova and A.V. Bulgakov. *Appl. Phys. A*, 73:199, 2001. 16
- [6] M.N. R. Ashfold, F. Claeysens, G. M. Fuge, and S. J. Henley. *Chem. Soc. Rev.*, 33:23, 2004. 17
- [7] S. I. Anisimov, D. Bäuerle B.S., and Lukyanchuk. *Phys. Rev. B*, 48:12076, 1993. 19, 20
- [8] R. K. Singh and J. Narayan. *Phys. Rev. B*, 41:8843, 1990. 19
- [9] N.Arnold, J.Gruber, and J.Heitz. *Appl.Phys.A*, 69 S:87, 1999. 19
- [10] M. R. Predtechensky and A. P. Mayorov. *Appl. Supercond.*, 1:10, 1993. 19
- [11] A. Sambri. Pulsed laser deposition of complex transition metal oxides: plume expansion and film growth. *University of Napoli Federico II*, Italy, 2008. 20
- [12] S.Amoruso, A.Sambri, and X.Wang. *J.Appl. Phys.*, 100:013302, 2006. 20
- [13] P. R. Willmott and J. R. Huber. *Rev. Mod. Phys.*, 72(1):315, 2000. 20
- [14] G.Rijnders. The initial growth of complex oxides: study and manipulation. *University of Twente*, The Netherlands, 2001. 20
- [15] M.Huijben. Tuning electronic properties by atomically controlled growth. *University of Twente*, The Netherlands, 2002. 20

3

Experimental set-up

3.1 Pulsed Laser Deposition apparatus

The apparatus for pulsed laser deposition have been developed in our laboratories of Trento University. Our apparatus consists of an excimer (KrF) laser (Lambda Physik LPX 220i), an optical system, a vacuum system, two handling mechanisms, for the target and substrate and a LPX[®] Series Handheld Keypad for purposes of control. The vacuum system and the two handling mechanisms were completely developed in our laboratories.

The laser and halogen source The laser is a LPX220i Lambda Physik laser having the following characteristics: nominal maximum pulse energy 450 mJ, maximum repetition rate 200 Hz, maximum average power 80W, nominal pulse duration 20 ns, beam dimensions 8 mm x 23 mm (vertical x horizontal (V x H)) and beam divergence 1 mrad x 3 mrad (V x H). The pulse energy can be lowered by dropping the pumping high voltage. The repetition rate can be varied in the range 1-200 Hz. The laser is an excimer laser (*KrF*, wavelength 248 nm) with laser action occurring on the $B^2 \Sigma \rightarrow X^2 \Sigma$ transition.

The optical system The laser beam (see fig. 3.1) passes through a slit where it is cleaned of haloes. It is deflected by 90° by means of a dielectric mirror and then focused by a lens (we have two lens with respectively 40 and 60 cm focal length), which is mounted on a slide permitting it to be translated along the beam direction from the focusing position (where the beam is focused onto the

3. EXPERIMENTAL SET-UP

target) away by about ± 15 cm. On the slide a graduated scale allows to read the distance between the target and the lens. The slide is used to change the energy fluence on the target. The focused beam finally enters the treatment chamber through a fused silica window and impinges on the target at 45° .

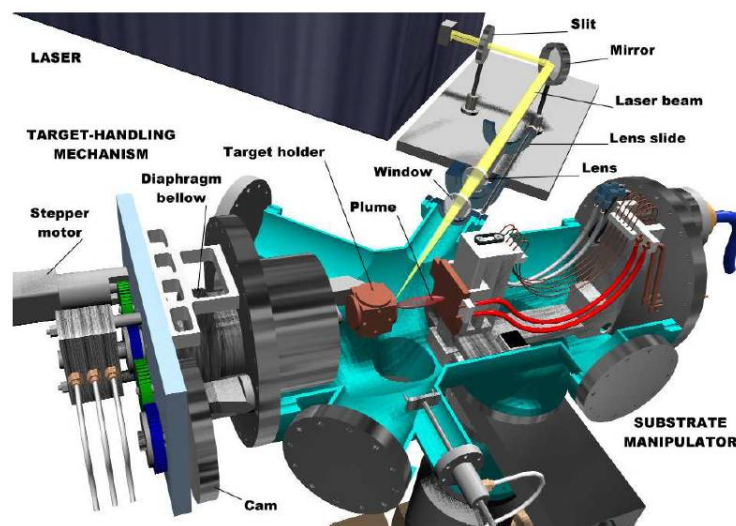


Figure 3.1: A schematic 3D view of the laser deposition apparatus -

The vacuum system In general, the thin-film-deposition process requires good vacuum conditions: in the PLD technique, gas-mixture atmospheres of relatively high pressure (of the order of 1 Pa) may be necessary in order to obtain complex stoichiometries. Our vacuum chamber was totally realized with CF flanges. The vacuum system is schematized in fig.3.2a. To preserve the turbomolecular pump, when an ambient gas is introduced into the treatment chamber, the pump itself is separated from the chamber by a gate valve and pumping occurs only through a bypass with a angle valve with adjustable transverse section (see fig. 3.2b). The gas mixture is introduced into the vacuum chamber through two mass-flow meters, thus maintaining constant the pressure and the partial pressure ratio.

The target-handling mechanism To obtain uniform target ablation, the laser beam must scan the target surface in such a way that the beam impinges on every surface element for the same duration. We use a circular target and we move it in the sense of a rotation about its symmetry axis (with a constant angular velocity,

3.1 Pulsed Laser Deposition apparatus

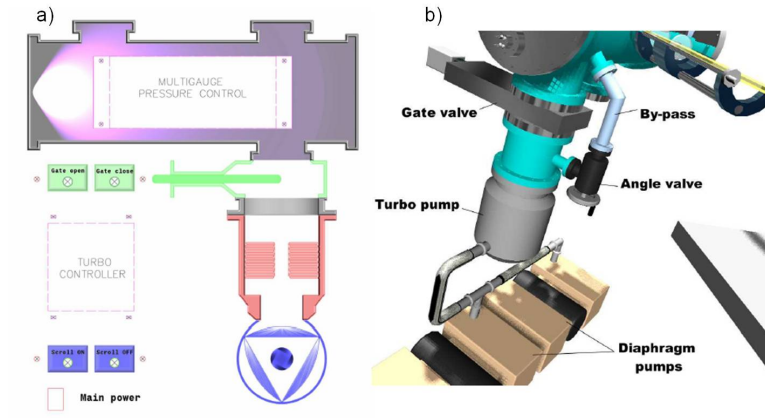


Figure 3.2: A schematic of the a) vacuum system, b) by-pass system -

combined with a horizontal transverse translation. The target holder inside the PLD chamber is shown in fig. 3.3

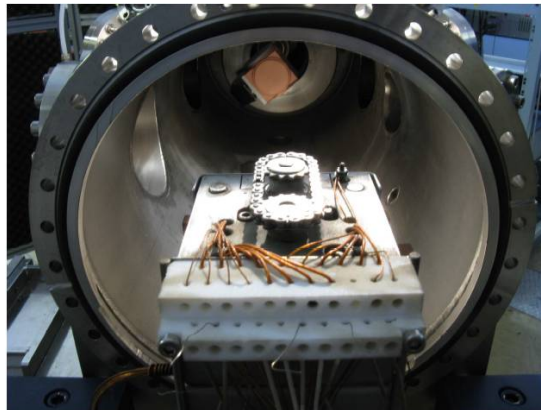


Figure 3.3: View of the PLD chamber -

The substrate-manipulator mechanism The sample-manipulator system is mounted on a multiport CF flange (see fig. 3.1). It is a mechanism with three degrees of freedom: one translation of 85 mm in the transverse horizontal (x) direction, one translation of 85 mm in the transverse vertical (y) direction and one translation of 300 mm in the longitudinal (z) direction. The motion is imparted through in vacuum stepper motors, mounted directly on the manipulator mechanism.

The substrate heating support A heating holder has been made to heat the substrate up to 350°C . A tungsten wire is connected to a power supply controllable

3. EXPERIMENTAL SET-UP

from outside. By varying the current applied to the wire we varied the temperature due to thermionic emission. The wire is placed behind a copper plate where the substrates are applied. We choose copper to ensure a uniform distribution of heat. Substrates are positioned over the copper plate and fixed to it by a stainless steel (SS) mask specially shaped. The SS is able to bear a temperature of 350°C . The heating support is in turn inserted in a bigger SS support, attached, but electrically isolated, to the substrate-manipulator system. In this way the W wire is isolated in an empty space in order to limit the heating of the vacuum stepper motors and of the other components into the PLD chamber.

3.1.1 Laser energy calibration

In deposition we are not interested in the energy of the pulse, but in the fluence (J/cm^2) reaching the target. As described before we can vary this fluence by changing the position of the lens on the slide. We just know the energy coming out from the laser, so we have to measure the losses of the beam during its path and the area of the laser spot on the target for different lens position.

We used a Scientech Astra Calorimeter AC50UV connected with a Scientech Vector H310 power meter. Power meter was configured in W mode (measurement of the power) and it was set in automatic range (it automatically changes the range of measured power). All the measurements were performed in air.

First we calibrated the internal energy monitor of the keypad in accordance with the external power meter by following the standard procedure suggested in the keypad manual. To check the successful of the operation we measured a few laser pulses with the external power meter and compared these values with those displayed by the energy monitor values. They didn't differ no more than 2-3 %, as expected.

Then we estimated the energy lost by the laser beam during its optical path. Once coming out from the laser the beam passes through the following elements: the adjustable slit, the dielectric mirror, the convergent lens (focal length=40cm) and the silica window. We measured with the power meter the energy of the beam after each of the listed elements for different pulse energy and for different repetition rate. Finally we estimated the total optical losses and checked it by measuring the energy of the beam passing at the end all the optical system (see fig. 3.4). The alignment of the beam is made by a secondary red laser.

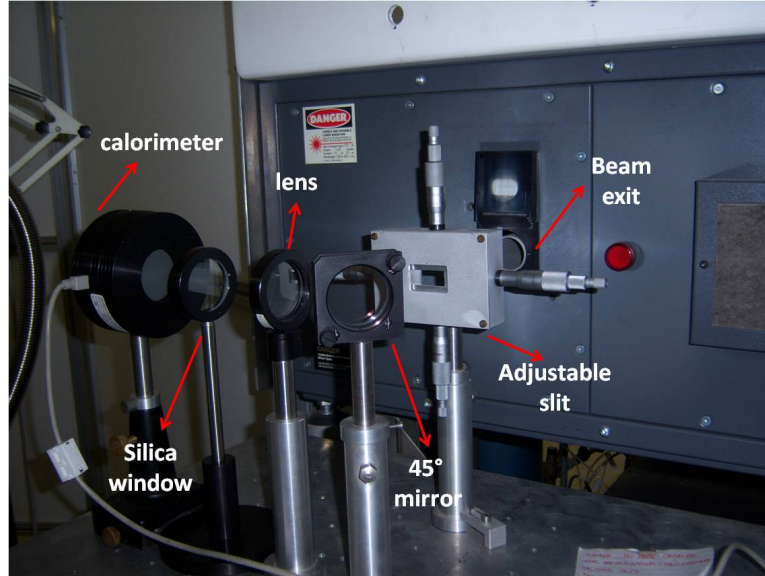


Figure 3.4: Measurement of the optical losses -

Finally the total losses was estimated around 30% of the laser pulse energy set by key-pad.

3.1.1.1 Determination of the fluence

To estimate the laser fluence on the target surface we focalize the beam on an external support where an Aluminum target was loaded at 45° with respect lo laser beam direction. The beam passes through all the optical system before reaching the Al target. The target can be moved forward and backward in order to vary the distance from the lens. We irradiated the target with few tens of pulses at different focalization of the beam and then analyzed the Al surface with Secondary Electron Microscopy (SEM) to measrure the size of crater formed on target surface after irradiation.

In measuring the area of the crater we should take into account that the size of the ablated area monotonously increases with increasing number of pulses. The dependence of crater size on number of pulses (N) is evident in fig. 3.5, where the dimension of the crater has been indicated for 1 and 50 pulses.

The dark contour surrounding the center of the crater in fig. 3.5 is due to the residual tail of the gaussian profile of the beam, part of the which is cut by the adjustable width, as shown schematically in fig. 3.6. So we measured the area of the crater including this

3. EXPERIMENTAL SET-UP

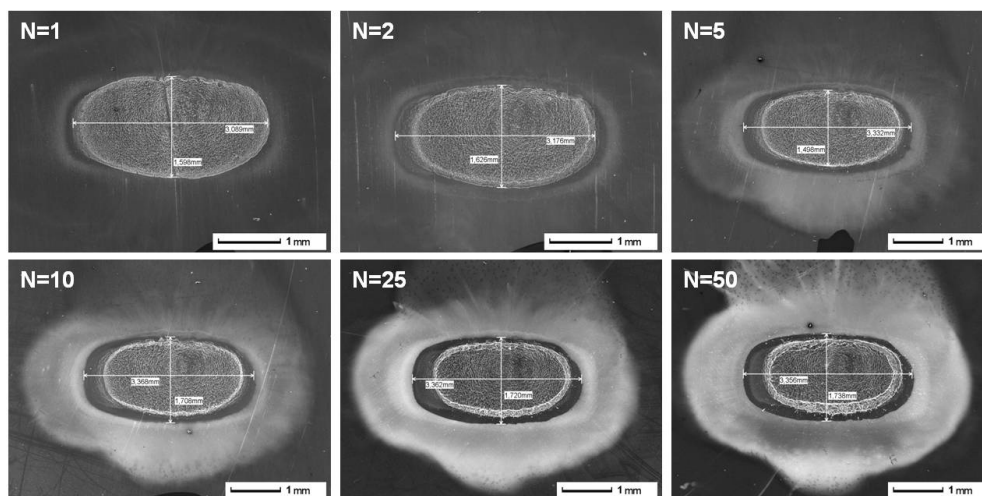


Figure 3.5: Measurement of the crater size on Al target for different number of pulses (N) - The distance of the target from the lens is 40 cm and the energy of the single laser pulse was is 200 mJ (without losses)

region.

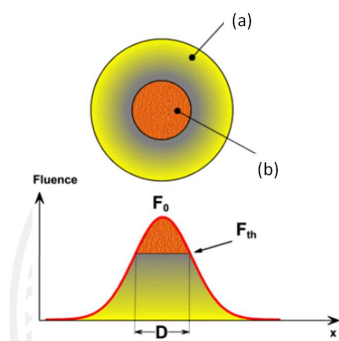


Figure 3.6: Gaussian profile of the laser beam and consequent crater shape -

Discolouration of the surface, appearing clear for $N=5$, is attributed to film growth via the inverse PLD process [14,15], while for $N=50$ Debris formation, i.e., re-deposition of the ablated material around the ablated area is visible.

Increasing the number of pulses the crater size increases until $N = 25 \div 50$. The observed behaviour has been explained in terms of an incubation model[1], where incubation means defect generation at sub-threshold fluence due to inhomogeneous intensity distribution of the laser beam (always present in experiment). Incubations will gradually reduce the damage threshold of the irradiated material according to:

$$\phi_{th}(N) = \phi_{th}(1)N^{S-1} \quad (3.1)$$

where S is the incubation parameter, while $\phi_{th}(1)$ and $\phi_{th}(N)$ are the single-pulse and N -pulse threshold fluences, respectively.

When ablating a sample with consecutive pulses of inhomogeneous fluence distribution (for homogenous intensity distribution $S=1$) incubation will result in a gradual increase in the dimension of the ablation crater. For N between 25 and 50 pulses the crater area seems to become constant, however a more detailed study, should be made (going on with the number of pulses). Indeed the increase of the size of the ablation crater is a logarithmic process, so one may be in error for a small number of pulses. Note also that changing the target materials, while keeping the other parameters (N , energy of the single laser pulse and lens-to-target distance) constant, the crater size change.

However an accurate determination of the crater size goes beyond our purpose. We do need to know exactly the absolute value of the fluence because we plan to compare properties of films deposited at different conditions to observe some trend.

So we performed different measurement keeping the number of pulses constant at $N=100$, and varying the position of the lens. The fluence was obtained dividing the energy of the laser pulse (keeping into account the optical losses) by the measured crater area. A final table was prepared which gives, for laser energy set at 200mJ, a set of lens-to-target distances (from 30.4 to 54.9 cm, with step of 0.5 cm) and the related fluences (the maximum fluence is $12J/cm^2$ while the minimum is $0.4J/cm^2$).

3.2 R.F. sputtering apparatus

Details on the sputtering deposition technique are given in appendix.

The plasma is powered by a R.F. PlasmaTherm HFS-500e power generator. We can load two targets inside the chamber. The substrates are loaded on a metallic substrate-holder that can be rotated from the outside of the sputtering chamber in order to locate the substrate over the target to be sputtered. Essentially the metallic substrate-holder is the anode of our system, while the target is the cathode. Between the target and the substrate there is a shutter to cover the target when performing a pre-sputtering for cleaning the target surface. An external view of the R.F. sputtering apparatus is given in fig. 3.7.

3. EXPERIMENTAL SET-UP



Figure 3.7: R.F. sputtering apparatus -

3.3 Apparatus for measurement of hydrogen

The apparatus for the gas-volumetric (GV) measurements of molecular hydrogen produced by catalysed chemical reactions was developed in our laboratories. We give here just a brief description. In figure 3.8 a schematic diagram of the experimental apparatus is reported. The reactor is coupled through a gas tube with an Erlenmeyer flask (capacity 1000 ml) containing water; the latter, in turn, is connected to a graduated cylinder (capacity 1000 ml), placed on an electronic precision balance (KERN GS 62001, readout 0.1 g, weighting range 6200 g, Sartorius) positioned lower with respect to the reactor and flask. The reaction chamber and the Erlenmeyer flask are assembled in a closed system. The decoupling between the flask and the cylinder is guaranteed by a stopcock. When the system is closed and the stopcock opened, the altitude difference between the flask and cylinder permits us to maintain a differential pressure between the two vessels (Bernoulli principle). Furthermore, overpressure inside the reaction chamber is prevented since the water level in the cylinder is always kept below the liquid level in the flask.

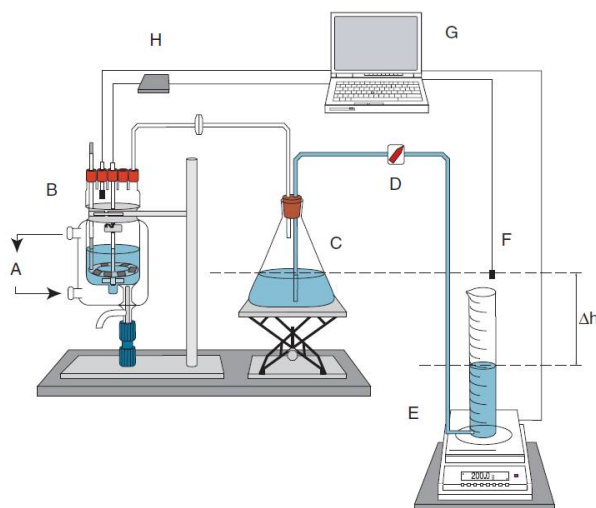


Figure 3.8: Schematic diagram of the experimental apparatus for GV analysis - (A) thermostatic water bath system, (B) reaction chamber, (C) Erlenmeyer flask with water reserve and elevator, (D) stopcock, (E) graduated cylinder and electronic balance, (F) external pressure sensor, (G) input/output board and acquisition software, (H) stepper motor controller. The height-difference Δh between the water level contained in the chamber/flask system and that in the cylinder is also indicated

3. EXPERIMENTAL SET-UP

When the catalyst (the Co-B films described in chapter) is dipped into the chemical solution (typically ammonia borane or sodium borohydride) contained in the reaction chamber, the hydrolysis process begins and H_2 starts to be produced. As a result of hydrogen evolution the pressure inside the reactor flask increases causing a water flow from the Erlenmeyer flask towards the graduated cylinder. The displaced volume of water, as a function of produced hydrogen, is continuously monitored by the electronic balance until the reaction ends.

We can obtain the number of moles of H_2 evolved by using the ideal gas law. At the beginning of the measure (t=0):

$$P_0V_0 = n_{air}RT \quad (3.2)$$

where $P_0 = P_{atm}$ and V_0 is the volume of air in the reactorflask system. During the measurement, and therefore with the production of gaseous hydrogen, the equation becomes.

$$P(t)V(t) = (n_{air} + n_{H_2})RT \quad (3.3)$$

where $V(t)$ is given by the sum of the initial volume of air and the volume of water displaced.

Hence, from equations 3.2 and 3.4 the expression for the estimation of the number of moles of hydrogen evolved can be obtained:

$$n_{H_2} = \frac{P(t)V(t)}{RT} - \frac{P_0V_0}{RT} \quad (3.4)$$

The mathematical expressions for time dependence of gas yield (%) and the rate ($ml\ min^{-1}\ g^{-1}$) as a function of the controlled variables are given by eq. 3.5:

$$Yield_{H_2} = \frac{n_{H_2}(t)}{4n_{BH_4-}} \quad (3.5)$$

where n_{BH_4-} is the number of moles of borohydride added (for ammonia borane the denominator is given by 3 times the number of moles of AB added), and

$$Rate_{H_2} = \frac{dv(t)}{dt} \quad (3.6)$$

is the rate of evolved hydrogen in millilitres per minute and grams of catalyst

4

Co-B nanoparticles synthesized by PLD

4.1 Introduction

Chemical hydrides are very attractive materials for hydrogen supply to the fuel cells at room temperature. Large amount of pure hydrogen gas is released during the hydrolysis of chemical hydrides in presence of certain catalysts. Alkaline sodium borohydride ($NaBH_4$) presents several advantages: (i) the high hydrogen storage capacity (10.9 wt.%); (ii) the good chemical stability of its alkaline solutions; (iii) the optimal control on H_2 generation rate by supported catalysts; (iv) the acceptable reaction rate even at low temperature; (v) the reaction product, borax, is environmentally clean and can be recycled [1]. Also ammonia borane (NH_3BH_3 , AB) has been identified as potential candidate for on-board hydrogen production mainly owing to its very high hydrogen storage capacity, 19.6 wt.%. AB can produce hydrogen by either hydrolysis or thermolysis and the end product, which is nontoxic and environmentally safe, can be used to regenerate AB [2, 3]. The hydrolysis reaction can be effectively controlled by the means of heterogeneous catalyst. Although noble metals like Pt, Rh, and Ru [4, 5, 6] are highly active catalysts for hydrogen production, their viability for industrial application is likely uncertain considering their cost and scarcity. Cheaper options in form of transition metals. Catalysts based on CoB seem to be interesting materials due to their low cost [7] and their high catalytic activity on hydrolysis reaction. Generally in the past, Co-B catalyst was studied in form of homogeneous powder which has

4. CO-B NANOPARTICLES SYNTHESIZED BY PLD

however some issues to be still solved, as the following: separation of the catalyst from the suspension after the reaction is difficult; the suspended particles tend to aggregate, especially when they are present at high concentrations; particulate suspensions are not easily applicable to continuous flow systems. On the other hand, Co-B in form of thin films will serve as an environmentally friendly "green catalyst" for being easily recovered, reused, and acting as suitable tool for ON/OFF switch. This thin film catalyst can also acquire better catalytic properties because of the inherent surface morphology and structure. Catalytic activity is mainly a surface effect and forming nano-catalysts is a potential route to increase the surface area. Pulsed laser deposition (PLD) has emerged as viable method for the production of nanoparticles on surface of the thin films.

4.2 Synthesis of the samples

Co-B powder catalyst, synthesized by the chemical reduction method, was used as the target material for the deposition of catalyst film by PLD. This powder was prepared by adding sodium borohydride, used as reducing agent, to an aqueous solution (0.05 M) containing cobalt salt ($CoCl_2$) under vigorous stirring. The black powder separated from the solution during reaction course was filtered and then extensively washed with distilled water and ethanol before drying at around 323 K under continuous N_2 flow. In order to be used as a target for the film deposition, the Co-B powder was cold pressed in form of cylindrical disks. Figure 4.1 shows a SEM images of the Co-B powder obtained after the synthesis process. SEM-EDS analysis on the powders gives the follow elemental composition: 34.4 at. % of Boron, 10 at. % of Carbon, 12.8 at. % of Oxygen and 42.8 at. % of Cobalt.

PLD was performed using KrF excimer laser (Lambda Physik) at the operating wavelength of 248 nm, pulse duration of 25 ns, and repetition rate f of 20 Hz. The ablation was carried out under vacuum condition with a base pressure of 2×10^5 Pa and target to substrate distance d_{t-s} was maintained at 4 cm. The substrates were kept at room temperature. Films were deposited on silicon substrates and on commercial Cu/C grids for the characterization and on glass substrates to test their catalytic activity.

Weight of the catalyst films was evaluated by measuring the weight of the glass slide

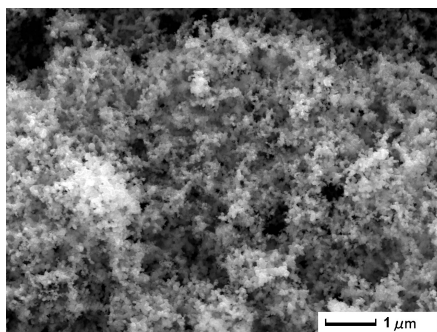


Figure 4.1: SEM micrographs of Co-B powders - Pressed powders will form our target

($25\text{mm} \times 75\text{mm}$) before and after deposition, and it was kept approximately constant (1 mg) for all the produced samples.

Samples were analyzed by SEM, TEM, XPS and AFM. Transmission Electron Microscopy (TEM) analyses were performed with a field emission FEI TECNAI F20 SuperTwin FEG-(S)TEM microscope operating at 200 kV equipped with an EDAX energy-dispersive X-ray spectrometer (EDS). Bright-field TEM (BFTEM) images, high-resolution TEM (HR-TEM) images, Fast Fourier Transform (FFT) image and selected area electron diffraction (SAED) patterns have been recorded. Commercial Cu grids were used as substrate to prepare samples for TEM analysis. X-ray photoelectron spectra were acquired using a SCIENTA ESCA200 instrument equipped with a monochromatic Al $K\alpha$ (1486.6 eV) X-ray source and a hemispherical analyzer. Topography of the Co-B film was analyzed by Atomic Force Microscopy (AFM) using silicon as a cantilever operating in the contact mode. The surface morphology of the samples was studied by scanning electron microscope (SEM-FEG, JSM 7001F, JEOL) equipped with energy-dispersive spectroscopy analysis (EDS, INCA PentaFET-x3) to determine the composition of the samples.

4.3 Characterization of the films

4.3.1 SEM results

We performed several deposition varying the laser fluence at 0.1, 0.3, 0.7, 1, 3, 6, 9, 12 J/cm^2 . In fig. 4.2 the surface of the different samples are compared.

4. CO-B NANOPARTICLES SYNTHESIZED BY PLD

Behind $1 J/cm^2$ fluence no single NP appears on the surface thus meaning that formation of NPs has a threshold energy. Indeed NPs are formed by phase explosion phenomena. As we mentioned before phase explosion happens only if the surface of the irradiated material reach a temperature near the critical point.

To have a further confirmation that droplets are ejected from the target and not by coalescence on the substrate, we produced three samples at $3 J/cm^2$ using respectively 5, 50 and 100 pulses. Results are reported in fig. 4.3 and shows the presence of NPs also for few number of pulses. Clearly increasing the number of pulses, the density of NPs increases.

4.3.2 TEM results

To go into the detail of the NPs structure we selected three fluences, namely 1, 3 and $9 J/cm^2$ to prepare samples for TEM analysis. We deposited the film on Cu/C grids using $f=20$ Hz, $d_{t-s}=4$ cm and about 1000 pulses. Before showing the results of analysis is important to underline the problem encountered in the quantification of B. In figure 4.4 an EDX spectrum was taken as example to explain the sensitivity of the EDX technique.

The background has to be subtracted for the spectrum analysis and gives an indication of the sensitivity of the EDX technique, which at low energies (e.g., below 0.3 keV, where is located the Boron K X-ray emission) is very low.

Others factors besides low detector sensitivity increase the difficulty in quantification of the actual B concentration:

- low fluorescence yield of very light elements;
- strong nearby C K signal from the TEM supporting grid;
- internal absorption of the X-ray emitted by Boron atoms due to the nearby heavy Co atoms (from the NPs) or Cu atoms from the TEM supporting grid.

4.3.2.1 Co-B film deposited at $1 J/cm^2$

From Bright-Field (BF-TEM) and Scanning-TEM (STEM) images it is possible to observe the presence of spherical particles having different dimensions (see fig. 4.5).

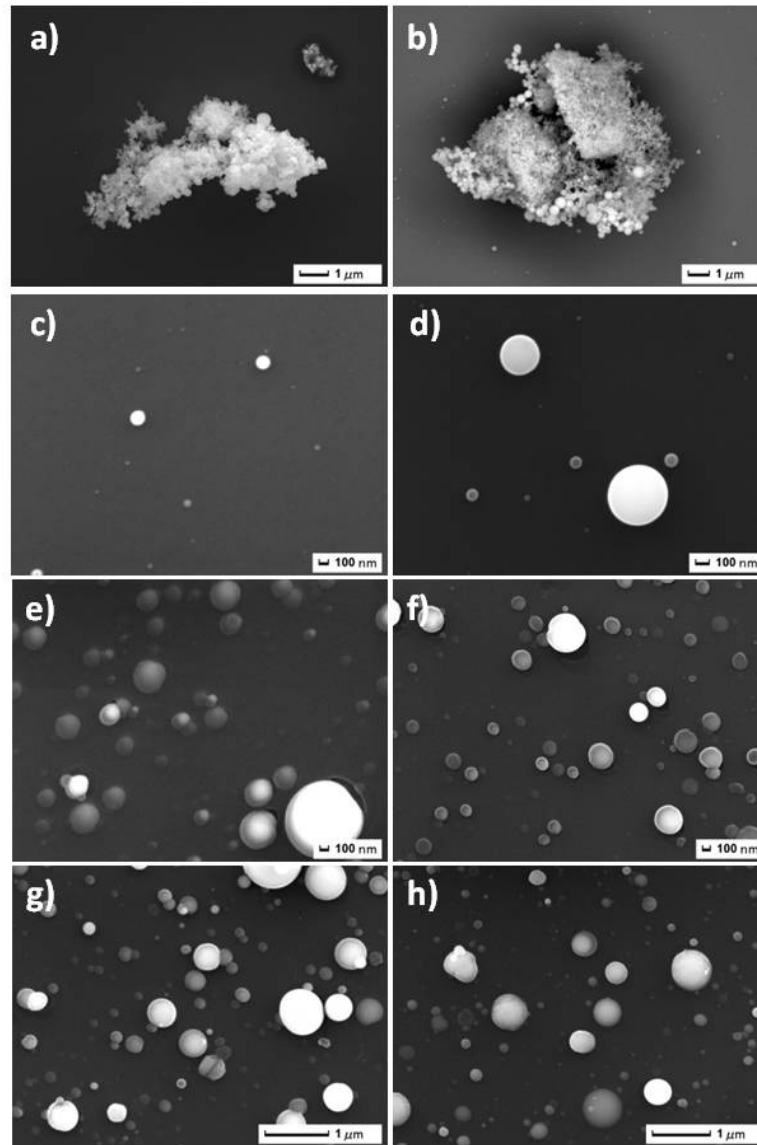


Figure 4.2: Co-B film deposited at different fluences - SEM micrographs of samples deposited at: a) 0.1, b) 0.3, c) 0.7, d) 1, e) 3, f) 6, g) 9, h) 12 J/cm^2

4. CO-B NANOPARTICLES SYNTHESIZED BY PLD

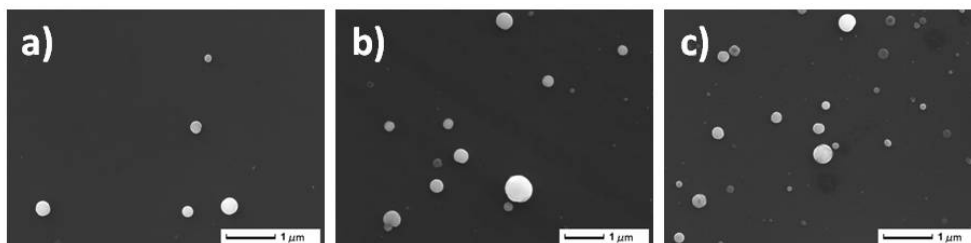


Figure 4.3: Co-B NPs - SEM micrographs of samples deposited using: a) 5, b) 50, c) 100 pulses

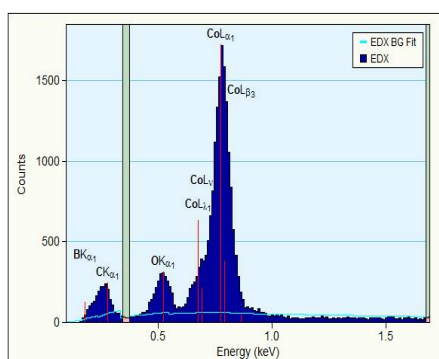


Figure 4.4: Typical EDX spectrum on a shell of a NP deposited at $3 J/cm^2$ - the position of the X-ray signals of the elements are shown (in red). The cyan line is the background

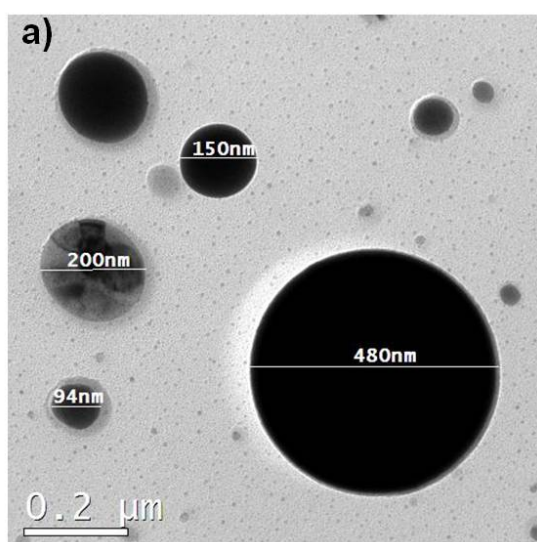


Figure 4.5: Bright field TEM images of Co-B film deposited at $1 J/cm^2$ - a) NPs of different size are visible, b) The presence of the shell was evidenced

The largest particles are surrounded by a shell, that sometimes is incomplete. The shell is constituted by light elements as visible in fig. 4.6. The thickness of the shell varies from a few nms to about 25 nm, and there is no apparent correlation between the dimension of the NPs and the thickness of the surrounding shell.

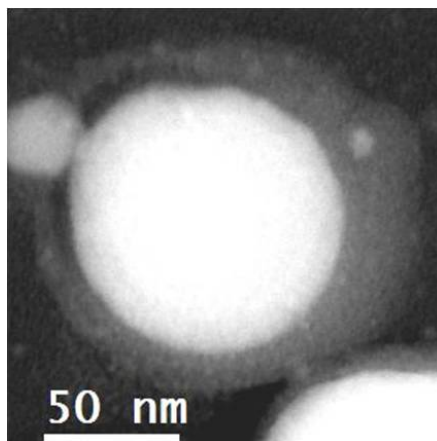


Figure 4.6: STEM images a the core/shell NP - an heavy element gives a brighter contrast

There is also a very broad size distribution including particles having a mean diameter $\langle D \rangle = (7.0 \pm 1.2)nm$, uniformly dispersed in in all the carbon film. The areal density of the NPs in the film is summarized in table 4.1. The Selected Area Electron Diffraction (SAED) and the relative radially averaged intensity function (see fig. 4.7) show that the most probable phase of this NPs is Co-hcp. Fast Fourier Transform (FFT) analysis of the High Resolutio (HR) images has confirmed that NPs are poly-crystalline and are formed by Co-hcp.

NPs size	NPs density ($NPs/\mu m^2$)
$D < 10nm$	100
$10nm < D < 80nm$	13
$80nm < D < 300nm$	7
$D > 300nm$	0.5

Table 4.1: areal density of the NPs obtained at $1 J/cm^2$ as a function of their dimensions - NPs have a broad range distributions

EDX compositional spectra were acquired by focusing the electron beam on different regions shown in fig. 4.8. The results are summarized in table 4.2.

4. CO-B NANOPARTICLES SYNTHESIZED BY PLD

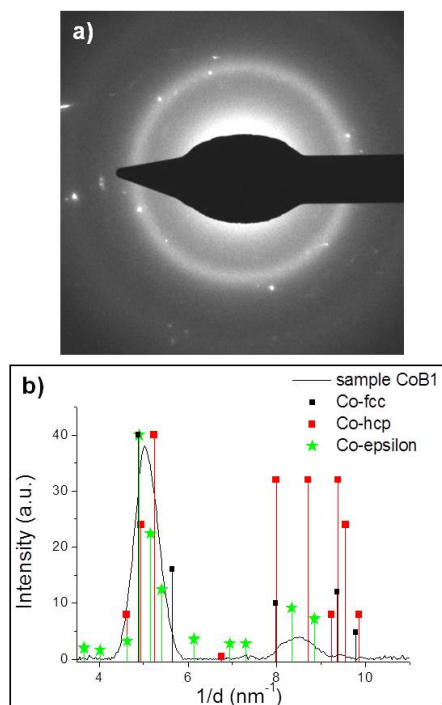


Figure 4.7: a) Selected Area Electron Diffraction (SAED) and, b) the relative radially averaged intensity function of small NPs obtained at 1 J/cm^2 - the most probable phase of this NPs is Co-hcp

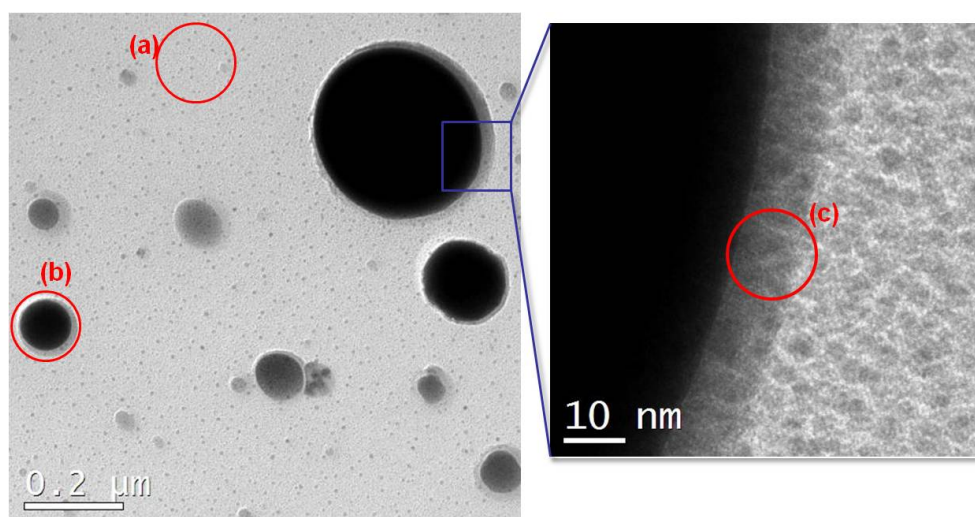


Figure 4.8: Different region where EDX compositional spectra were acquired - a) small NPs, b) big NP, c) shell of the big NP

Region:	a (small NPs)	b (big NP)	c (shell)
<i>Element</i>	<i>Atomic %</i>	<i>Atomic %</i>	<i>Atomic %</i>
B(K)	0	0	0
O(K)	40	26	37
Co(K)	60	74	63
O/Co=	0.67	0.35	0.59

Table 4.2: Results of EDX compositional spectra for 1 J/cm^2 sample - Note that the B concentration is set to 0 when the quantification is unreliable

The electron beam was focused with a FWHM of about 2-3 nm on core and then on the shell of the big NP to perform EDX-STEM analysis in order to detect the signal of Boron. However Boron X-Ray signal can be considered negligible both on the core and on the shell of the NP. The strongest compositional signal on the shell is from Co and O so we could support the formation of some Co oxide.

4.3.2.2 Co-B film deposited at 3 J/cm^2

As the previous sample there are spherical NPs having different sizes. Also in this case some of them are surrounded by incomplete shells. To better investigate the core-shell structure of the NPs images at different tilt (α) of the sample stage were acquired (see fig. 4.9), confirming that the shell is incomplete.

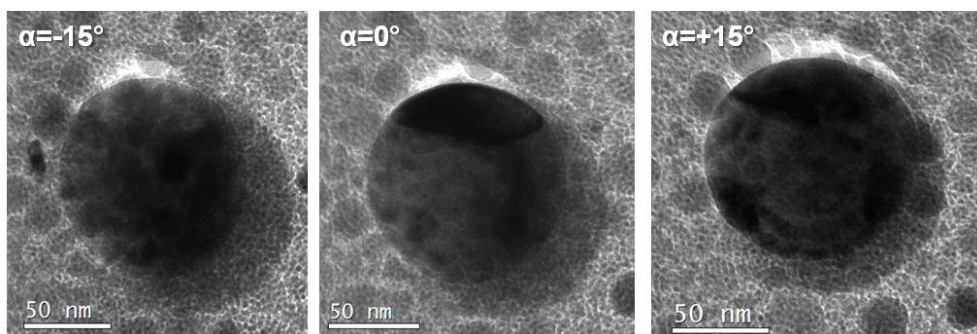


Figure 4.9: Bright field TEM images acquired at different tilt of the sample stage - the shell surrounding the NP is not complete

The thickness of the shell varies from a few nm to about 35 nm, and also in this sample there is no apparent correlation between the size of the NPs and the thickness of the surrounding shell. Moreover STEM confirms that the shell is constituted by light

4. CO-B NANOPARTICLES SYNTHESIZED BY PLD

elements.

The NPs are observed to be well-dispersed in the matrix of light element as shown in fig. 4.10.

Table 4.5 reports the areal density of the NPs as a function of their dimensions for this sample.

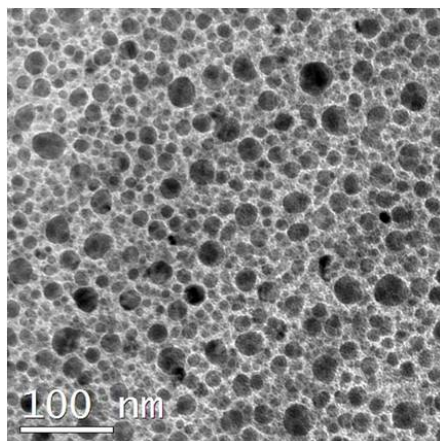


Figure 4.10: Bright field TEM on the small NPs for $3 J/cm^2$ - For details look at values reported in table 4.5

NPs size	NPs density ($NPs/\mu m^2$)
$D < 30nm$	320
$30nm < D < 100nm$	2
$100nm < D < 500nm$	2.2
$D > 500nm$	0.6

Table 4.3: areal density of the NPs obtained at $3 J/cm^2$ as a function of their dimensions - NPs have a broad range distributions

Smaller NPs are bigger with respect to the previous sample having $\langle D \rangle = (11 \pm 5)nm$.

HR-TEM reveals that small NPs are poly-crystalline and the most probable crystalline phase is Co-hcp.

Again the EDX compositional spectra was acquired on different regions, shown in table 4.4. The EDX spectrum of the shell is reported in fig. 4.11. Unlike table 4.2 in this case a weak Boron X-ray signal is present.

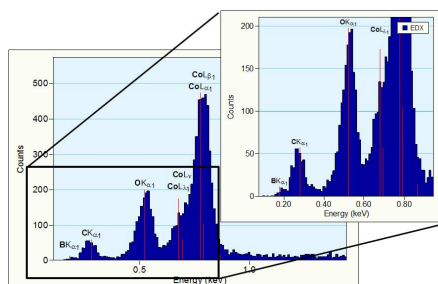


Figure 4.11: EDX spectrum of the shell of one NP for $3 J/cm^2$ - For details look at values reported in table 4.2

Region:	a (small NPs)	b (big NP)	c (shell)
<i>Element</i>	<i>Atomic %</i>	<i>Atomic %</i>	<i>Atomic %</i>
B(K)	2	0	0
O(K)	30	32	5
Co(K)	68	68	95
O/Co=	0.4	0.5	0.1

Table 4.4: Results of EDX compositional spectra $3 J/cm^2$ sample - A weak signal of B is detected

However performing EDX-STEM analysis Boron X-Ray signal is not always detectable, neither in the core nor in the shell.

4.3.2.3 Co-B film deposited at $9 J/cm^2$

Presence of spherical NPs having different sizes is again revealed, but the number of NPs surrounded by a shell is fewer with respect to the previous samples. The thickness of the shells varies from about few nm to about 20 nm, as visible in fig. 4.12.

Table 4.5 reports the areal density of the NPs as a function of their sizes.

NPs size	NPs density ($NPs/\mu m^2$)
$D < 30nm$	270
$30nm < D < 100nm$	3
$100nm < D < 500nm$	1.5
$D > 500nm$	0.3

Table 4.5: areal density of the NPs obtained at $9 J/cm^2$ as a function of their dimensions - NPs have a broad range distributions

4. CO-B NANOPARTICLES SYNTHESIZED BY PLD

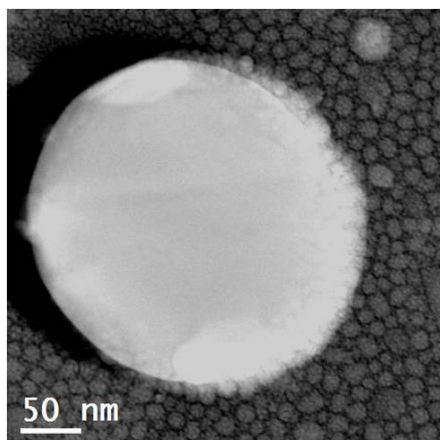


Figure 4.12: STEM images of core/shell NP obtained at $9 J/cm^2$ - the shell surrounding the NP is smaller with respect to the other samples

As the $1 J/cm^2$ the Boron X-Ray signal is below the detection limit of EDX, as reported in table 4.6

Region:	a (small NPs)	b (big NP)	c (shell)
<i>Element</i>	<i>Atomic %</i>	<i>Atomic %</i>	<i>Atomic %</i>
B(K)	0	0	0
O(K)	32	14	33
Co(K)	68	86	67
O/Co=	0.47	0.16	0.50

Table 4.6: Results of EDX compositional spectra $9 J/cm^2$ sample - No signal of B is detected

4.3.2.4 Summary of TEM results

We can summarize the above results in these key-points:

- In all the samples there is the presence of spherical NPs having different sizes;
- Larger NPs are poly-crystalline and are formed by Co-hcp;
- Most of the largest NPs are surrounded by a partially complete shell, whose thickness is not constant;

- In the sample 9 J/cm^2 the number of Cobalt NPs covered by a shell is smaller with respect to the previous ones;
- Presence of smaller NPs uniformly dispersed on the carbon film;
- Small NPs are crystalline and are formed by Co-hcp;
- The average size of small NPs increases with increasing the laser energy density;
- Concerning the compositional analysis by EDX Spectroscopy we have to keep in mind all the experimental problems underlined in the introduction about the Boron quantification. Anyway, it is possible to observe:
 - Presence of Oxygen X-Ray signal on the small NPs dispersed on the carbon film (presence of amorphous Cobalt Oxide can not be excluded);
 - The only sample which shows a detectable Boron X-Ray signal on some shell is the one at 3 J/cm^2 ;
 - No detectable B signal has been found in the other sample or in the smaller NPs (also in the sample at 3 J/cm^2).

According to the last points on EDX analysis, the formation of Co-oxide or Co-B-oxide seems to be the most probable mechanism for the shell formation.

4.3.3 XPS results

XPS analysis was performed both on powders forming the target and on samples obtained by PLD.

4.3.3.1 XPS on the powders

Four different spectra were acquired: B1s, C1s, O1s, Co2p.

Before starting the normal routine of XPS analysis the signal of the peak of C1s was controlled in order to decide whether or not compensate the charge during the acquisition phase. The sample showed a weak superficial charge effect during irradiation, that remained constant until the end of the control sequence, so the analysis phase was carried on without any charge compensation by the flood gun.

A successive charge correction of +0.5 eV has been made in the analysis data phase.

4. CO-B NANOPARTICLES SYNTHESIZED BY PLD

The value for charge corrections, kept the same for all the acquired spectra, was estimated by comparing the experimental position of metallic Co with the position of metallic Co reported in literature. A check of the correction was made verifying the position of C1s and O1s after the charge correction.

We refer to Perkin-Elmer manual and to the web site www.lasurface.com for the identification of peak positions.

The survey of the XPS analysis is reported in fig. 4.13, while we just summarize the result obtained in the single spectra.

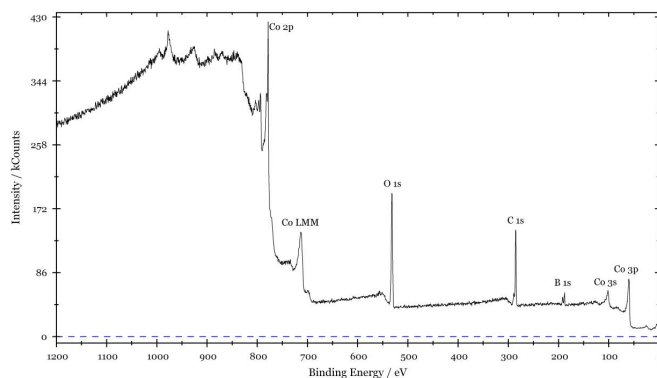


Figure 4.13: XPS survey (from 1200 to 0 eV) of the Co-B powders - Metallic Co and B and their respective oxide are visible

The C1s spectra shows an intense peak centered at a binding energies (BE) of 284.8 eV related to the existence of metallic C from contamination. A peak at the BE of 288.8 eV was also detected, and indicates oxidized C.

The B1s spectra shows the co-existence of a sharp peak at the BE of 187.7 eV, indicating the presence of metallic B, and of a smaller and broad peak at a BE of 191.5 eV related to boron oxides.

The Co2p spectra shows the co-existence of the characteristic doublet of metallic Co and of the doublet structure of oxidized Cobalt. We have to note that the intensities of the cobalt peaks are of the order of MCounts, while for the other line the intensities reach only kCounts.

The O1s spectra show a broad and asymmetric peak. The broadening of the peak may be a further indication of the charge effect in the sample, or may be due to the chemical environment of the O atoms.

4.3.3.2 XPS on the films

We analyzed three different samples synthesized by PLD, namely 3, 9 and 12 J/cm^2 . It was not necessary to compensate the charge effect during the analysis by using the flood gun.

To evaluate the requirement of a charge correction during data analysis we follow the same procedure adopted for the analysis of powder. If not possible (for the sample at 3 J/cm^2) we take as reference only the position of C1s and O1s peaks. The following charge corrections were finally applied:

- 0.15 eV for sample at 3 J/cm^2
- 0.5 eV for sample at 9 J/cm^2
- 0.5 eV for sample at 12 J/cm^2

Furthermore, for each spectrum, we calculated the background using the Shirley model (see appendix) in order to subtract it from the experimental spectra. The Shirley background was calculated over all the acquisition spectra, except from the Co2p, where it was necessary to reduce that spectra.

We operated the following fit procedure for the four spectra of all the samples:

O1s 3 singolets each relating respectively to the: C-O, the B-O and the Co-O bonds;

C1s 4 singolets: the first (at lower BE) taking into account the C contribution in compound containing Co-C bonds and in B_4C compound containing C-C bonds, the second relating to the contribution of graphitic C and to the contribution of C in compound having B-C bonds, and the last two related to oxidized C;

B1s 3 singolets: one for the contribution of elemental B and of B present in compound having B-Co bonds, one for the compound containing B-C bonds, and the last one related to oxidized B;

Co2p 2 doublets: the first related to the contribution of metallic Co and of Co coming from compounds having Co-B bonds, the second for the oxidized Co (peaks of the second doublet are accompanied by characteristic shake-up satellites). The contribution of the Co-O bonds was then estimated by summing the intensities of the fundamental doublet and of the satellite doublet.

4. CO-B NANOPARTICLES SYNTHESIZED BY PLD

Here we show just the XPS results for samples deposited at 12 J/cm^2 (see from fig. 4.14 to fig. 4.17)

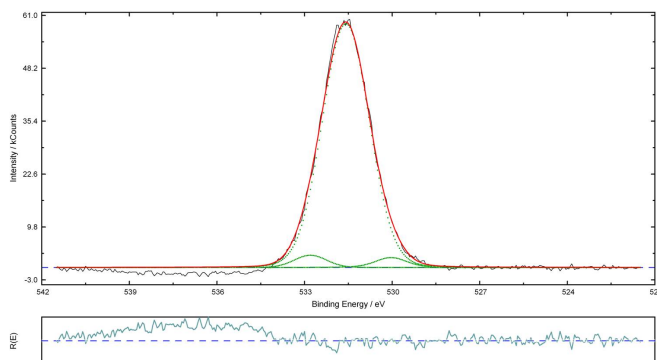


Figure 4.14: O1s spectra of XPS spectrum for sample at 12 J/cm^2) - Data are in black line, fit line is in red, and singlets used for fitting are in dashed lines. On the bottom of the spectra there is the residual of the fit

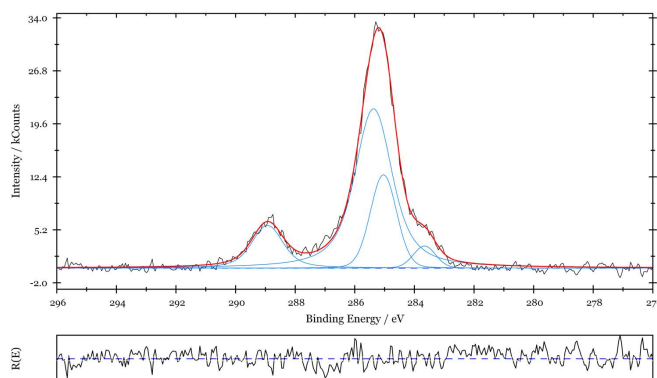


Figure 4.15: C1s spectra of XPS spectrum for sample at 12 J/cm^2) - Data are in black line, fit line is in red, and singlets used for fitting are in blue lines. On the bottom of the spectra there is the residual of the fit

The qualitative results obtained from the analyzes are given below.

Sample at 3 J/cm^2 No peak related to metallic B was observed, while a peak indicating the presence of oxidized B at 192.5 BE is evident. In the Co2p spectra there is the doublet structures typical of Co oxides. The C1S spectra reveals the presence of both graphitic C (peak at BE of 284.5 eV) and oxidized C (peak at 288 eV) due to contamination.

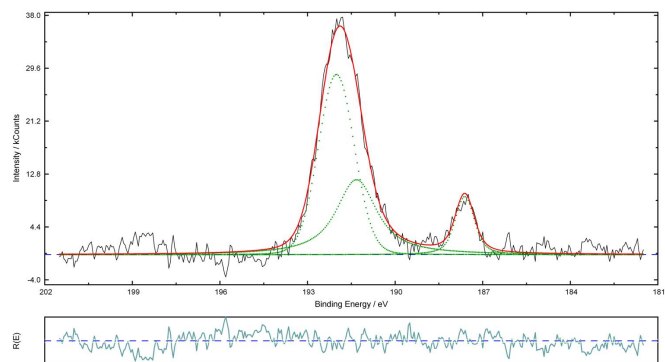


Figure 4.16: B1s spectra of XPS spectrum for sample at $12 J/cm^2$ - Data are in black line, fit line is in red, and singlets used for fitting are in dashed lines. On the bottom of the spectra there is the residual of the fit

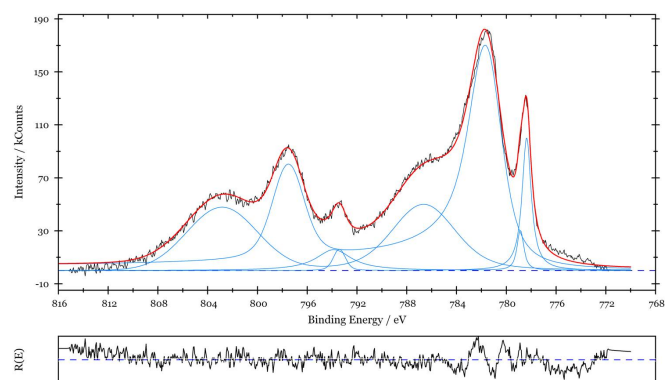


Figure 4.17: Co2p spectra of XPS spectrum for sample at $12 J/cm^2$ - Data are in black line, fit line is in red, and doublets used for fitting are in blue lines (also satellite peaks appears). On the bottom of the spectra there is the residual of the fit

4. CO-B NANOPARTICLES SYNTHESIZED BY PLD

Sample at 9 J/cm^2 Also in this case a peak at BE of 192.5eV indicates the existence of oxidized B, but the peak relative to metallic B starts to emerge and most probably it comes from compound containing Co-B bonds. In the Co2p spectra appears the doublet characteristic of the metallic Co together with the doublet structures of the Co oxides. The C1s spectra shows again the presence of both graphitic and oxidized C coming from contamination, but also a small signal indicating the presence of C bonded with a metal.

Sample at 12 J/cm^2 In the B1s spectra the peak related to oxidized B is still dominant, but the presence of metallic B, related to compound containing Co-B bonds becomes even more important. In the Co2p spectra the doublet of metallic Co prevails on the peaks related to oxidized Co, that however are still present. Finally in the C1s spectra remains the presence of the graphitic and oxidized C from contamination, but the contribution of the C bonded with a metal becomes more important.

4.3.3.3 Summary of XPS results

The BE of the two peaks appearing in the B1s spectra is lower in the powders than in the synthesized films. The difference is more evident for the peak related to oxidized B. On the contrary both the positions of the doublet of metallic Co and of oxidized Co are the same for powders and films.

XPS analysis shows also an evolution of the film surface by increasing the laser fluence. Indeed the signal of Co and B increases with fluence respect to the signal of O and C. Moreover for fluences higher than 3 J/cm^2 metallic Co and B appears together with oxidized Co and B, and their presence is more evident at higher fluences. This is evidenced in fig. 4.18, where the area under the peaks obtained by the fitting procedure were plotted versus fluence used in deposition.

4.3.4 AFM results

AFM images of samples deposited at 1, 3, 9 and 12 J/cm^2 were taken. Fig. 4.19 presents the AFM image taken on film at 1,3, 9 and 12 J/cm^2 . Together with STEM results these images indicate that the Co NPs synthesized are only partially embedded

4.4 Discussion on samples characterization

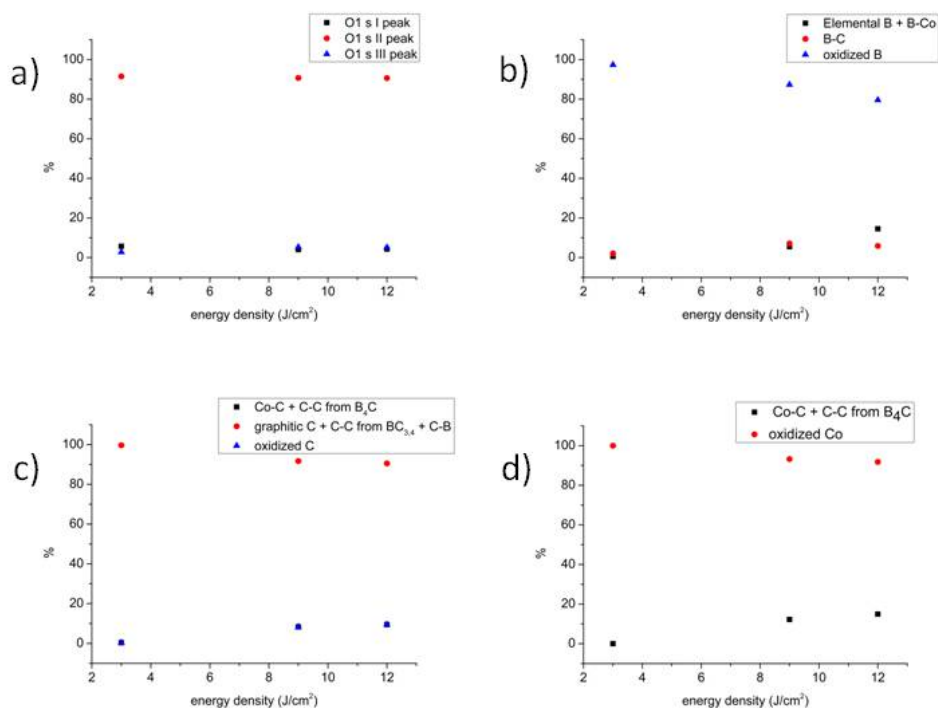


Figure 4.18: XPS fit peaks area vs fluence - a) O1s, b) B1s, c) C1s, d) Co2p

in the light element matrix and forms 3-dimensional surface, thus providing high active surface area, useful for the catalysis reaction.

4.4 Discussion on samples characterization

According to TEM analysis the Co-NPs, with narrow size distribution and distinct spherical shape, are well-dispersed in the matrix of light element. As explained before the detection of B is difficult, however we expect to have boron in the synthesized films because it is present in the target. This is confirmed by XPS analysis that shows the presence of B in all the samples, at least on the first nm of the film surface. So we can assume that the light element matrix is constituted of B or B oxide, even if we must consider the possible presence of C also.

Carbon peaks appear in XPS spectrum not only at the typical position for environmental contamination, but also bonded with metals. SEM-EDS on powders of Co-B clearly detect the presence of C and finally the signal of C is revealed in the shell of the NPs also by EDX-TEM (see fig. 4.11). So a portion of the Carbon in the films comes from

4. CO-B NANOPARTICLES SYNTHESIZED BY PLD

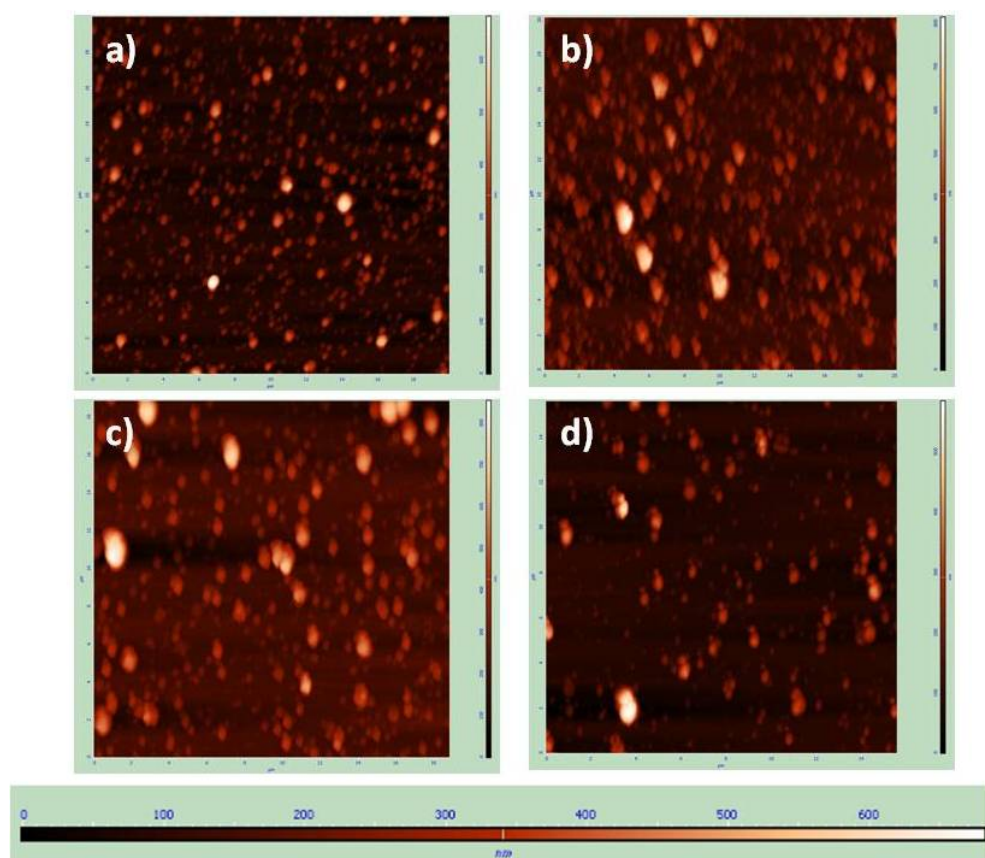


Figure 4.19: AFM images of samples at a) 1, b) 3, c) 9, d) 12 J/cm^2 - Color scale in nm is reported

4.4 Discussion on samples characterization

deposition process, and can contribute to the formation of the light element matrix in which the NPs rest.

XPS analysis for samples deposited at 9 and 12 J/cm^2 exhibit the co-presence on the surface of both metallic Co and B and their respective oxides, while for lower fluence there are only the peaks related to oxidized Co and B. Moreover increasing laser fluence the XPS shows an increase of the Co and B signals with respect to the signals coming from O and C.

Information given by XPS refers to a large area of the surface (about $2mm^2$) and so we can not attribute the signal of metallic B exclusively to the shell of the NPs or to the light element matrix. Indeed even if the density of big NPs is quite low respect to the small ones, their surface area is bigger and so their contribution to the total signal of B, in XPS analysis, is comparable to that of small NPs. However we can make few comments.

TEM analysis for samples at 9 J/cm^2 indicates that the thickness of the shell is lower and also the number of particles covered by the shell decrease with respect to lower fluences. Moreover TEM analysis reveals that increasing the laser fluence the average particle diameter D of the small NPs grows. Finally SEM micrographs shows that the particle density of big NPs increases with increasing laser fluence.

Increasing the fluence the presence of the shell decrease and the signals from metallic B and Co emerge. So we can assume that the shell of the NPs is formed by oxide of Co or B (remember that TEM-EDX reveals also a weak signal of B in the shell).

But is not only the metallic contribution of both B and Co to increase with fluence, but also the total signal of Cobalt and Boron with respect to Oxygen and Carbon. The contribution of Co may increase because of an higher density of NPs on the surface of the film. Similarly the signal of B increases with fluence, indicating again that B can contribute to the shell of the NPs.

HRTEM shows that Co-NPs are polycrystalline, as confirmed by FFT and SAED pattern (see fig. 4.7). This result suggests that each Co-NP is composed of nano-size domains, with a set of atomic planes, separated by grain boundaries. These boundaries are linear defects in polycrystalline nanoparticles with a width of 0.5–1.0nm containing atoms with lower coordination number as compared to atoms in the ideal crystallites and therefore these grain-boundaries regions are highly catalytic active sites with basic, acidic or redox functionality [8].

4. CO-B NANOPARTICLES SYNTHESIZED BY PLD

Furhtermore the examination of XPS spectra of Co and B reveals the existence of Co-B bonds. Electron transfer from alloying B to vacant d-orbital of metallic Co, makes B electron deficient and Co enriched with electrons. This interaction may stabilize the Co-NPs by avoiding coalescence and Ostwald ripening, with B acting as an atomic diffusion barrier.

The mechanism of NPs formation is here attributed to the phase explosion process that occurs under extreme conditions of high temperature and pressure produced by the laser pulses irradiating targets in vacuum. We know that phase explosion process occurs in a superheated liquid near T_c , so we suppose that the emitted liquid would have a homogeneous Co-B composition. This means that during the liquid flight from target to substrate, or just on the substrate, cooling processes will occur that lead to phase separation and the formation of a film of Co-NPs embedded in a light element (possibly boron or boron oxide) matrix.

During the laser ablation, as the deposition progresses, the NPs of the target material may also tend to grow on the surface of substrate by diffusion-related coalescence and Ostwald ripening processes [9]. Therefore, during the synthesis of NPs using PLD, the number of laser pulses is carefully selected to obtain deposits not fully covering the surface of the substrate in order to limit the influence of particles coalescence on the substrate. However, this nanoparticles arrangement will not be able to serve catalysis reaction on macroscopic scale. But with the present synthesis strategy, starting from targets of pressed Co-B powder, multiple layers were successfully deposited with better dispersion of Co nanoparticles in the B matrix that avoids surface clustering.

Moreover by just varying the laser fluence in PLD it is possible to tune both size and density of Co NPs.

4.5 Catalytic activity measurements

For catalytic activity measurements, a solution of ammonia borane (AB) and sodium borohydride (SBH) (SigmaAldrich) with 0.025M was prepared. The generated hydrogen volume was measured through a gas volumetric method in an appropriate reaction chamber with thermostatic bath, wherein the temperature was kept constant within accuracy of ± 0.1 K. A detailed description of the measurement apparatus is given in section 3.3.

4.5 Catalytic activity measurements

In a typical experiment, catalyst film supported on a glass substrate was introduced in the SBH (200 ml, 0.025M) or AB solution (150 ml, 0.025 M), at 298 K, and the generated H_2 yield was evaluated by accurately measuring the weight of water displaced by the hydrogen volume produced during the reaction course.

In all the runs, the catalyst was placed on the appropriate device inside the reaction chamber and the system was sealed. Catalyst film was added to 150 ml of the above AB solution, at 298 K, under continuous stirring.

Results obtained are reported in fig. 4.20 and 4.21.

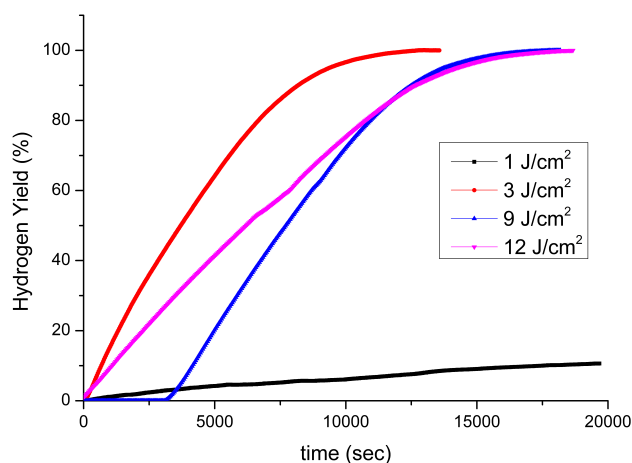


Figure 4.20: Hydrolysis of SBH solution (0.025 M) at 298K - Hydrogen generation yield as a function of time

The figures clearly show that the Co-B film catalysts are highly active and produce hydrogen instantaneously as soon as they come in contact with the hydride solutions. However, the catalyst synthesized at laser fluence of $3 J/cm^2$ exhibits higher catalytic activity, for both SBH- and AB-reactions, as compared to that produced at $9 J/cm^2$ by using same amount of catalyst (about 1 mg). Both the Co-B catalysts are able to produce the expected amount of H_2 gas (100% yield) from the hydrolysis reaction of $NaBH_4$. On the contrary, the total amount of H_2 (95%), generated through hydrolysis of AB by catalyst deposited with low energy density, is greater than that generated by catalyst synthesized with $9 J/cm^2$ (85%).

The lower catalytic activity exhibited by the catalyst deposited with higher energy

4. CO-B NANOPARTICLES SYNTHESIZED BY PLD

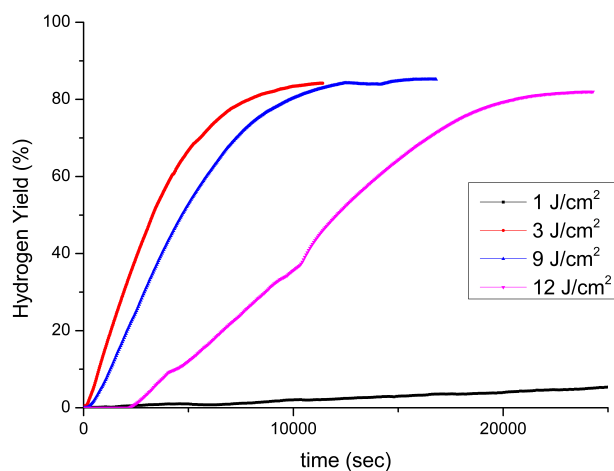


Figure 4.21: Hydrolysis of AB solution (0.025 M) at 298K - Hydrogen generation yield as a function of time

density can be attributed to the bigger average size of Co NPs as compared to that produced with $3 J/cm^2$. This is consistent with the fact that the low size of NPs favors a large surface-to-volume atomic ratio, a necessary requirement for catalysis that indeed is a surface process.

The sample at $1 J/cm^2$ has the smallest NPs, but their area density is lower compared to the other samples, as reported in table 4.5 . This is because a fluence of $1 J/cm^2$ is near the threshold value of fluence to have phase explosion in our conditions, as can be deduced from the SEM images in fig. 4.2.

The functionality of the synthesized Co-B catalysis is attributed to the following features:

1. Co NPs, with average size of a few nanometers, provide the best situation to have a large amount of surface active atoms over NPs with respect to bulk atoms: a condition that favors catalytic efficiency;
2. Co NPs have polycrystalline structure and include several grain boundaries containing low coordinated atoms which are able to act as active sites for catalytic reaction. The peculiar electronic properties of such boundary sites are also expected to play a role in chemical reactivity;

3. The interaction between surrounding B matrix and Co NPs plays a vital role not only for better dispersion of NPs but also in protecting against oxidation and stabilizing against coarsening;
4. Co NPs form rough surface structure, as observed by AFM, thus providing an active surface area higher than a flat film.
5. In electron-enriched Co NPs, the excess electrons contribute to the hydrolysis reaction by providing the charges required by the hydrogen atom to detach from the catalyst surface, thus establishing optimum interaction with the reactant and product molecules.

4.6 Improvement in catalytic activity

In order to improve the catalytic activity of the Co-B film we deposited it on an highly irregular and porous carbon film instead that on the plane glass substrate. In this way we wanted to effectively improve the initial surface area and obtain better dispersion of NPs.

4.6.1 Synthesis and characterization of the samples

Carbon supported Co-B film catalyst was synthesized in two steps: 1) by first depositing carbon film by PLD, on a glass substrate, using a laser fluence of 12 J/cm^2 and varying Ar pressures ranging from 10 to 50 Pa to obtain different surface roughness; 2) by depositing of Co-B nanoparticles-assembled film over these carbon films in vacuum with similar laser parameters used to deposit unsupported Co-B film (we choose a fluence of 3 J/cm^2).

Weight of the catalyst loading was evaluated as before, by measuring the weight of the glass slide (76 x 46 mm) with carbon film, before and after deposition of Co-B film, and it was kept approximately constant for all the produced samples (10 mg). Films were deposited on silicon substrates for the characterization and on glass substrates to test their catalytic activity.

In fig. 4.22 SEM images of Co-B catalyst powder and both films (unsupported and C-supported) synthesized are shown. The SEM images of catalyst powders show typical

4. CO-B NANOPARTICLES SYNTHESIZED BY PLD

particle-like morphology with spherical shape and average size of a few nanometers. However, because of the high surface energy related to these particles, they tend to agglomerate as observed in the SEM image. As seen in fig. 4.22, the surface of unsupported Co-B catalyst films exhibit a nanoparticles-assembled structure made of well dispersed spherical particles with size ranging between 50 to 300 nm.

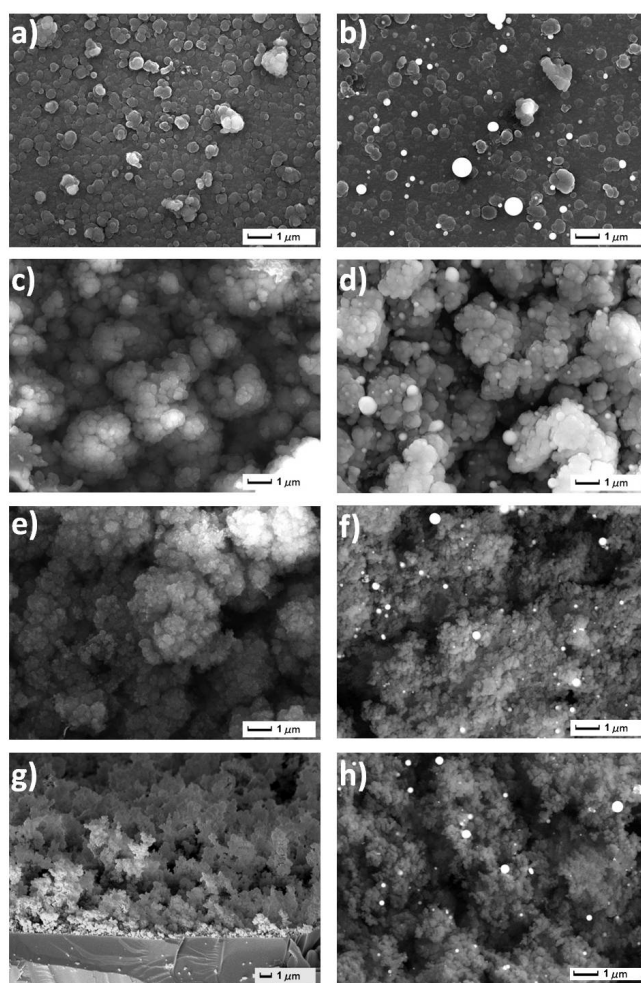


Figure 4.22: SEM micrographs of carbon film and Co-B supported C film deposited under different Ar gas pressure - a,b) 20, c,d) 30, e,f) 40, g,h) 50 Pa

Microstructures ranging from flat to highly irregular and to porous are clearly visible. The carbon film deposited at low Ar pressure (20 Pa) exhibits columnar structure (observed through cross-section SEM images of the film, figure not shown) with embedded spherical nodules on the surface. By increasing the pressure (to 30 and 40

Pa) dendritic, highly porous microstructure starts to appear with extremely irregular surface. The nodes in this case appear bigger, loosely packed, and non-spherical. Film-substrate adhesion is slightly poor than that reached at low Ar pressure. When using high pressure conditions (50 Pa), the film appears powder-like, with barely any adhesion to the substrate. The morphology of such a film is very similar to that of simulated films grown under ballistic deposition conditions. The collisional effects imposed by inert gas (Ar) at high pressure in the deposition chamber causes a cooling down of plume along with charges recombination and condensation of carbon clusters in the plume which are deposited on the substrate. In particular, by increasing the gas pressure, cluster-cluster collision may also occur that contributes to formation of bigger cluster which when assembled forms highly porous and irregular structure on the film surface. The visible consequence of such a process is the peculiar sequence of morphologies that develop in the growing film [10].

4.6.2 Catalytic activity measurements

Hydrogen generation yield was measured, as a function of time, by the hydrolysis of AB solution (0.025 M) at 298 K in presence of Co-B film catalyst supported on different carbon films deposited with various Ar pressures ranging from 20 to 50 Pa (see fig. 4.23). The inset of Fig. 4.23 shows the maximum H_2 generation rate R_{max} as a function of Ar gas pressure used to deposit the carbon films.

We want to note that the H_2 generation yield as function of time reported in fig. 4.23 for the unsupported Co-B film is not the same of fig. 4.21 because for the previous samples the weight of the deposited catalyst was about ten times lower. As the weight of Co-B film increases it takes less amount of time to reach the the maximum yield of hydrogen.

Co-B catalysts supported on C-film deposited at low Ar pressures (20 Pa) shows almost similar catalytic activity as un-supported Co-B film. We attribute this result to the non-porous structure of C-films. However, the catalytic activity increases for Co-B catalysts supported on C-films deposited at higher Ar pressures (30 and 40 Pa). R_{max} reached the maximum for C-film deposited at 40 Pa. As indicated by SEM images, the roughness and surface area of C-film increases with the deposition pressure. This trend is also followed by the H_2 generation rate for hydrolysis of AB as demonstrated in the inset of fig. 4.23.

4. CO-B NANOPARTICLES SYNTHESIZED BY PLD

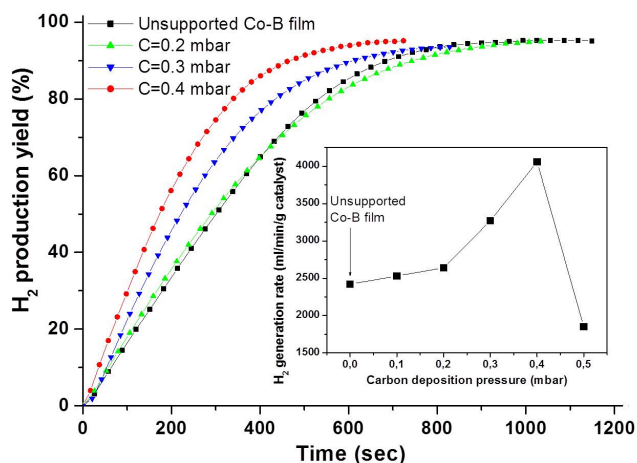


Figure 4.23: Hydrolysis of B (0.025 M) with Co-B film on carbon film Co-B supported C film deposited under different Ar gas pressure - Inset shows the R_{max} as a function of Ar gas pressure used to deposit the carbon films.

Thus, surface area and roughness of C-films play a vital role in the increment of catalytic activity for Co-B film catalyst by providing better dispersion and avoiding aggregation of Co-B nanoparticles. On the contrary, Co-B catalyst supported on C-film deposited at highest pressure of 50 Pa showed drastic decrease in the H_2 generation rate and was not able to complete the hydrolysis reaction of AB. The C-film deposited at this pressure had a very weak adhesion with the substrate and thus under vigorous stirring the film slowly detached from the substrate in the reactant solution during the AB hydrolysis reaction.

References

- [1] S.C. Amendola, S.L. Sharp-Goldman, M.S. Janjua, N.C. Spencer, M.T. Kelly, P.J. Petillo, and M. Binder. *Int. J. Hydrogen Energy*, 25:969, 2000. 33
- [2] T. Umegaki, J.M. Yan, X.B. Zhang, H. Shioyama, N. Kuriyama, and Q. Xu. *Int. J. Hydrogen Energy*, 34:2303, 2009. 33
- [3] F.H. Stephens, V. Pons, and R.T. Baker. *Dalton Trans.*, 25:2613, 2007. 33
- [4] Q. Xu and M. Chandra. *J. Alloys Compd.*, 446-447:729, 2007. 33
- [5] M. Chandra and Q. Xu. *J. Power Sources*, 156:190, 2006. 33
- [6] F. Durap, M. Zahmakiran, and S. Özkar. *Int. J. Hydrogen Energy*, 34:7223, 2009. 33
- [7] S.U. Jeong, R.K. Kim, E.A. Cho, H.J. Kim, S.W. Nam, I.H. Oh, S.A. Hong, and S.H. Kim. *J. Power Sources*, 144:129, 2005. 33
- [8] V. Johánek, M. Laurin, A.W. Grant, B. Kasemo, C.R. Henry, and J. Libuda. *Science*, 304:1639, 2004. 53
- [9] A. Miotello, G. De Marchi, G. Mattei, P. Mazzoldi, and C. Sada. *Phys. Rev. B*, 63:075409, 2001. 54
- [10] P.M. Ossi, C.E. Bottani, and A. Miotello. *Thin Solid Films*, 482:2, 2005. 59

REFERENCES

5

Cobalt oxide nanoparticles synthesized by PLD

5.1 Introduction

Textile dyes, releasing aromatic amines and potential carcinogens, are frequently found in trace quantities in industrial waste water. The increasing environmental concerns make it necessary to implement certain steps towards eliminating dyes from wastewater before discharging in the mainstreams. Advanced oxidation processes (AOP) involving active species like hydroxyl radical ($OH\bullet$) with very high oxidation potential resulted to be most efficient route for dye degradation [1]. This radical generation occurs by processes such as direct photolysis of H_2O_2 , photo-excitation of TiO_2 , and Photo-Fenton reaction in presence of H_2O_2 and metal cations [2]. However, the first two methods require high intensity UV light while the Photo-Fenton reaction proceeds by absorption of visible light hence showing significantly higher efficiency. Photo-Fenton reaction is very complex type of photocatalytic reaction which employs a mixture of H_2O_2 and ferrous ions (Fe^{2+} and Fe^{3+}) in acidic medium to generate the hydroxyl radicals in presence of light [3]. Due to the requirement of acidic medium with low pH (pH 3) the process results in large sludge residues. Other transition metal ions like Co^{2+} ions are found to be active even in neutral pH for generating hydroxyl radicals via Photo-Fenton process and this is a clear advantage over Fe^{2+} [4]. However, this kind of homogenous reaction produces additional impurity in the water by the dissolved metal ions (Fe^{2+} and Co^{2+}) thus avoiding its use on the commercial level. Hence the heterogeneous

5. COBALT OXIDE NANOPARTICLES SYNTHESIZED BY PLD

cobalt oxide catalyst has attracted great attention to generate hydroxyl radicals. The catalyst like Co_3O_4 has been considered for photodegradation of organic dyes in waste water treatment application because of its thermodynamic stability and desired catalyst properties [5, 6, 7]. Co_3O_4 nanorods prepared by complex pyrogenation method showed photocatalytic degradation of the three different dyes: reactive black, reactive turquoise, and reactive blue [8]. Small nanosized clusters of Co_3O_4 coated on PTFE (polytetrafluoroethylene) flexible coating are reported as novel and efficient supported photocatalysts in the fast discoloration of the azo-dye Orange II under simulated solar radiation in the presence of oxone [9]. Nano-structures of Co_3O_4 (nanoparticles, nanorods, nanowires, etc.) exhibit exceptional activity and selectivity in catalytic processes as compared to the corresponding bulk counterpart, especially because of their large surface-to-volume atomic ratio, size- and shape-dependent properties, and high concentration of under-coordinated active surface sites [10, 11]. The catalyst in form of NPs-assembled coating can be easily recovered and efficiently reused to serve as environmentally friendly green catalyst, as seen for Co-B catalyst. However, forming NPs with proper distribution and narrow size distribution on the coating surface has to be engineered carefully. Up to now, Co_3O_4 thin coatings have been synthesized by a variety of deposition techniques: electron-beam evaporation [12], electro-deposition [13], CVD [14], solgel route [15], atomic layer deposition [16], etc. None of the previously mentioned techniques were successful to form unique nanostructure on the surface of the coatings. Pulsed laser deposition (PLD) technique offers several advantages over other methods for both synthesis and tailoring of NPs properties on the coating surface by varying several PLD parameters. Furthermore, with PLD the desired stoichiometry of the material could be generally obtained. There are very few reports on the synthesis of Co_3O_4 synthesized using PLD in a temperature range of 300 – 600°C for different applications [17, 18, 19, 20, 21].

5.2 Synthesis of the samples

PLD was performed on Si substrate, glass substrate and Mo/C grids by using a KrF excimer laser at operating wavelength of 248 nm, pulse duration of 25 ns, and repetition rate of 20 Hz. Pure cobalt was used as the target for the laser ablation. The PLD chamber was evacuated up to a base pressure of 2×10^6 mbar prior to deposition that

was carried out by keeping a constant O_2 gas partial pressure in the chamber. O_2 gas was introduced in the chamber through mass flow controller and pumping was throttled in order to maintain the desired gas pressure. We performed several depositions varying the O_2 gas partial pressure P_{O_2} , the target to substrate distance d_{t-s} and substrate temperature T_{sub} .

More in detail we synthesized the following samples:

- $T_{sub} = 25, 100, 150, 200, 250^\circ C$, $F = 3J/cm^2$, $P_{O_2} = 4.5 \times 10^{-2}$ mbar, $d_{t-s} = 5.5$ cm
- $P_{O_2} = 4.5 \times 10^{-3}, 1.0 \times 10^{-2}, 4.5 \times 10^{-2}$ mbar, $F = 6J/cm^2$; $d_{t-s} = 5.5$ cm, $T_{sub} = 250^\circ C$,
- $d_{t-s} = 5.5, 8.5, 11.5$ cm, $F = 6J/cm^2$, $P_{O_2} = 4.5 \times 10^{-2}$ mbar, $T_{sub} = 250^\circ C$;
- *post* - O_2 : Cobalt deposited in vacuum at $P=2 \times 10^6$ mbar, $T_{sub} = 250^\circ C$, $F = 6J/cm^2$, $d_{t-s} = 5.5$ cm, after the deposition $P_{O_2} = 4.5 \times 10^{-2}$ mbar was introduced in the PLD chamber for 30 minutes;
- *post-annealing*: $F = 6J/cm^2$, $P_{O_2} = 4.5 \times 10^{-2}$ mbar, $T_{sub} = 25^\circ C$, $d_{t-s} = 5.5$ cm, after the deposition we increases $T_{sub} = 250^\circ C$.

Samples were analyzed by SEM, TEM, XRD, FT-IR and micro-Raman spectroscopy. The surface morphology of the samples was studied by scanning electron microscope (SEM-FEG, JSM 7001F, JEOL) equipped with energy-dispersive spectroscopy analysis (EDS, INCA PentaFETx3) to determine the composition of the samples. Transmission Electron Microscopy (TEM) analyses were performed with a field emission FEI TECNAI F20 SuperTwin FEG-(S)TEM microscope operating at 200 kV equipped with an EDAX energy-dispersive X-ray spectrometer (EDS). Bright-field TEM (BFTEM) images, high-resolution TEM (HR-TEM) images, Fast Fourier Transform (FFT) image and selected area electron diffraction (SAED) patterns have been recorded. Commercial Cu grids were used as substrate to prepare samples for TEM analysis. The structural characterization of the deposited samples was carried out by conventional X-ray diffraction (XRD), Cu $K\alpha$ radiation ($\lambda = 1.5414\text{\AA}$), in BraggBrentano ($\theta - 2\theta$) configuration. Raman spectra were recorded by using HORIBA Jobin Yvon LabRAM Aramis Raman spectrometer with diode pumped solid state laser at 532 nm. Bruker

5. COBALT OXIDE NANOPARTICLES SYNTHESIZED BY PLD

(Equinox 55) Fourier transform infrared spectroscopy (FT-IR) was used to perform FT-IR measurements.

5.3 Characterization of the films

5.3.1 Different substrate temperature

We varied the substrate temperature $T_{sub} = 25, 100, 150, 200, 250^{\circ}\text{C}$ while keeping the other parameters constant: $F = 3\text{J}/\text{cm}^2$, $P_{\text{O}_2} = 4.5 \times 10^{-2}$ mbar, $d_{t-s} = 5.5$ cm.

SEM analysis on the samples deposited at $T_{sub} = 25^{\circ}\text{C}$ and 250°C are shown in fig. 5.1.

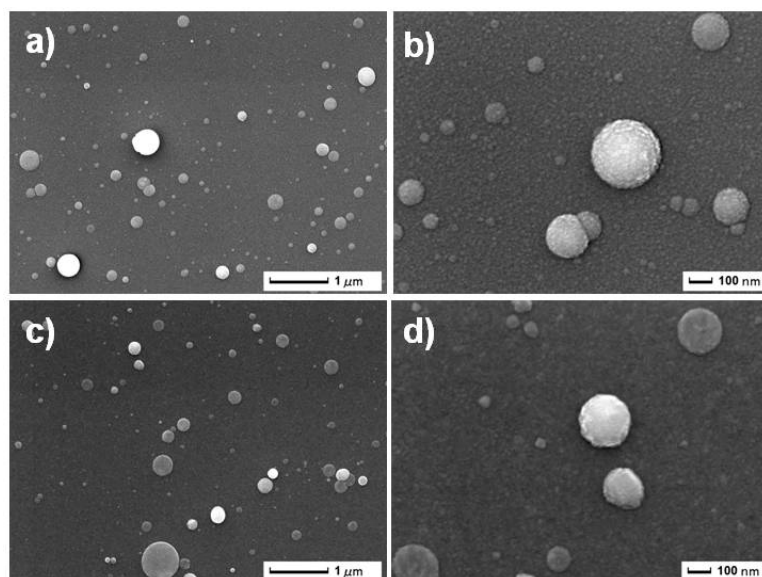


Figure 5.1: SEM micrographs of Co oxide films produced at different temperature - a,c) 25°C , b,d) 250°C

Fig. 5.2 shows the XRD spectra of samples prepared at different temperatures. Co_3O_4 (311) and (200) peaks are barely detected at $2\theta = 31.2^{\circ}$ and 36.5° , respectively, for samples prepared at 25°C , and 100°C , indicating prevailing NPs in amorphous phase. In addition to these peaks, with higher intensity, an extra peak at $2\theta = 19.0^{\circ}$ attributed to (111) plane is also detected for the sample prepared at 150°C indicating increase of crystalline phase of NPs. The diffraction peaks in the NPs deposited at 200°C and 250°C are clearly observed at $2\theta = 19.0^{\circ}, 31.2^{\circ}, 36.5^{\circ}, 38.4^{\circ}$ and 59.0° which

5.3 Characterization of the films

are attributed to the spinel type cubic structure of Co_3O_4 with Fd3m space group [22]. These diffraction peaks correspond to the reflections (111), (200), (311), (222) and (511) as from the JCPDS data file 009-0418. The diffraction peak appearing at $2\theta = 69^\circ$ is attributed to silicon substrate. No diffraction peaks are observed, in the XRD spectra, to be attributed to metallic Co or to other cobalt oxides.

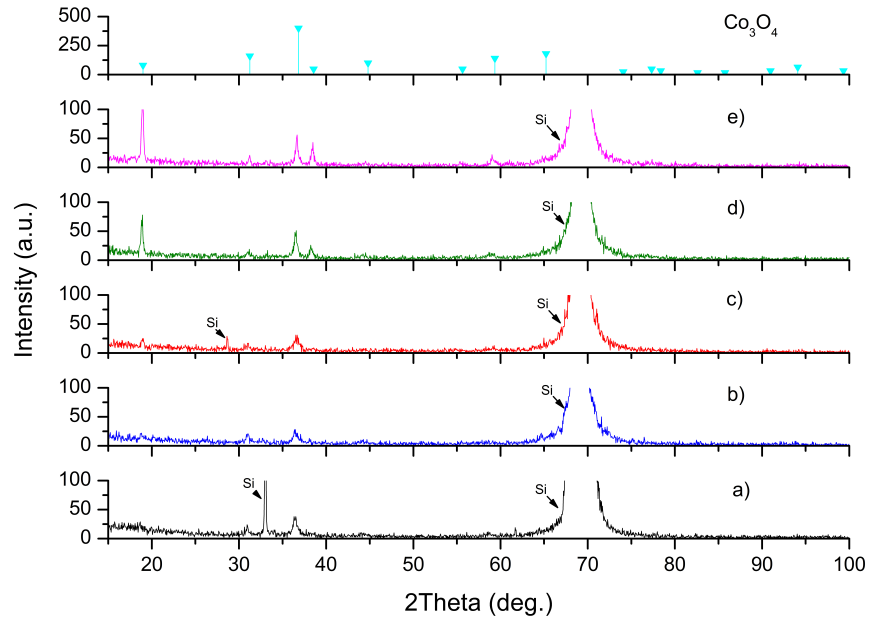


Figure 5.2: X-ray diffraction pattern of Co oxide films NPs synthesized by PLD at different temperatures - a) 25° C, b) 100°C, c) 150°C, d)200°C, and e) 250°C

Fig. 5.3 shows Raman spectra for films deposited at various temperatures. The spectrum has been taken in the range $200\text{--}1200\text{ cm}^{-1}$, but here we display only the interesting region $370\text{--}800\text{ cm}^{-1}$. The Raman spectrum of samples prepared at 250°C , clearly displays four bands in that range. The signals located at approximately 485 , 625 , and 696 cm^{-1} correspond to the E_g , F_{2g2} , and A_{1g} modes respectively of the crystalline Co_3O_4 phase [23]. The peak located at 529 cm^{-1} has a FWHM of about 17 cm^{-1} , and can be formed by the contribution of both F_{1g2} modes of the crystalline Co_3O_4 phase (at 527 cm^{-1}) and of bulk crystalline (expected at 523 cm^{-1}). In sample deposited at 200°C the signal at 626 cm^{-1} is weak, while second the peak at about 525 cm^{-1} shows more distinctly the presence of two contributions respectively at 520 and

5. COBALT OXIDE NANOPARTICLES SYNTHESIZED BY PLD

527 cm^{-1} . For the sample prepared 150°C the peak at 626 cm^{-1} is almost completely disappeared while in the second peak the signal of Si at 520 cm^{-1} predominates the signal at 527 cm^{-1} coming from the F_{1g2} modes of the crystalline Co_3O_4 phase. At 100°C we can see only three distinct peak: one at 485 cm^{-1} and another at 694 cm^{-1} both related to the crystalline Co_3O_4 phase, and the third at 520 cm^{-1} due to Si, with a small protrusion at 526 cm^{-1} assignable to Co_3O_4 phase. Finally the films prepared at RT show the same signals of the 100°C , even if the contribution of Si is lower.

5.3.2 Different oxygen partial pressure

We wanted to study the dependence of morphology and composition of our films on O_2 partial pressure. We prepared samples at three different P_{O_2} , namely $P_{\text{O}_2} = 4.5 \times 10^{-3}$, 1.0×10^{-2} , 4.5×10^{-2} mbar. Samples to be analyzed by SEM, FTIR and micro-Raman were deposited on Si substrate using 20000 pulses, while samples to be analyzed by TEM were deposited on Mo/C grids using 1000 pulses.

In fig. 5.4 the images of the samples surface taken by SEM are showed.

The density of the big droplets (size of the order of $\mu\text{ m}$) decreases slightly by increasing pressure, while the density of the small droplets (hundred of nm) increases little

The background structure consists of small NPs (tens of nm) for medium and high pressure, while it appears continuous at low pressure.

Fig. 5.3 shows Raman spectra for films deposited at different P_{O_2} . The spectrum of sample obtained at the lowest pressure presents three peaks at 489, 523 and 699 cm^{-1} . A small signal is also detectable at 629 cm^{-1} . The spectrum of the film prepared at $P_{\text{O}_2} = 1.0 \times 10^{-2}$ shows three peaks at 485, 529 and 695 cm^{-1} , and a broad and weak peak at 626 cm^{-1} . The spectrum of the samples at $P_{\text{O}_2} = 4.5 \times 10^{-2}$ mbar displays again three peaks at 485, 529 and 696 cm^{-1} , and a more defined peak at 626 cm^{-1} .

FTIR analysis of samples deposited at different P_{O_2} are shown in fig. 5.20 and do not reveal important differences among the films. The spectrum exhibit three peaks related to the Co_3O_4 phase: 389, 561 and 660 cm^{-1} . The other broad peak appearing at around 610 cm^{-1} and the signal at 515 cm^{-1} , emerging from the tail of the second peak of Co_3O_4 , are both related to the substrate of Si.

TEM analysis were performed on samples deposited at $P_{\text{O}_2} = 4.5 \times 10^{-2}$ and 4.5×10^{-3} mbar.

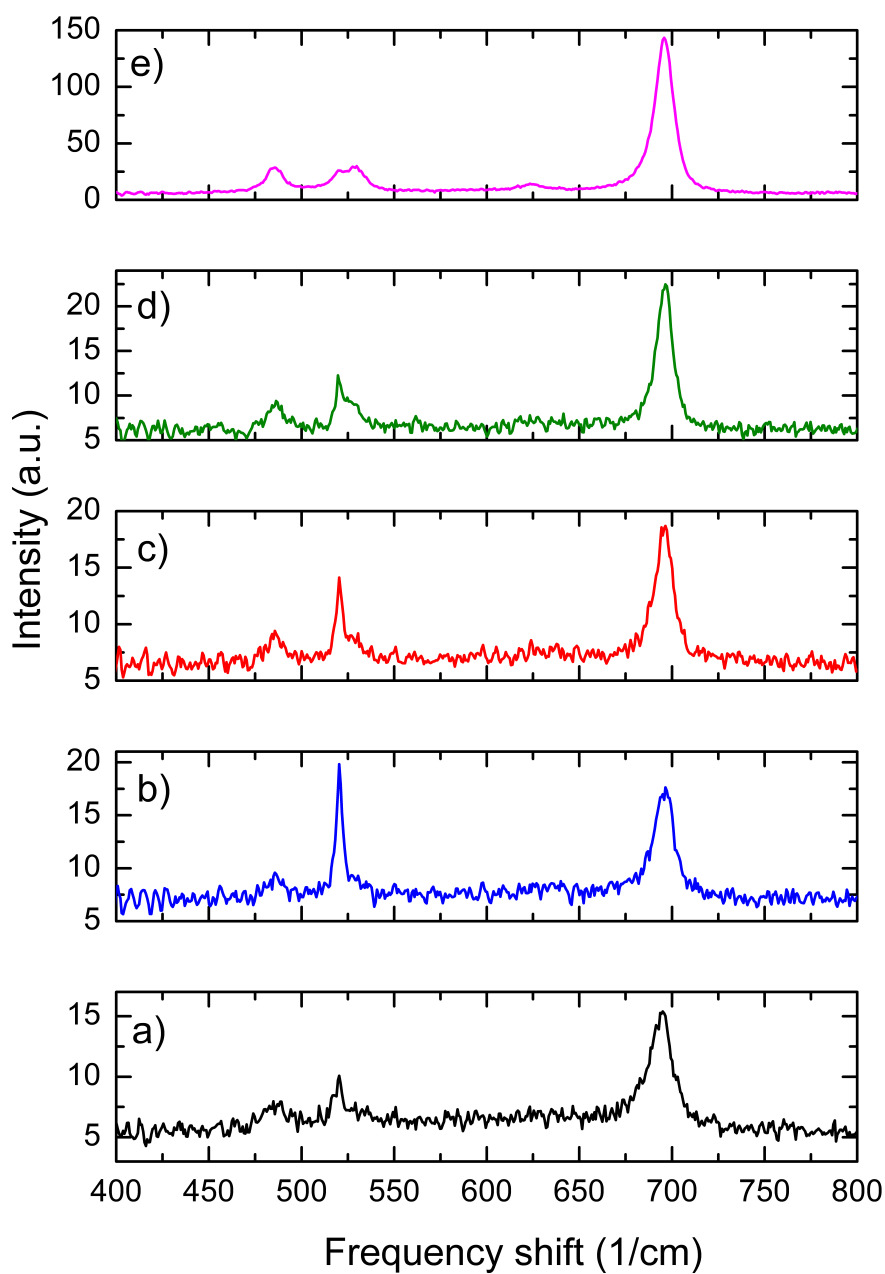


Figure 5.3: Raman spectra of Co oxide films NPs synthesized by PLD at different temperatures - a) 25°C, b) 100°C, c) 150°C, d) 200°C, and e) 250°C

5. COBALT OXIDE NANOPARTICLES SYNTHESIZED BY PLD

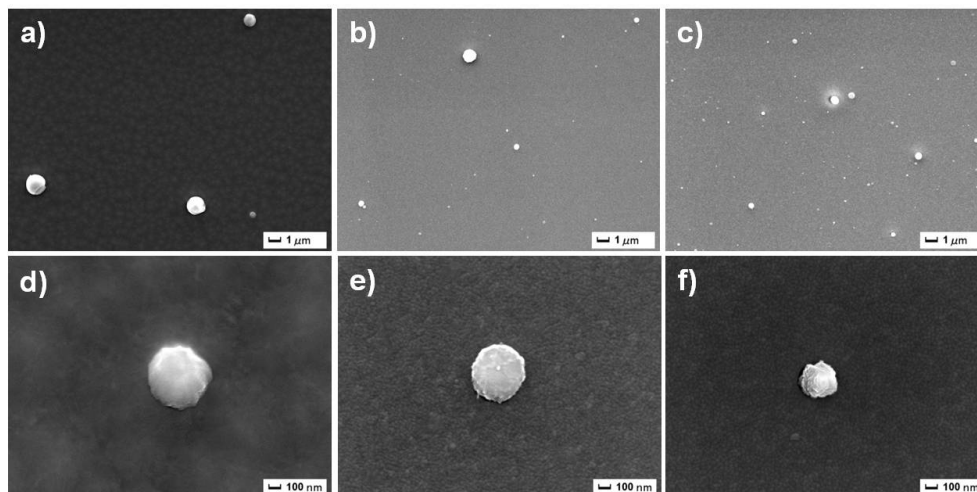


Figure 5.4: SEM micrographs of Co oxide films produced at different P_{O_2} - a,d) 4.5×10^{-3} mbar, b,e) 1.0×10^{-2} mbar, c,f) 4.5×10^{-2} mbar

In sample deposited at $P_{O_2} = 4.5 \times 10^{-2}$ mbar Bright-Field-TEM (BF-TEM) revealed the presence of crystalline NPs having different sizes and shapes over a continuous film deposited on the carbon (see fig. 5.7).

Big NPs, of sizes varying from 50 to 400nm, are surrounded by a shell with thickness of about 15nm that sometimes is not complete (see fig. 5.8).

High-Resolution-TEM (HR-TEM) shows that small NPs are uniformly dispersed on the carbon film and have a mean diameter $\langle D \rangle = (5.9 \pm 1.6nm)$ (see fig. 5.9).

Fast Fourier Transform (FFT) analysis of the HR images confirmed that NPs are crystalline and are formed by Co-oxides (CoO and/or Co_3O_4 -phase). Big NPs are poly-crystalline and in the inner part are formed by Co-hcp and Co-oxide phases, while presence of Co_3O_4 was detected in the surrounding shell (see fig. 5.10).

In the Scanning-TEM (STEM) images the big NP is surrounded by a shell constituted by lighter elements (the contrast is lower than for the inner part) while the carbon film appears uniformly covered by smaller NPs (see fig. 5.11).

EDX compositional spectra were acquired focusing the electron beam on the films covered by small NPs and on a single big NP. Co/O ratio is respectively: (0.6 ± 0.1) and (10 ± 2) .

For $P_{O_2} = 4.5 \times 10^{-3}$ mbar BF-TEM shows the presence of big NPs having a diameter bigger than 100 nm (dimension from 100 to 300 nm) that could be divided

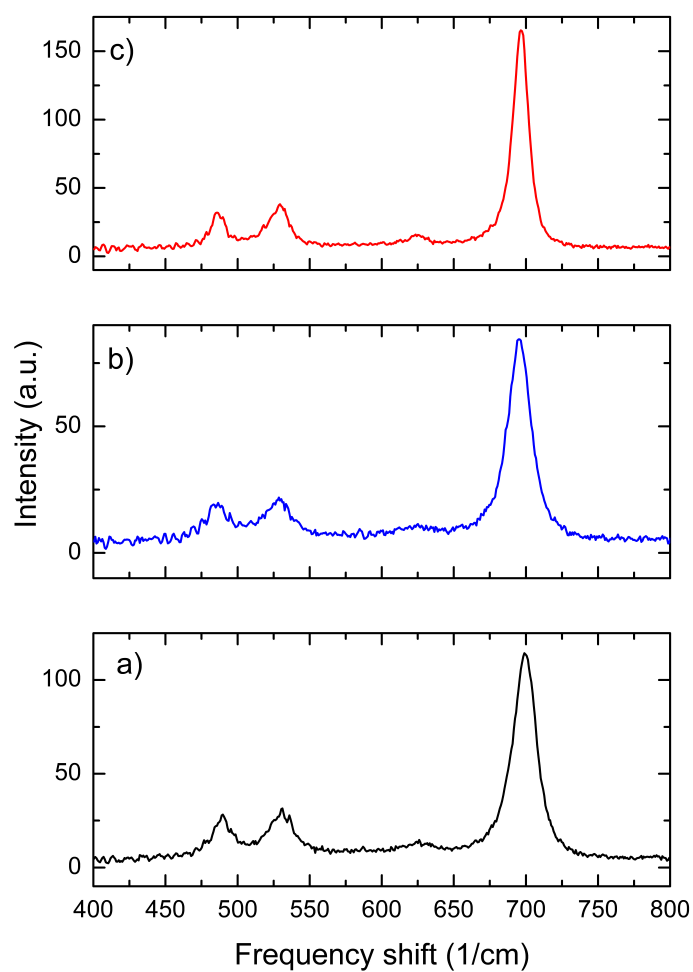


Figure 5.5: Raman spectra of Co oxide films NPs synthesized by PLD at different P_{O_2} - a) 4.5×10^{-3} mbar, b) 1.0×10^{-2} mbar, c) 4.5×10^{-2} mbar

5. COBALT OXIDE NANOPARTICLES SYNTHESIZED BY PLD

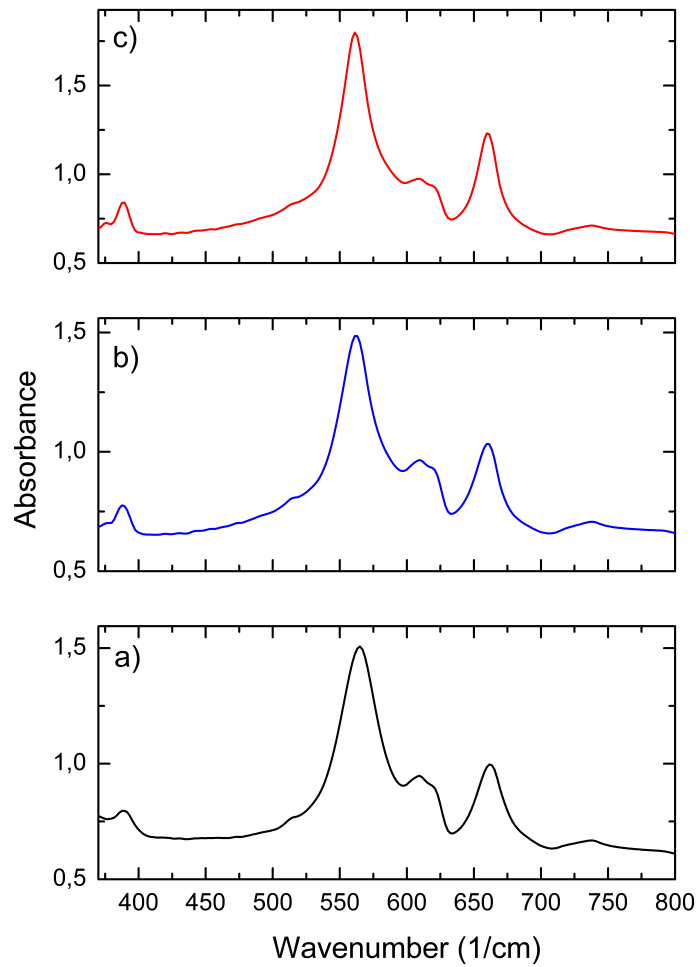


Figure 5.6: FT-IR absorption spectra of Co oxide films NPs synthesized by PLD at different P_{O_2} - a) 4.5×10^{-3} mbar, b) 1.0×10^{-2} mbar, c) 4.5×10^{-2} mbar

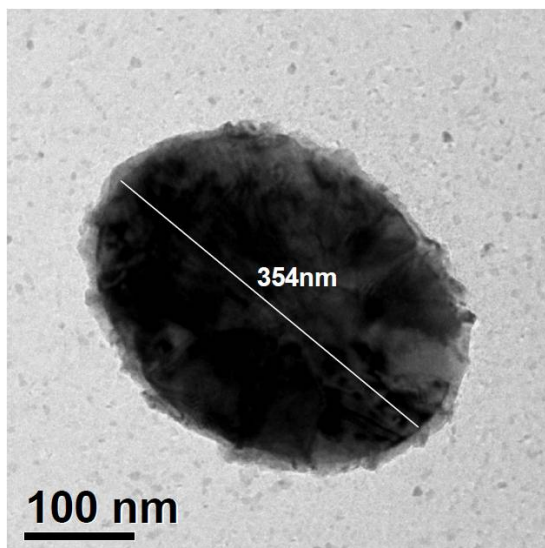


Figure 5.7: BF-TEM images of a core/shell NP - sample prepared at $P_{O_2} = 4.5 \times 10^{-2}$, $F = 6 J/cm^2$; $d_{t-s} = 5.5$ cm, $T_{sub} = 250^\circ C$

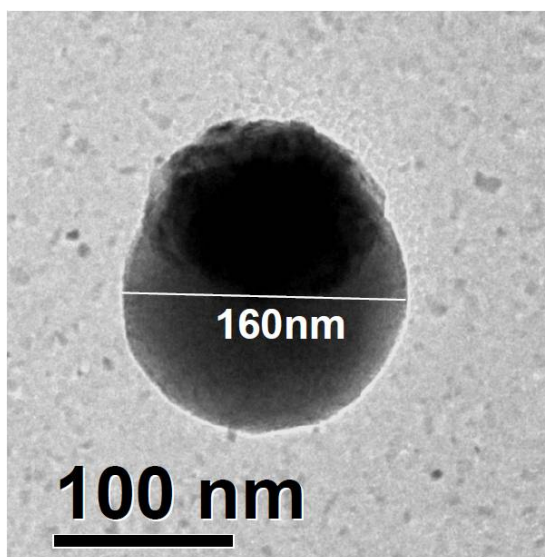


Figure 5.8: BF-TEM images of a core/shell NP with an incomplete shell - sample prepared at $P_{O_2} = 4.5 \times 10^{-2}$ mbar, $F = 6 J/cm^2$; $d_{t-s} = 5.5$ cm, $T_{sub} = 250^\circ C$

5. COBALT OXIDE NANOPARTICLES SYNTHESIZED BY PLD

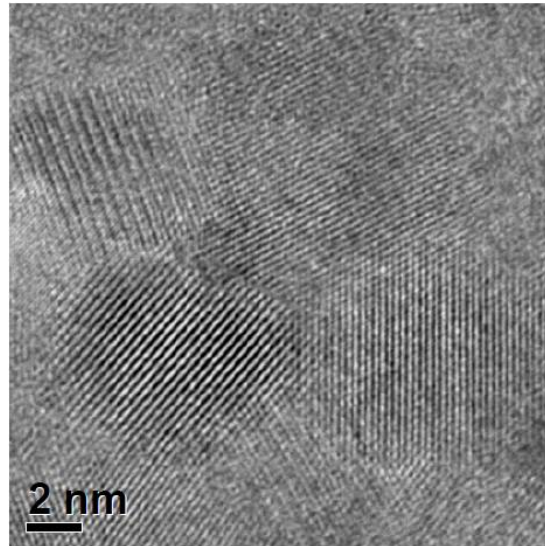


Figure 5.9: HR-TEM images small NPs - sample prepared at $P_{O_2} = 4.5 \times 10^{-2}$ mbar, $F = 6 J/cm^2$; $d_{t-s} = 5.5$ cm, $T_{sub} = 250^\circ C$

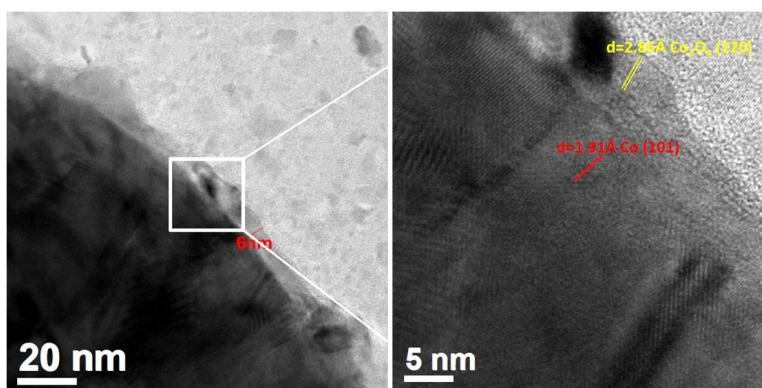


Figure 5.10: HR-TEM images of the shell surrounding big NPs - sample prepared at $P_{O_2} = 4.5 \times 10^{-2}$ mbar, $F = 6 J/cm^2$; $d_{t-s} = 5.5$ cm, $T_{sub} = 250^\circ C$

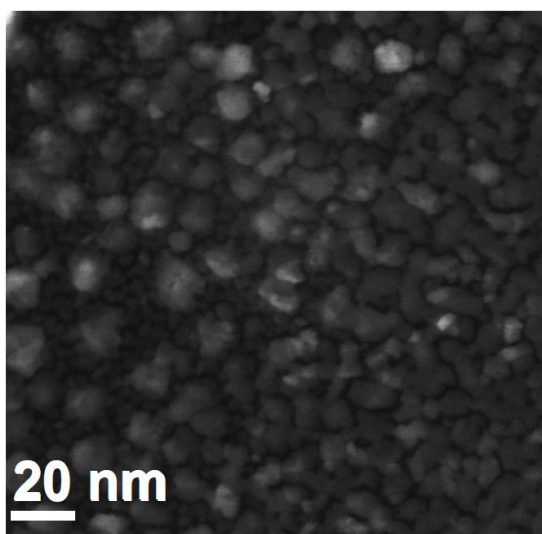


Figure 5.11: STEM images of small NPs dispersed on the carbon support - sample prepared at $P_{O_2} = 4.5 \times 10^{-2}$ mbar, $F = 6 J/cm^2$; $d_{t-s} = 5.5$ cm, $T_{sub} = 250^\circ C$

into two types:

- Poly-crystalline NPs surrounded by a not complete shell with a thickness of about ($5 \div 10 nm$) (see fig. 5.12a)
- NPs that seems to be amorphous (see fig. 5.12b))

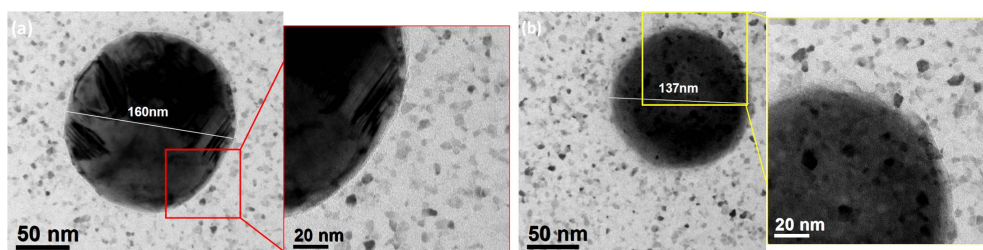


Figure 5.12: BF-TEM images of two kind of big NPs: a) core/shell NPs, b) amorphous cobalt oxide NPs - sample prepared at $P_{O_2} = 4.5 \times 10^{-3}$ mbar, $F = 6 J/cm^2$; $d_{t-s} = 5.5$ cm, $T_{sub} = 250^\circ C$

There is again a continuous film deposited on the carbon support, and crystalline small NPs with $\langle D \rangle = (4.8 \pm 1.1)$ nm are uniformly dispersed on the carbon film. FFT analysis of the HR images of the small NPs showed that NPs are poly-crystalline and are formed by CoO-phase. Big NPs are poly-crystalline and in the inner part are

5. COBALT OXIDE NANOPARTICLES SYNTHESIZED BY PLD

formed by Co-hcp and Co-oxide phases, while the surrounding shell is formed by Co-oxide (CoO and/or Co_3O_4 -phase). STEM confirms again that big NP is surrounded by a not-complete shell constituted by lighter elements. EDX compositional spectra were acquired by focusing the electron beam on small NPs and big NP as illustrated in fig. 5.13. Co/O ratio is (0.6 ± 0.1) for small NPs and (7 ± 1) for big NP.

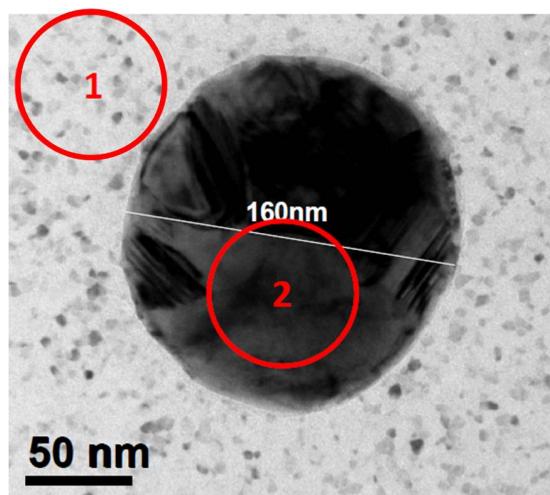


Figure 5.13: BF-TEM images with region analyzed by EDX evidenced : 1) small NPs, 2) big - sample prepared at $P_{O_2} = 4.5 \times 10^{-3}$, $F = 6 J/cm^2$; $d_{t-s} = 5.5$ cm, $T_{sub} = 250^\circ C$

5.3.3 Different target-to-substrate distance

In fig. 5.14 the SEM images of the samples deposited at different d_{t-s} are presented. The density of the big NPs decreases with distance.

Raman spectrum for samples prepared at different d_{t-s} (see fig. 5.15) shows no evident differences. Four signals appear in all spectra at 485, 529, 626 and 696 cm^{-1} , indicating the presence of Co_3O_4 phase.

FTIR analysis on samples deposited at different d_{t-s} (fig. 5.20) are similar. All spectra exhibit three peaks related at the Co_3O_4 phase (389, 561 and 660 cm^{-1}) and one broad peak appearing at around 610 cm^{-1} assigned to Si substrate. The signal at about 515 cm^{-1} , emerging from the tail of the second peak of Co_3O_4 and related to the substrate of Si, appears more clearly in the films deposited at higher distances. The width of the peak at 660 cm^{-1} decreases by increasing d_{t-s} .

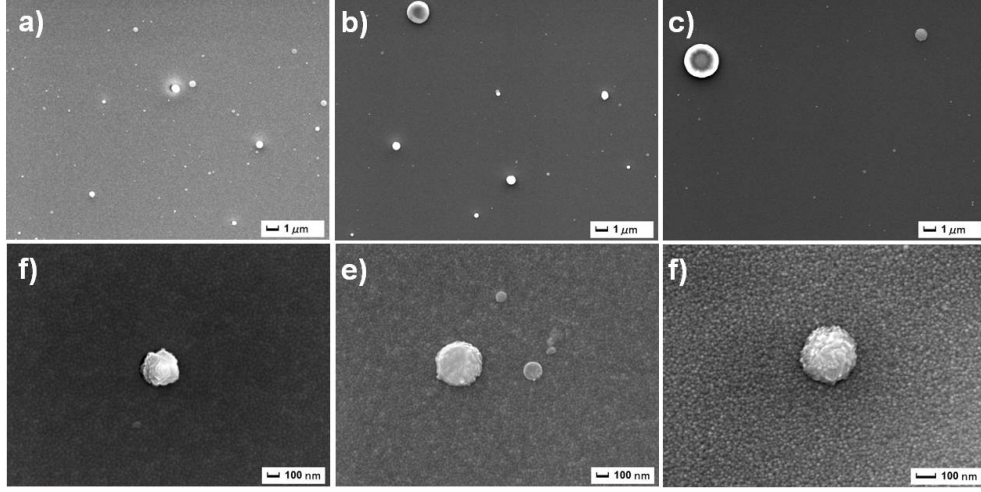


Figure 5.14: SEM micrographs of Co oxide films produced at different d_{t-s} - a,d) 5.5 cm, b,e) 8.5 cm, c,f)11.5 cm

Samples deposited at $d_{t-s}=8.5$ cm were analyzed at TEM. BF-TEM revealed the presence of both crystalline nano-particles (NPs) having different sizes and of a continuous film deposited on the carbon support. However no NPs with a diameter bigger than 100 nm (size varies from 10 to 100nm) were found and the continuous film is thinner with respect to $d_{t-s}=5.5$ cm. HRTEM confirms that small NPs (see fig. 5.17) are uniformly dispersed on the carbon film and have a mean diameter $\langle D \rangle = (4.4 \pm 0.9$ nm). FFT analysis of the HR images has confirmed that NPs are poly-crystalline and are formed by Co-oxide, the most probable phase seems CoO-phase.

FFT analysis of the HR images of the big NPs has shown that they are poly-crystalline and are formed by cobalt oxide phases. EDX compositional spectra were acquired by focusing the electron beam on the background of small NPs and on the single big NP. Oxygen was found both in the small and in the big NPs and the Co/O ratios are respectively: (0.5 ± 0.1) and (0.9 ± 0.2) . The quantification of the oxygen, especially in the big NP, could be underestimated due to X-Ray signal absorption effects.

5.3.4 Different post-deposition treatment

We named *post - O₂* the sample obtained by depositing Cobalt in vacuum at $P=2 \times 10^6$ mbar, $T_{sub} = 250^\circ\text{C}$, $F = 6\text{J}/\text{cm}^2$, $d_{t-s} = 5.5$ cm, and then introducing $P_{O_2} = 4.5 \times$

5. COBALT OXIDE NANOPARTICLES SYNTHESIZED BY PLD

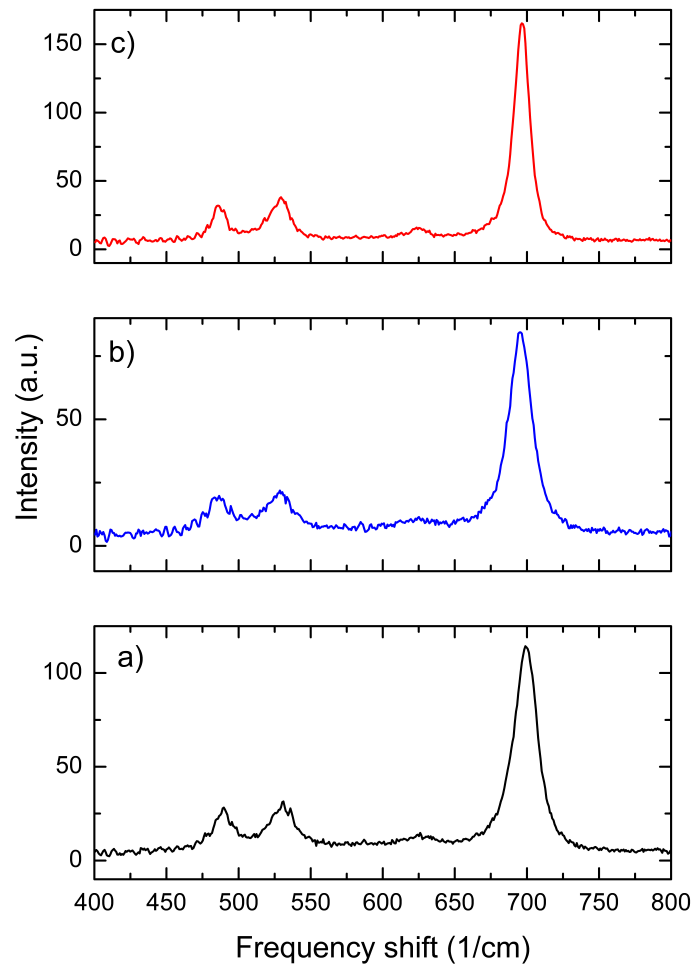


Figure 5.15: Raman spectra of Co oxide films NPs synthesized by PLD at different d_{t-s} - a) 5.5 cm, b) 8.5 cm, c) 11.5 cm

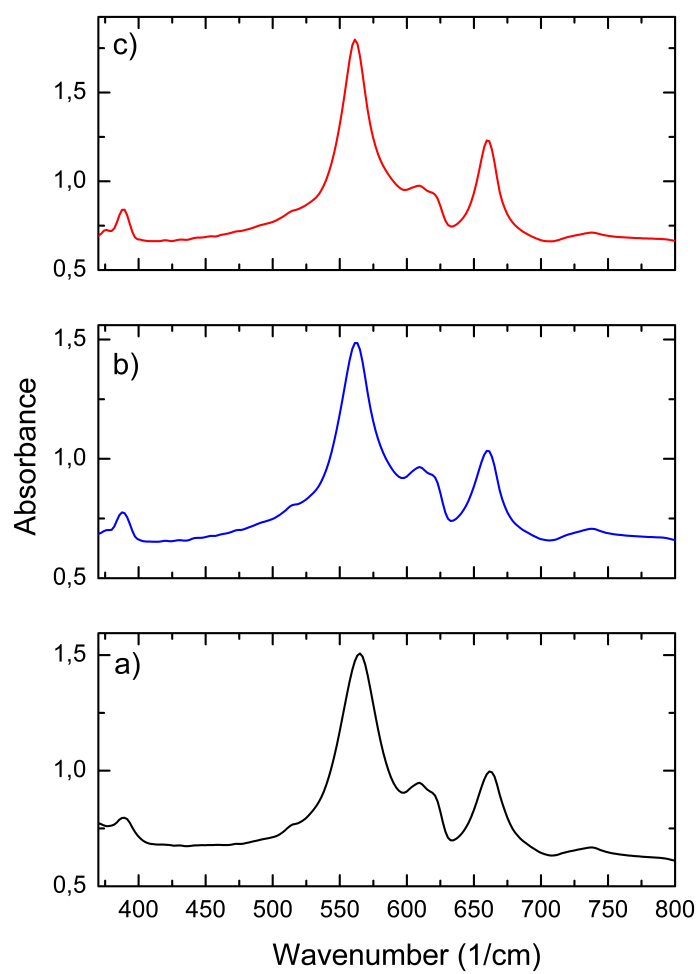


Figure 5.16: FT-IR absorption spectra of Co oxide films NPs synthesized by PLD at different d_{t-s} - a) 5.5 cm, b) 8.5 cm, c) 11.5 cm

5. COBALT OXIDE NANOPARTICLES SYNTHESIZED BY PLD

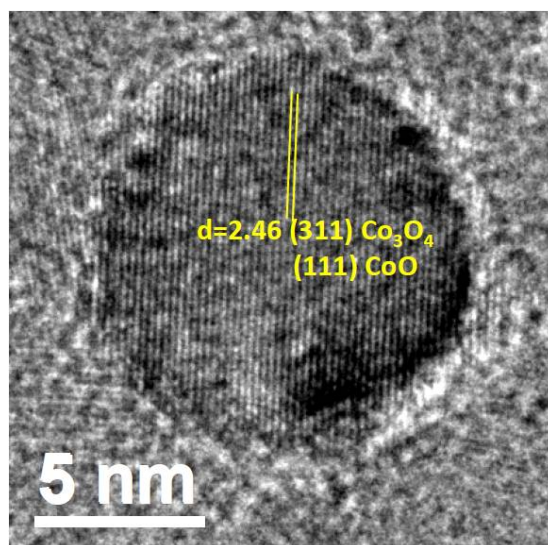


Figure 5.17: HRTEM images of small NPs with reported experimental $d(\text{\AA})$ - sample prepared at $P_{O_2} = 4.5 \times 10^{-2}$ mbar, $F = 6J/cm^2$; $d_{t-s} = 8.5$ cm, $T_{sub} = 250^\circ C$

10^{-2} mbar in the PLD chamber for 30 minutes after the deposition. Then we named *post-annealing* the sample obtained by depositing Cobalt using $F = 6J/cm^2$, $P_{O_2} = 4.5 \times 10^{-2}$ mbar, $T_{sub} = 25^\circ C$, $d_{t-s} = 5.5$ cm, and then increasing $T_{sub} = 250^\circ C$ after the deposition.

In figure 5.18 the SEM images of the *post-O₂* and *post-annealing* are reported, together with the sample deposited in the usual condition ($F = 6J/cm^2$, $P_{O_2} = 4.5 \times 10^{-2}$ mbar, $T_{sub} = 250^\circ C$, $d_{t-s} = 5.5$ cm).

The Raman spectra of *post - O₂* sample (fig. 5.19b) shows two weak peaks, at 482 and 523 cm^{-1} and a well distinguishable peak at 693 cm^{-1} . The Raman spectra of *post-annealed* samples (fig. 5.19c) exhibit the usual four peaks at 485, 529, 623 and 693 cm^{-1} . However only for this sample the relative intensity of the first peak is higher than the intensity of the second peak.

In FTIR spectrum of *post-O₂* sample (fig. ??b) no peak is detected. FTIR analysis on *post-annealed* films (fig. ??c) displays four peaks: 385, 560, 613 and 660 cm^{-1} . The third peak is, as usual, attributed to the Si substrate. The others three peaks are related to the Co_3O_4 phase, with the first one shifted downward of 4 cm^{-1} .

TEM analysis were carried out on *post - O₂* sample. BF-TEM reveals the presence of crystalline NPs having different sizes and shapes (see fig. 5.21)

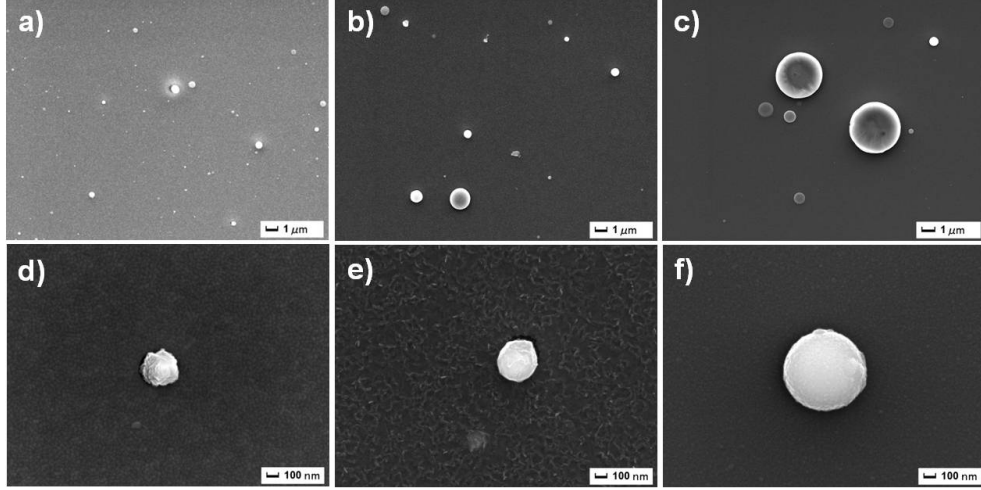


Figure 5.18: SEM micrographs of Co oxide films produced at different conditions - a,d) standard, b,e) post oxygen, c,f) post annealing

Small NPs are uniformly dispersed on the carbon film and have $\langle D \rangle = (5.0 \pm 1.1)$ nm. FFT analysis of the HR images confirmed that NPs are poly-crystalline and are formed by Co oxides (CoO and Co_3O_4). Big NPs, with dimension varying from 50 to 100 nm, are poly-crystalline and are divided in:

- Core-shell NPs with an inner region of Co-hcp phase and a surrounding shell of Co oxides with thickness of $15 \div 30 \text{ nm}$ (fig. 5.22).
- few NPs completely formed by Co-oxide phase.

EDX compositional spectra were acquired as usual giving a Co/O ratio of (0.9 ± 0.2) for the small NPs and (2.1 ± 0.6) for big NP.

5.4 Discussion on sample characterization

First we want to focus our attention on one result obtained by SEM analysis, that can help to understand the dynamic of the NPs formation.

A SEM image of NPs deposited at $F = 6 \text{ J/cm}^2$, $P_{\text{O}_2} = 4.5 \times 10^{-2}$ mbar, $T_{\text{sub}} = 250^\circ\text{C}$, $d_{t-s} = 5.5$ cm is reported in fig. 5.23. It is clear that in this condition the droplets are molten before hitting the substrate where the NPs rapidly cool.

The size of the small NPs is almost the same for the four samples analyzed by TEM. This means that they are not formed from aggregation of atoms in the plume,

5. COBALT OXIDE NANOPARTICLES SYNTHESIZED BY PLD

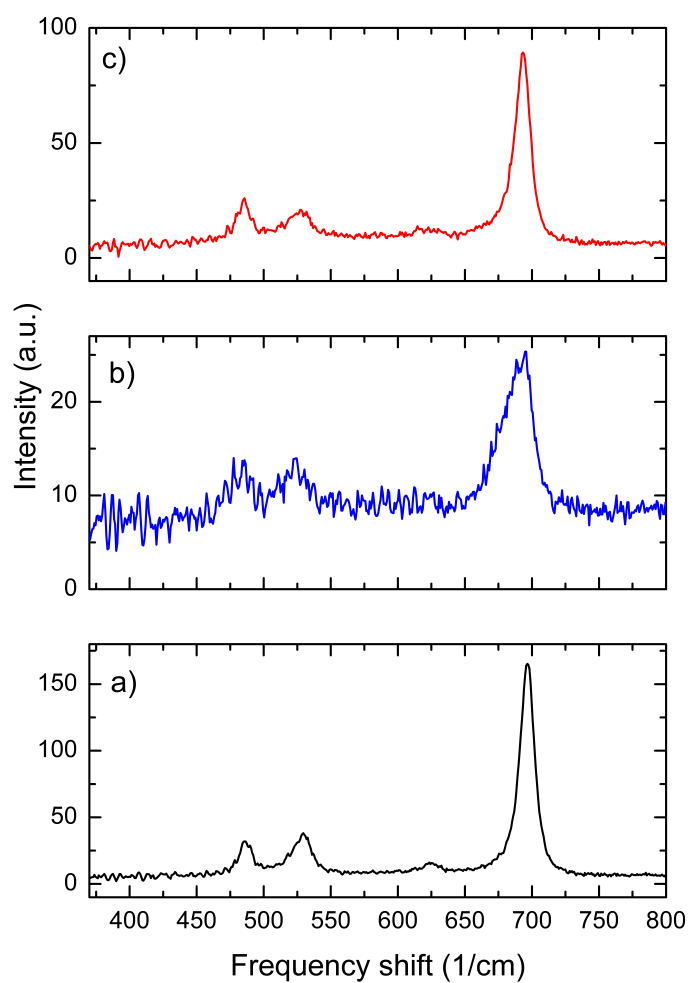


Figure 5.19: Raman spectra of Co oxide films NPs synthesized by PLD at different treatment - a) standard, b) post oxygen, c) post annealing

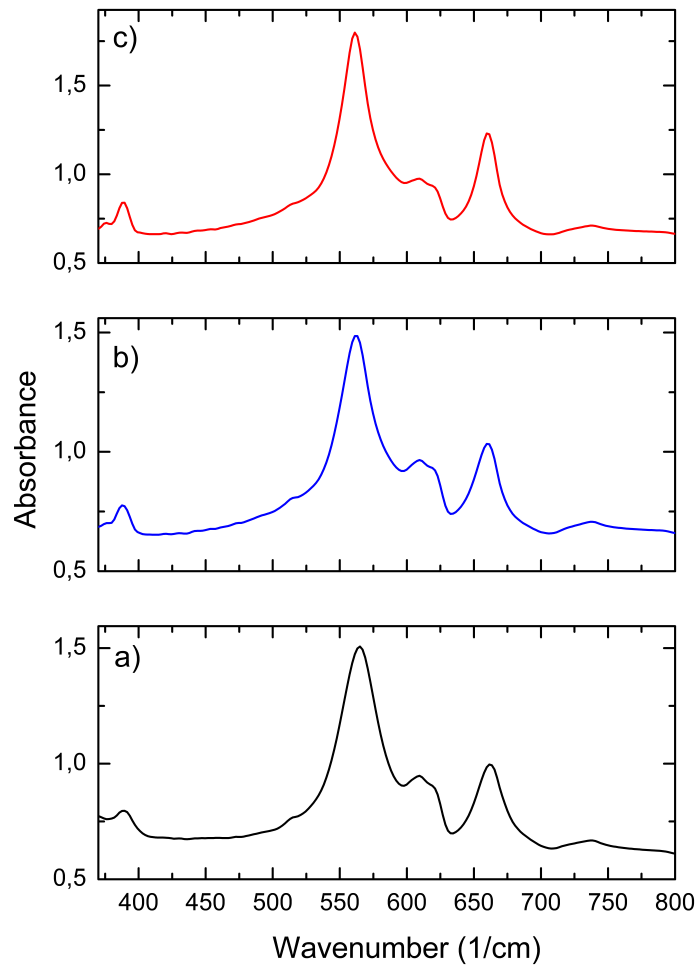


Figure 5.20: FT-IR absorption spectra of Co oxide films NPs synthesized by PLD at different conditions - a) standard, b) post oxygen, c) post annealing

5. COBALT OXIDE NANOPARTICLES SYNTHESIZED BY PLD

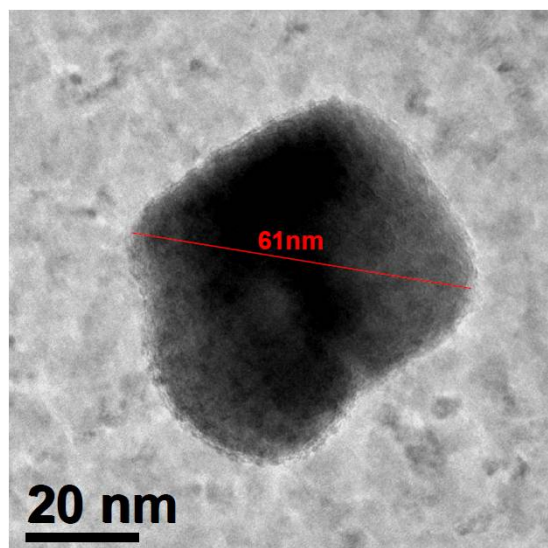


Figure 5.21: BF-TEM images of a big NPs with not spherical shape - *post* - O_2 sample

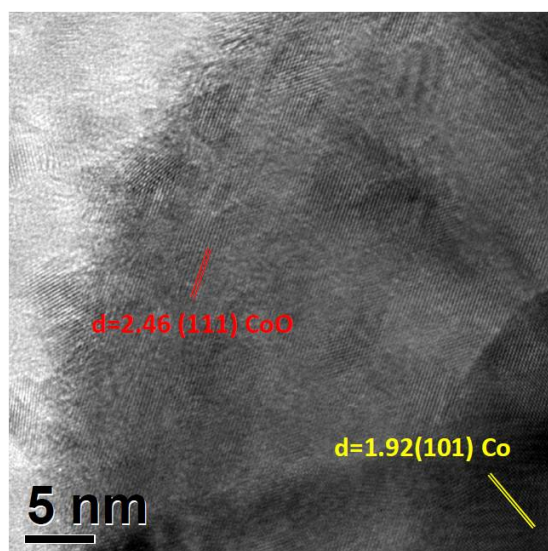


Figure 5.22: HR-TEM images of a core/shell (Co-hcp/Co oxide) NPs - *post* - O_2 sample

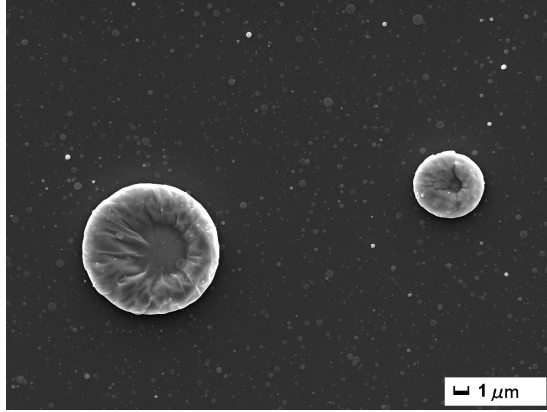


Figure 5.23: SEM micrographs magnification of cobalt oxide NPs - deposited at $F = 6 J/cm^2$, $P_{O_2} = 4.5 \times 10^{-2}$ mbar, $T_{sub} = 250^\circ C$, $d_{t-s} = 5.5$ cm

otherwise the different deposition parameters would have affected the dimension of the NPs. Droplets of different size, from few nm to hundred of nm are directly ejected from the target due to phase explosion phenomena.

Moreover the continuous films over the C support observed in all the samples analyzed by TEM come from the atom ejected because of normal vaporization.

5.4.1 Different substrate temperatures

SEM images show that the small NPs have a narrow size distribution and are densely arranged on the substrate surface. The density of the bigger NPs (size of the order of 100 nm) is higher for $T = 25^\circ C$ and $T = 250^\circ C$, while it decreases for intermediate temperature.

The complete crystallization is seen for the sample prepared at $250^\circ C$ where we see presence of all the vibration modes of Co_3O_4 by Raman analysis. This is also in good agreement with XRD results.

All the above results prove the clear role of the substrate temperature in the observed increase of NP crystallinity by favoring adatom diffusion and coalescence, and allowing NP to form more ordered structure.

5.4.2 Different oxygen partial pressure

SEM images show that the density of big NPs decreases while increasing P_{O_2} . For the NPs reaching the substrate the increase in the ambient-gas pressure results in a reduced

5. COBALT OXIDE NANOPARTICLES SYNTHESIZED BY PLD

sticking coefficient of the droplets on the film surface due to their lower kinetic energy [24].

Big NPs for high P_{O_2} , as seen by TEM, have a core-shell structure (Co-hcp mixed Co oxides / Co_3O_4 phase). Instead for $P_{O_2} = 4.5 \times 10^{-3}$ mbar, we found two kind of NPs: core/shell (Co-hcp mixed Co oxides/Co oxides) and amorphous cobalt oxide.

The droplets ejected from the target are composed by cobalt and have an high temperature (remember that to have phase explosion the target surface must reach a temperature near the critical point of the material). During the flight the NPs collide with the atoms of the plume and of the background gas, losing their initial kinetic energy. In the plume the NPs surface start to oxidize and the oxygen diffuse into the core of the NPs during the flight. We suppose that the NPs reach the substrate with a mixed Co-CoO composition, but as shown both by SEM (fig. 5.23) and TEM (fig. 5.7) they are still molten. So before the complete solidification on the substrate a surface oxidation may take place leading to the formation of a partial Co_3O_4 shell. For low P_{O_2} the shell is not Co_3O_4 phase but a mixed CoO- and Co_3O_4 phase because the oxygen content in the chamber is too low to have a complete oxidation of the CoO-phase into Co_3O_4 phase. Furthermore the thickness of the shell is higher for higher pressure of O_2 . This also can be due to the greater amount of O_2 in the chamber.

In addition small NPs are only in the CoO phase for low P_{O_2} , while Co_3O_4 phase appears for small NPs at high pressure. This also can be explained by the lower content of O_2 in the chamber at $P_{O_2} = 4.5 \times 10^{-3}$ mbar, that does not allow the complete oxidation of small NPs. Moreover the small NPs should reach the substrate already in the solid state (so with a low temperature) due to their small size. So the T_{sub} alone can not be enough to sustain Co_3O_4 formation.

Raman, FTIR an XRD analysis do not reveal any signal coming from CoO even for the sample prepared at low pressure. We have to remember that the samples analyzed by these techniques are deposited using an high number of pulses (20000) than for samples prepared for TEM analysis (1000 pulses). An higher number of pulses implies longer deposition time: for a pulse repetition rate equal to 20 Hz, the time required to complete the deposition is 50 seconds for 1000 pulses, while the deposition takes 15 minutes for 20000 pulses. During the deposition the NPs already deposited on the substrate remain in an enriched O_2 atmosphere on the heated substrate. So the presence of CoO may be suppressed because of a longer interaction time between the

5.4 Discussion on sample characterization

deposited NPs and the oxygen atmosphere at $T_{sub} = 250^\circ$. It is possible that the small CoO NPs was transformed into Co_3O_4 . Phenomena of coalescence, and so of diffusion of atoms, on the substrate are also indicated by the irregular and elongate shape of some NPs (25), such in fig. 5.21 and 5.7.

Raman spectrum show the absence of the peak at 629 cm^{-1} for $P_{O_2} = 4.5 \times 10^{-3}$ mbar. Furthermore in this sample all the other peaks shifted toward higher wavenumbers.

The shift of Raman peaks to higher wavenumbers can have several causes. For nanocrystals smaller than 30 nm, the size dependence of Raman spectra (downshift and broadening of Raman lines with decreasing crystal size) can be observed [26]. Moreover local symmetry distortion and cation disordering in the spinel cubic structure can lead to minor or major shifts and deformation of the Raman bands [27]. If there are defects in the materials, resulting in the disorder and decrease of crystallinity, the symmetry will be distorted and the Raman selection rules will be relaxed. [28].

Our films are composed of NPs of different size and phase-composition, so it is difficult to make conclusive interpretation of the spectra. Differences in spectrum may come also from the area of the surface observed (micro-Raman investigates a region of the surface of $2 \times 2\mu\text{m}^2$), because if the small NPs are uniformly distributed on the film, the big NPs are not. The number of big NPs in the analyzed zone influences the Raman signal. However we can say that the disappearance of the F_{2g2} peak of the Co_3O_4 in the spectrum of sample prepared at low P_{O_2} is a confirmation of a not completely crystalline phase of Co_3O_4 , due to the lower amount of oxygen in the chamber.

FTIR spectrum of $P_{O_2} = 4.5 \times 10^{-3}$ mbar displays a decrease in the intensity of signal at 389 cm^{-1} , and in general the width of the 660 cm^{-1} peak in FTIR spectrum decreases with increasing O_2 pressure, such as the width of the peak at about 560 cm^{-1} . CoO presents an absorption band at 550 cm^{-1} strongly overlapped with Co_3O_4 signals, so FT-IR analyses did not enable unambiguous conclusions regarding the mutual Co_3O_4 content [29]. However the increase of peaks broadening with decreasing P_{O_2} may be ascribed to a decrease of the Co_3O_4 phase, as further confirmed by the lower intensity of the peak located at 389 cm^{-1} .

Another works studied the effect of oxygen partial pressure on PLD deposition of cobalt in oxygen atmosphere [19]. The authors deposited cobalt oxide thin film (20nm) keeping the substrate temperature at 250°C and varying the O_2 pressure from

5. COBALT OXIDE NANOPARTICLES SYNTHESIZED BY PLD

10^{-4} to 10^{-2} mbar. The ablation of a Co target was performed in a reactive atmosphere produced by an $P(O_2)$ dynamic gas flow through a needle valve.

They found that film grown at the lower pressure of $P(O_2)$ are composed predominantly of cobalt, and have just a thin layer of CoO on the surface. When the pressure was increased up to 10^{-3} mbar the surface exhibit a Co_3O_4 phase, behind of which there is again a CoO phase. A small contribution of Co is still present. Increasing the $P(O_2)$ up to 10^{-2} mbar the content of Co_3O_4 increases. The CoO film has Co/O ratio slightly lower than 1 probably because of the preferential ion sputtering which can cause a partial reduction of oxide, as suggested. Two mechanisms of oxidation are proposed: a direct oxidation that happens only for $P(O_2)$ higher than 10^{-3} mbar and a surface oxidation occurred after the film deposition. They finally suggest that there is an increasing contribution of Co_3O_4 phase for films grown at higher O_2 pressure probably because the hot film surface after the deposition was exposed to enriched O_2 atmosphere before recovering the vacuum in the chamber.

These previously reported aspects are in agreement with our results for NPs.

5.4.3 Different target-to-substrate distance

For $d_{t-s}=8.5$ cm the NPs on the substrate have a spherical shape, while for $d_{t-s}=5.5$ cm the splash of big NPs on the substrate is evident (see fig. 5.23). This means that for short d_{t-s} the NPs arriving at the substrate are not well solidified, while for longer d_{t-s} the NPs reach the substrate already in the solid state. Increasing the distance the NPs suffer an higher number of collisions before reaching the substrate. Thus the NPs arrive at the substrate with a lower temperature than that for shorter d_{t-s} . Moreover sample deposited at low $d_{t-s}=8.5$ cm the NPs have a Co/O ratio near 1, while for lower d_{t-s} Co/O ratio is about 10. Even if the quantification of the oxygen could be underestimated due to X-Ray signal absorption effects, the comparison of the two value clearly show that the NPs in sample prepared at $d_{t-s}=8.5$ cm contains more oxygen than in sample where $d_{t-s}=5.5$ cm. This is because of the longer residence time of the droplets in the oxygen enriches atmosphere. When $d_{t-s}=5.5$ cm the NPs reach the substrate they have a mixed Co-hcp and CoO-phase, while for $d_{t-s}=8.5$ cm the NPs have been enough time to completely oxidize into CoO.

Then on the substrate the temperature of the NPs deposited at $d_{t-s}=5.5$ cm and the $P(O_2)$ are sufficiently high to allow the formation a Co_3O_4 shell. On the contrary for

5.4 Discussion on sample characterization

$d_{t-s}=8.5\text{cm}$ the NPs suffered many collisions so, even if the partial pressure of oxygen in the chamber is the same than for $d_{t-s}=5.5\text{cm}$, the Co_3O_4 phase cannot be formed because the NPs temperature is too low and the only T_{sub} can not sustain the Co_3O_4 phase formation.

Even for the small NPs we can adopt the previous argument. Indeed small NPs are CoO-phase for $d_{t-s}=8\text{cm}$, whilst they are CoO- and Co_3O_4 -phase for $d_{t-s}=5.5\text{cm}$.

After the solidification (still during the flight) the small NP for $d_{t-s}=8.5\text{cm}$ continue to collide with atoms in the plume loosing again their kinetic energy. When they reach the substrate they have low energy, with respect to NPs of sample synthesized at $d_{t-s}=5.5\text{cm}$, to diffuse on the substrate. So there is an increase of nucleation sites on the substrate. Indeed looking at SEM images when d_{t-s} increase then the density of the small NPs increases. Against there is a suppression of coalescence as confirmed by the decrease in mean diameter, for NPs obtained at higher d_{t-s} , measured by TEM.

Raman and FTIR do not show significant differences in peak positions among the samples. However increasing d_{t-s} the broadening of the peak in Raman spectra and that of the peak in FTIR spectra decreases.

As already said Raman and FTIR spectrum have to be interpreted carefully. We can surely say that for all the distances the Co_3O_4 phase prevail over the CoO phase. The narrowing of the A_{1g} mode in Raman spectrum and of the FTIR peaks let us believe that there is an increase in crystallinity (Co_3O_4 phase) for samples deposited at higher d_{t-s} .

The presence of the Co_3O_4 is justified by the higher number of pulses used for these samples, as explained before. Moreover increasing the d_{t-s} the number of big NPs decreases, and so the prevalent contribution to the FTIR and Raman signal comes from small NPs, more easily oxidized into Co_3O_4 .

The effect of target to substrate distance in PLD of nickel-oxide nanoparticles has been investigated by Zbroniec et al. [30]. They justify some discrepancies found especially in the areal number density of particles as caused by the effective fluence change at the target surface due to the optical setting difference of the laser beam line. However they found that shorter distance produced larger nanoparticles at an ambient pressure of 0.67 Pa. This confirms that nanoparticles formation does not take place in the plume. They supposed that NPs form via rapid surface diffusion [31] on the substrate. Collisions during the flight suppress the energy after landing without contributing to

5. COBALT OXIDE NANOPARTICLES SYNTHESIZED BY PLD

the growth. Indeed if the particles formed in the plume, the longer d_{t-s} would produce larger particles due to a longer residing time and more collisions. The authors also found that the correlation between particle areal density versus number of laser pulses changes with d_{t-s} . A shorter d_{t-s} produced a monotonically decreasing number density with increasing ablation time, whereas the longer d_{t-s} resulted in its gradual increase. In the shorter d_{t-s} case, particles have sufficient energy even after landing, resulting in an areal density decrease due to the coalescence of nanoparticles. On the other hand, when the d_{t-s} becomes larger, particles after landing do not have enough energy to move around, leading to the increase in the areal density.

We attributed the formation of NPs at phase explosion and hydrodynamic instabilities in the target, however we also found the same correlation between d_{t-s} and temperature of the NPs reaching the substrate. Phenomena of coalescence and diffusion on the substrate has been taken into account before, but between NPs already formed by ejection from ablated target and deposited on the substrate.

5.4.4 Different post-deposition treatment

For *post* – O_2 samples we found two different kind of big NPs: one with a core-shell structure, and a less amount of NPs formed completely of crystalline cobalt oxides. The core-shell NPs have a core of Co-hcp phase and an outer shell of CoO-phase. The core of the NP is composed only of metallic cobalt, unlike the other films, because during the flight of the droplets from the target to the substrate there is no oxygen in the chamber. After the deposition O_2 was introduced and the surface oxidation is initiated. The shell is always complete, unlike the other samples, because the oxidation time is higher. In fact in the previous case the chamber was evacuated immediately after the deposition, so the NPs were in contact with oxygen only for the time needed to evacuate the PLD chamber. The shell is CoO-phase. The particles suffer no collisions during the flight so they should reach the substrate with a temperature higher than the others, as confirmed by their different shape. However when the NPs come in contact with the surface there is no oxygen in the chamber and the NPs rapidly cool. Indeed we start putting O_2 in the chamber only at the end of the deposition and the time required to reach $P(O_2) = 10^{-2}$ mbar is of some tens of second.

So the oxygen should react with quite cold NPs ($T_{sub} = 250^\circ\text{C}$). In this condition only CoO can form (as seen also for sample prepared at low O_2 pressure).

Few big NPs are crystalline cobalt oxide phase. A possible explanation is that these particles undergo to a complete oxidation during the permanence in the enriched O_2 . Indeed the shell of the *post* – O_2 sample is very thick ($15 \div 30nm$) among the samples, comparable to NPs size.

Smaller NPs are Co_3O_4 phase because of the strongly dependence of oxidation on the size of the particle [32]. Moreover the temperature required for the formation of the Co_3O_4 phase of NPs of few nm can be lower than for big NPs [33].

Raman spectrum for *post* – O_2 sample shows only a weak signal related to Co_3O_4 phase, because of the presence of a small amount of cobalt oxide. Indeed even if the number of pulses is higher than for samples analyzed by TEM, only the NPs on the surface come in contact with oxygen, while the NPs below remain in the metallic Co phase.

Instead for the post-annealed samples there are clear signals coming from Co_3O_4 . In this case oxygen has been incorporated in the NPs during the flight, so NPs reach the substrate already in oxide phase. Then the substrate temperature at $250^\circ C$ made the Co_3O_4 crystallization possible. However only in this sample the relative intensity of the Eg mode is higher than that of the second peak (F_{1g2} mode and Si contribution) appearing in in the Raman spectra. Also FTIR reveals all the peaks assigned to Co_3O_4 , with the first one shifted to low wavenumber. This may indicate a difference in crystallization between post-annealed NPs and NPs deposited on a hot substrate, as testified also by the existence of complete crystalline cobalt oxide NPs in the post-annealed sample. This can be attributed to an higher permanence of the NPs on a hot substrate. Indeed annealing was performed for 30 minutes, while for other samples analyzed by TEM the NPs remained on the substrate only for the deposition time (less than one minute). At the end of the deposition the substrate was cooled down and when $T_{sub} = 25^\circ C$ (it requires about 70 minutes) the samples were removed from the chamber.

5.5 Final remarks

Several factors affect the final structure of the cobalt oxide NPs like the amount of oxygen available in chamber, the residence time in the oxygen enriched atmosphere, the substrate temperature, the number of collisions suffered by the NPs during the

5. COBALT OXIDE NANOPARTICLES SYNTHESIZED BY PLD

flight towards the substrate and the consequent temperature with which the NPs reach the substrate. The change of one deposition parameter often affects more than one of the factors just mentioned. In particular the distance from target to substrate influence both the number of collision (and so the final temperature of the NPs) and the residence time of the NPs in the O_2 enriched atmosphere. A variation in the oxygen partial pressure lead also to a variation in the number of collisions, and in the amount of O_2 available for oxidation. So by varying the deposition conditions we are able to obtain the following different cobalt oxide NPs:

- Co oxide big NPs (with size ranging from 10 to 100 nm);
- core/shell NPs (with size ranging from 50 of nm to 400 nm), with core composed of both metallic and oxide Co and a Co-oxide (CoO and/or Co_3O_4 phase) shell;
- core/shell NPs (with about the same size of the previous one), whit a core of Co-hcp and a CoO shell
- small (size of about 5 nm)NPs having CoO phase;
- small (as before) NPs having Co_3O_4 phase.

References

- [1] D. Chatterjee and S. Dasgupta. *J. Photochem. Photobiol. C*, 6:186, 2005. 63
- [2] R. Bauer, G. Waldner, H. Fallmann, S. Hager, M. Klare, T. Krutzler, S. Malato, and P. Maletzky. *Catalysis Today*, 53(1):131, 1999. 63
- [3] J.H. Ramirez, M.A. Vicente, and L.M. Madeira. *Appl. Catal. B: Environ.*, 98:10, 2010. 63
- [4] S.K. Ling, S. Wang, and Y. Peng. 178:385, 2010. 63
- [5] H. Li, G.T. Fei, M. Fang, P. Cui, X. Guo, P. Yan, and L.D. Zhang. *Appl. Surf. Sci.*, 257:6527, 2011. 64
- [6] N.N. Binitha, P.V. Suraja, Z. Yaakob, M.R. Resmi, and P.P. Silija. *Journal of Sol-Gel Science and Technology*, 53(2):466, 2010. 64
- [7] Y. Chen, L. Hu, Y. Min, and Y. Zhang. *Mater. Chem. Phys.*, 124:1166, 2010. 64
- [8] X. Lou, J. Han, W. Chu, X. Wang, and Q. Cheng. *Mater. Sci. Eng. B*, 137:268, 2007. 64
- [9] P. Raja, M. Bensimon, U. Klehm, P. Albers, D. Laub, L. Kiwi-Minsker, A. Renken, and J. Kiwi. *J. Photochem. Photobiol. A: Chem.*, 187:332, 2007. 64
- [10] A.Z. Moshfegh. *J. Phys. D: Appl. Phys.*, 42(233001):1, 2009. 64
- [11] B.R. Cuenya. *Thin Solid Films*, 518:3127, 2010. 64
- [12] T. Seike and J. Nagai. *Sol. Energy Mater.*, 22:107, 1991. 64
- [13] C.N.P. Da Fonseca, M.A. De Paoli, and A. Gorenstein. *Adv. Mater.*, 3:553, 1991. 64
- [14] T. Maruyama and S.J. Arai. *Electrochem. Soc.*, 143:1383, 1996. 64
- [15] F. Svegli, B. Orel, I.G. Svegli, and V. Kaucic. *Electrochim. Acta*, 45:4359, 2000. 64
- [16] K.B. Klepper, O. Nilsen, and H. Fjellvg. *Thin Solid Coat*, 515:7772, 2007. 64

REFERENCES

- [17] V. Pralong, J.B. Leriche, B. Beaudoin, E. Naudin, M. Morcrette, and J.M. Tarascon. *Solid State Ionics*, 166:295, 2004. 64
- [18] Y. Wang, Z.W. Fu, and Q.Z. Qin. *Thin Solid Coat.*, 441:19, 2003. 64
- [19] S. Laureti, E. Agostinelli, G. Scavia, G. Varvaro, V. Rossi Albertini, A. Generosi, B. Paci, A. Mezzi, and S. Kaciulis. *Appl. Surf. Sci.*, 254:5111, 2008. 64, 87
- [20] X. Gao, H. Guo, Y. Xia, J. Yin, and Z. Liu. *Thin Solid Coat.*, 519:450, 2010. 64
- [21] J. Alaria, N. Cheval, K. Rode, M. Venkatesan, and J.M.D. Coey. *J. Phys. D: Appl. Phys.*, 41(135004):1, 2008. 64
- [22] J.B. Goodenough M.M. Thackeray, W.I.F. David. *Mater. Res. Bull.*, 17(6):785, 1982. 67
- [23] V.G. Hadjiev, M.N. Iliev, and I.V. Vergilov. *J. Phys. C: Solid State Phys.*, 21:L199, 1988. 67
- [24] Y. Yonezawa, T. Minamikawa, K. Matsuda, K. Takezawa, A. Morimoto, and T. Shimizu. *Applied Surface Science*, 127–129(1–2):639, 1998. 86
- [25] D. Alloyeau, C. Langlois, C. Ricolleau, Y. Le Bouar, and A. Loiseau. *Nanotechnology*, 18:375301, 2007. 87
- [26] J. Tyczkowski, R. Kapica, and J. Lojewska. *Thin Solid Films*, 515:6590, 2007. 87
- [27] Michel Boucharda and Alessa Gambardella. *Journal of Raman Spectroscopy*, 41:1477, 2010. 87
- [28] Yan Zhao, Yijian Jiang, and Yan Fang. *Journal of Crystal Growth*, 307:278, 2007. 87
- [29] D. Barreca, A. Gasparotto, O. I. Lebedev, C. Maccato, A. Pozza, E. Tondello, S. Turner, and G. Van Tendeloo. *Journal of Crystal Growth*, 12(7):2185, 2010. 87
- [30] L. Zbronic, T. Sasaki, and N. Koshizaki. *Journal of Ceramic Processing Research*, 6(2):134, 2005. 89
- [31] G. Medeiros-Ribeiro, A. M. Bratkovski, T. I. Kamins, D. A. A. Ohlberg, and R.S. Williams. *Science*, 279:353, 1998. 89

REFERENCES

- [32] J. Alaria, N. Cheval, K. Rode, M. Venkatesan, and J.M.D. Coey. *Appl. Phys. Lett.*, 100(26):263111, 2012. 91
- [33] E. Roduner. *35*, 18:583, 2006. 91

REFERENCES

6

*TiO*₂-doped Cr/ITO multilayer thin films by R.F. sputtering

6.1 Introduction

The search for clean renewable energy is important to try solving problems related to emission of greenhouse gases from fossil fuels which contribute to dangerous climatic changes. Hydrogen, with its high gravimetric energy density, is a promising route to store renewable energy. Moreover, there is almost zero emission of environment pollutants when hydrogen is used as a fuel in proton exchange membrane fuel cell (PEMFC)[1]. Presently, about 95% of the total hydrogen is produced from fossil fuels by procedures that lead to increase in greenhouse gases [2]. Thus, to make the life cycle of hydrogen fuel to be clean and renewable it is very important to produce hydrogen gas from clean and renewable energy sources such as solar and wind. Photocatalytic water-splitting by using solar energy could contribute to the solution of environmental and energy issues related to the hydrogen production [3]. *TiO*₂ is the most preferred material to be used as photoelectrode in hydrogen production by photo-electrochemical water-splitting because it is: i) very resistant to corrosion and photocorrosion in aqueous media, ii) cheap and easily available, iii) environmentally clean, iv) with energy band edges which are well-matched with the redox level of water, and v) with electronic properties that can be varied by just changing the lattice defects chemistry or the oxygen stoichiometry [4]. In addition, *TiO*₂ is also the most desired material for the environment treatment technologies, mainly in purification of toxic

6. TiO_2 -DOPED CR/ITO MULTILAYER THIN FILMS BY R.F. SPUTTERING

compounds from polluted water and air [5, 6, 7]. However, TiO_2 is active only under ultraviolet (UV) light because of its wide energy band gap (~ 3.2 eV): this means that only a small portion (4 %) of the solar energy spectrum may be utilized for photocatalytic processes [8]. Thus, the better absorption of the solar spectrum is one of the important factors to be considered for the development of the TiO_2 as photocatalyst. Doping TiO_2 with foreign ions is one of the most promising strategies for sensitizing TiO_2 to visible light by forming impurity levels in the forbidden gap [8]. Recently, TiO_2 doped with 3d-transition metals (V, Cr, Mn, Fe, Cu, Co and Ni) have been mostly investigated because they are able to establish energy levels inside the band gap leading to significant visible light absorption for TiO_2 [9, 10, 11, 12, 13, 14]. However, the role of dopant transition metals on the photocatalytic activity is still under investigation. Indeed, while the formation of impurity energy levels should contribute to increase the absorption of photons having lower energy than the TiO_2 band gap, the lifetime of the charge carriers is however much shorter in transition metals doped- TiO_2 . Thus an increased recombination rate of charge carriers in doped- TiO_2 implies a reduction of the photocatalytic activity. A systematic investigation performed by Choi et al. [10] on the photocatalytic activity of TiO_2 doped with 21 different metal ions, proved that the charges recombination processes largely depend on both dopant concentration and type. Small concentration of transition metals (lower than 1 at.%) is able to introduce traps for electrons and/or holes, thus increasing the recombination time [11]. On other hand, this low concentration is not sufficient to significantly increase the absorption of the visible light in TiO_2 . High dopant concentration (about 5-10 at.%) causes an efficient narrowing of the TiO_2 band gap but at the same time it introduces new recombination centers for the photo-generated charges thus increasing recombination processes [15]. From previous consideration, it becomes important to solve the problem of recombination for these moderately doped TiO_2 . To this purpose, note that by using redox couple as electrolyte inside the photo-electrochemical cell can reduce the recombination processes to some extent [16, 17]. In addition, the charge separation can be further obtained by application of an external bias. However, the two above solutions are not convenient for commercial purposes related to solar energy conversion. The best way to suppress the recombination processes is to produce specific charge states to favor electrons and holes trapping while having appropriate spatial separation. This can be achieved by using coupled semiconductor layers having

appropriate electron energy levels where the edge of the conduction band of the first semiconductor is lower than that of the second one. If the semiconductor layers are not much thick, then the photogenerated electrons in one layer are easily injected into the second one [18]. In addition, a thin space charge layer of a few tens of nanometers is formed near the interface of the semiconductors to make their Fermi level equal [19]. The junction electric field is built up in this space charge layer of the electrode and is able to provide the driving force to the photogenerated electrons to move from one semiconductor to another thus favoring the electron-hole separation. Therefore, the development of a number of interfaces in the photoelectrode creates an ideal scenario to reduce the recombination rate. Many TiO_2 -based coupled systems such as CdS/TiO_2 [20], WO_3/TiO_2 [21], SnO_2/TiO_2 [22, 23], SiO_2/TiO_2 [24] etc., have been used in the past as photocatalysts. But none was reported using transition metal -doped- TiO_2 in the coupled system where the recombination rates are much higher.

6.2 Synthesis of the samples

Undoped and Cr-doped- TiO_2 thin films were synthesized by RF-magnetron sputtering using TiO_2 disc (purity equal to 99.99 %) and Ar gas (purity equal to 99.99 %) as sputtering target and working gas, respectively. Cr-doped TiO_2 films were synthesized by partially covering the TiO_2 target surface with small Cr-metal discs. The number of discs on the TiO_2 target was varied in order to obtain Cr-doped films of three different atomic concentrations. High vacuum (HV) with base pressure $< 3 \times 10^{-5}$ Pa and working Ar pressure of 0.8 Pa were used in the deposition chamber. Before film deposition, the TiO_2 target was pre-sputtered for 20 min in order to remove any surface contamination. The TiO_2 films were sputter-deposited on both glass and Si (100) substrates at room temperature using RF power of 150 W. The sample-target distance was kept constant at 5.5 cm for deposition of all the samples. After deposition, no post annealing was performed. To test photocatalytic activity, TiO_2 thin films were deposited on a conducting indium tin oxide (ITO) layer. The ITO layer, of about 80 nm, was deposited on the glass slide using magnetron sputtering with RF power of 100 W and working Ar gas pressure of 0.8 Pa. Pre-sputtering of the ITO target was also conducted to remove possible surface contamination. Multilayer coating was prepared by sequential in-situ sputtering, firstly of the ITO layer and then of Cr-doped TiO_2 : this

6. TiO_2 -DOPED CR/ITO MULTILAYER THIN FILMS BY R.F. SPUTTERING

forms a single bilayer. Similarly, several numbers of bilayers (3-, 4-, 5-, 6- and 7-bilayers) were deposited in order to study the efficiency of the adopted multilayer structure to reduce the recombination process of holes and electrons. The total thickness of Cr-doped TiO_2 was kept constant, about 750 nm, in all the multilayer films by controlling the sputtering deposition time. Thus, as the bilayers number increases, the thickness of the Cr-doped TiO_2 decreases in each bilayer to maintain constant the total thickness of TiO_2 in all films. The thickness of ITO (~ 80 nm) was kept constant in all the multilayer films irrespective of number of bilayers. The top surface of all the films was always covered with pure TiO_2 of ~ 100 nm to protect the metal ions from leaching out in the electrolyte.

The structural characterization of the sputter-deposited TiO_2 films was carried out by XRD technique (Cu K_α radiation, $\lambda = 1.5414\text{\AA}$) in Bragg-Brentano ($\theta - 2\theta$) configuration. Surface electronic states of the photocatalysts were established by using XPS. X-ray photoelectrons spectra were acquired using a SCIENTA ESCA200 instrument equipped with a monochromatic Al K_α (1486.6eV) X-Ray source and a hemispherical analyzer. No electrical charge compensation was required to perform XPS analysis. Optical measurements in the Ultraviolet (UV) and visible range were performed using a Bruker IFS66 spectrometer equipped with reflection and transmission units while the incoming beam was incident near to the surface normal. The measurements were performed in the wavelength range between 250 nm and 750 nm to obtain the absorbance spectra of TiO_2 samples deposited on glass slides. The surface morphology of the TiO_2 samples was analyzed by means of a SEM equipped with Energy Dispersive Spectroscopy (EDS) which permitted compositional studies of the films.

The performance of multilayer-Cr-doped TiO_2 films in photocatalytic water-splitting was tested by measuring both photocurrent and hydrogen production rates in photo-electrochemical cell which consists of TiO_2 as photo-anode, Pt mesh as cathode, and aqueous electrolytes. In order to establish a chemical bias we used two chambers containing electrolytes with different pH values. The TiO_2 photo-anode was kept in contact with a NaOH (1 M) solution, while the cathode was immersed in a H_2SO_4 (1 M) solution. A salt bridge containing NaCl (1 M) was used to provide a path for ion conduction between the two chambers. The photo-anode was exposed to visible light, generated by a 250 W tungsten halogen lamp, to measure both open-circuit photo-voltage and closed-circuit photocurrent. The reactor for water-splitting tests was prepared with

6.3 Characterization of the films and photocatalytic activity measurements

borosilicate glass that acts as a UV filter, while the reactant water solution is a filter for IR radiation. Oxygen from the reaction chamber was completely removed by purging the chamber with pure Ar gas (99.9%) for 1 h before performing measurements. The evolution of H_2 originated by the water-splitting process at the cathode was measured on-line, as a function of time, by using a gas chromatographer (GC, Agilent MIRCOGC-3000A). Finally, the hydrogen evolution was measured in both ON- and OFF- light regimes.

6.3 Characterization of the films and photocatalytic activity measurements

As observed by SEM, the surface morphology of the Cr-doped TiO_2 films appears quite flat, smooth, and without major defects, while the cross-section of the Cr-doped films showed a dense columnar structure. In addition, SEM images obtained in back scattering mode, show uniform distribution of Cr-ions in the TiO_2 film. The dopant concentration uniformity is clearly connected to the adopted co-deposition procedure. This feature was also confirmed, in the sampled volume, by compositional line scan using EDS. The Cr concentration of about 2 ± 0.2 , 5.5 ± 0.2 , and 9 ± 0.3 at.% was obtained in three different TiO_2 films as confirmed by EDS.

Fig. 6.1 shows the XRD spectra of the Cr-doped- TiO_2 films, of several concentrations, deposited by RF-magnetron sputtering on amorphous glass. The XRD peaks of pure TiO_2 are mainly due to the anatase phase while some weak additional reflexes are attributed to the rutile phase. The crystal grain sizes of the rutile and anatase phase are about 6 nm and 45 nm, respectively, as calculated by using the Debye-Scherrer equation. This means that the rutile phase is almost amorphous with very finely dispersed grains while, on the other hand, the anatase phase is in nanocrystalline form. The peaks due to rutile phase, with crystal grain size of about 35 nm, prevail over the anatase phase for TiO_2 films doped with low concentrations of Cr (~ 2 at.%). The reflexes of the rutile phase are now shifted to lower 2θ values, as compared to those of pure TiO_2 film. This indicates a slight increase in the spacing value between the lattice planes which might be caused by the insertion of Cr in the lattice. Complete transformation from anatase to rutile phase is observed in XRD pattern for higher concentration of Cr-doped TiO_2 (5.5 and 9 at.%) films. The peaks due to Cr oxides

6. TiO_2 -DOPED CR/ITO MULTILAYER THIN FILMS BY R.F. SPUTTERING

(Cr_2O_3 or CrO) formation were not detected by XRD. Cr^{3+} metal ions have an effective diameter comparable to that of Ti^{4+} ions thus, during deposition, the metal ions sputtered from the target with kinetic energy of some 10 eVs might be able to replace the Ti^{4+} ions in the lattice of TiO_2 without major variation in the crystal structure, at least for low doping concentration. However, high metal-acceptor dopant concentration causes the formation of oxygen vacancies whose mobility may account for the rearrangement of Ti^{4+} and O^{2-} ions in the lattice and finally favoring the anatase to rutile phase transformation [25] in the TiO_2 film.

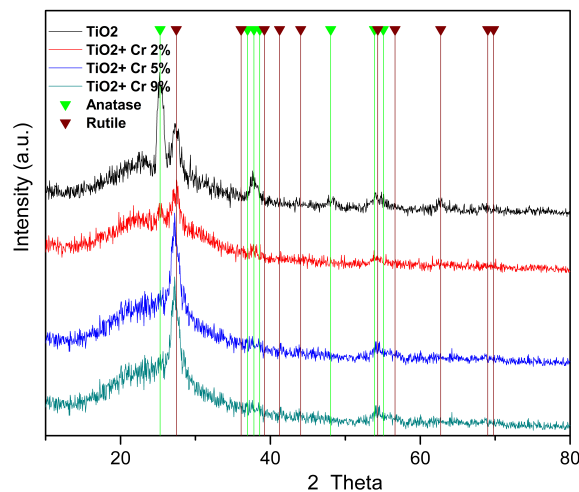


Figure 6.1: XRD spectra of undoped and Cr-doped TiO_2 films - deposited with different dopants concentration

The optical properties of the pure and Cr-doped TiO_2 were studied by measuring the absorption spectra ranging from UV (250 nm) to visible (750 nm) wavelengths and presented in fig. 6.2. The figures clearly show a shift in the absorption band edge towards longer wavelengths when increasing the Cr concentration in the TiO_2 film.

The band gap value is obtained by using the following equation [26]:

$$\alpha h\nu = \alpha_0(h\nu - E_g)^\gamma \quad (6.1)$$

where E_g is the optical band gap, $h\nu$ is the photon energy, $h\nu_0$ is a constant which does not depend on $h\nu$, and α is the absorption coefficient which is obtained from

6.3 Characterization of the films and photocatalytic activity measurements

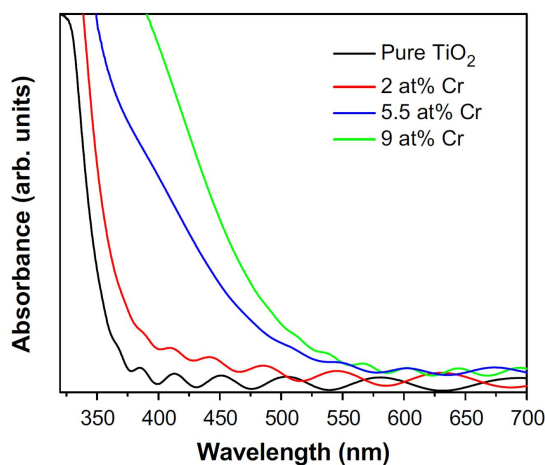


Figure 6.2: UV-VIS absorption spectra of undoped and Cr-doped TiO_2 films - deposited with different dopants concentration

the measured absorbance (A) and thickness (t) of the TiO_2 film through the relation: $\alpha = A/t$. Depending on the type of transition, γ assumes different values: for direct, allowed (forbidden) transitions $\gamma = 1/2$ ($\gamma = 3/2$) and for indirect, allowed (forbidden) transitions $\gamma = 2$ ($\gamma = 3$). We used $\gamma = 2$ for the present nanocrystalline or amorphous films according to ref. [27].

Using Tauc plot (fig. 6.3) for the UV-VIS absorption spectra, i.e. $(\alpha h\nu)^{1/2}$ versus $(h\nu)$, the band gap energies were deduced by extrapolating the linear region of the plot to intersect the photon energy axis: the obtained values are reported in table 6.1.

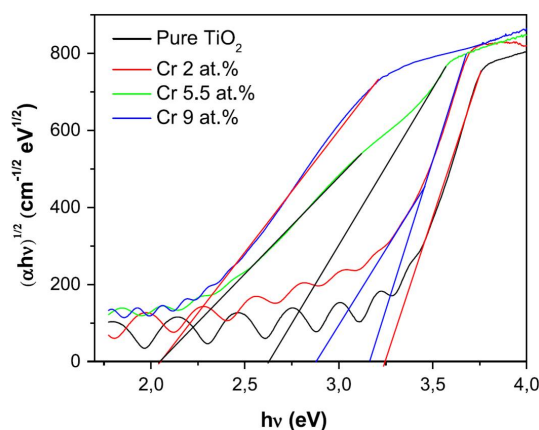


Figure 6.3: Tauc plot of undoped and Cr-doped TiO_2 films - deposited with different dopants concentration

6. TiO_2 -DOPED CR/ITO MULTILAYER THIN FILMS BY R.F. SPUTTERING

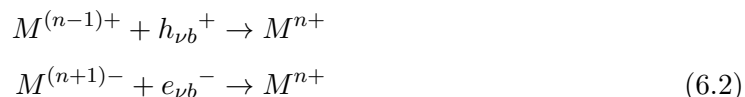
Cr concentration in TiO_2 film (at.%)	TiO_2 optical band gap values (eV)	Doping energy level values (eV)
Cr concentration in TiO_2 film (at.%)	TiO_2 optical band gap values (eV)	Doping energy level values (eV)
Pure TiO_2	3.25 ± 0.2	–
2 at.%	3.17 ± 0.2	2.85 ± 0.2
5.5 at.%	2.63 ± 0.2	2.1 ± 0.2
9 at.%	2.1 ± 0.2	–

Table 6.1: TiO_2 optical band gap and doping energy level values for undoped and Cr-doped TiO_2 films deposited by RF-magnetron sputtering with several Cr concentration

For sputter-deposited pure TiO_2 films a band gap of 3.25 eV is obtained: it signals the presence of a well-crystallized anatase phase. In case of Cr-doped TiO_2 films, by increasing the Cr concentration a red shift of the absorption edge is noticed. In 9 at.% Cr-doped TiO_2 , a relevant lowering of the photon-absorbed energy from ~ 3.2 eV (pure TiO_2) to ~ 2.1 eV, is observed. During sputter deposition, Cr^{3+} ions may have enough energy to displace the Ti^{4+} ions from their lattice positions thus creating lattice vacancies where the impurity metal ions get incorporated into the TiO_2 films. This incorporation leads to formation of new energy levels, due to Cr^{3+} , at ~ 1 eV above the valence band of the TiO_2 [28]. When excited with visible light 3d-electrons are transferred from Cr^{3+} to the conduction band of TiO_2 : this explains the observed increased absorption [28]. In addition, a characteristic bend of the linear part in the experimental plot can be recognized (fig. 6.3) whose extrapolation establishes the doping energy level in the band gap [26]. This feature is mainly observed in TiO_2 doped with low Cr concentration (2 at.%) showing energy level at 2.85 eV (table 6.1). However at high Cr concentration, the density of the doping energy level causes the definite narrowing of the band gap as shown in the UV-visible spectra. These results definitely prove that we were able to sensitize TiO_2 in visible light range by doping with Cr^{3+} ions. As seen from the above results, Cr-doped TiO_2 with 9 at.%, shows the maximum lowering of the photon-absorbed energy and thus we preferred to perform the photocatalytic activity measurements only with these doped-films by making comparison with undoped TiO_2 . Henceforth, 9 at.% Cr-doped TiO_2 film will be designated as Cr9-doped TiO_2 film.

6.3 Characterization of the films and photocatalytic activity measurements

Cr9-doped TiO_2 film (about 750 nm thick) was deposited on an ITO layer (80 nm), previously deposited on glass substrate, and the obtained bilayer was covered with thin layer of pure TiO_2 to protect the film from possible corrosion induced by contact with the electrolyte. This single bilayer film was used as photocatalyst for water-splitting experiments. The ITO/ TiO_2 stack film is able to partially limit the recombination of photo-generated holes and electrons (h^+ and e^-) because the conduction band edge of ITO (~ -4.5 eV) is at an energy value lower than that of TiO_2 (~ -4.0 eV) thus making favorable for the electrons injection from the later into the former. The open-circuit photo-voltage (V_{oc}) was first measured in light-ON regime in photo-electrochemical cell by using Cr9-doped and undoped TiO_2 films as photo-electrode. Both these films show a photo-voltage value of about 1.45 V which is greater than the required voltage (1.23 V) to break the water molecule. However, the photocurrent measured using Cr9-doped TiO_2 ($\sim 14\mu A$) is negligible as compared to pure TiO_2 films ($\sim 290\mu A$). This is mainly due to recombination of the photo-generated charges on defects associated to the Cr^{3+} ions. High concentration of metal ions leads to the recombination of the photo-generated h^+ and e^- accordingly to the following equations 6.2:



This means that doping TiO_2 with 9 at.% of Cr has two effects:1) titania is sensitized to the visible light range, and 2) recombination centers are formed where the photo-generated electrons and holes recombine by limiting the photocatalytic activity. To avoid the recombination problem we may lower the concentration of Cr in the TiO_2 film. But this will cause lower absorption of the visible light. In addition, the low concentration of Cr in TiO_2 is unable to completely solve the problem of recombination, as reported in a previous work of our laboratory team[29].

A simple and efficient route to suppress the recombination of charge carriers is by immediately removing the photoelectron from the generation site before it recombines with the holes through radiative or non-radiative processes. This fast separation can be achieved through the use of coupled semiconductors with appropriate conduction energy levels. For instance, as mentioned previously, in the ITO/ TiO_2 coupled system, the conduction band edge of ITO (~ -4.5 eV) is at an energy value lower than that

6. TiO_2 -DOPED CR/ITO MULTILAYER THIN FILMS BY R.F. SPUTTERING

of TiO_2 (~ -4.0 eV) thus making favorable for the electrons injection from the later into the former. Once the photoelectron from TiO_2 is injected in ITO, it has a very low probability of back transfer and, as a result, electrons and holes are definitely separated. However, to be efficient, ITO should be located near the electron generation site to provide the driving force for the photoelectron transfer.

Having this in mind, we have deposited multilayer films with different numbers (3-, 4-, 5-, 6- and 7-bilayers) of ITO/Cr9- doped TiO_2 bilayers and finally covering with thin layer of pure TiO_2 (100 nm) the surface layer that will be in contact with the electrolyte. The bottom portion of the overall multilayers is also in contact with the electrolyte through the pure TiO_2 (100 nm) layer (while the corresponding top portion is electrically connected to cathode of the photo-electrochemical cell). The total thickness of Cr9-doped TiO_2 was kept constant, about 750 nm, in all the multilayer films by decreasing the thickness of each Cr9-doped TiO_2 layer when increasing the number of the bilayers. The thickness of ITO (~ 80 nm) was kept constant in all the multilayer films irrespective of number of bilayers. In a previous work made by our laboratory group[30], the effect of conducting ITO layer on photocatalytic activity was studied by varying the thickness of the ITO films and we found that ITO layers having thickness in the range of 50-100 nm offer the best conditions to have low losses of absorbed photon energy thus favoring better photo-voltage.

In fig. 6.4 we present the cross-section SEM images, in back scattering mode, of multilayer films with 1-, 3-, 4-, 5-, 6- and 7- bilayers of ITO/Cr9-doped TiO_2 . The white layer of ITO can be easily distinguished from the dark layer of Cr9-doped TiO_2 and for this reason both the periodicity and continuity of the layers are clearly visible. The images clearly show that along with the increase of bilayers number, the thickness of single Cr9-doped TiO_2 layer decreases (see fig. 6.5).

Here we want to note that ITO deposited on the top of TiO_2 layer does not affect the amount of photons reaching the TiO_2 layer because ITO is a transparent conducting oxide with a direct band gap in the range of 3.9-4.2 eV which is significantly higher than the absorption edge of Cr9-doped TiO_2 layer (2.1 eV). This feature was experimentally confirmed by measuring the absorbance of the Cr9-doped TiO_2 -ITO bilayers, with ITO on top, in the UV-Visible range: the spectra showed similar red shift in the band edge as that observed with single layer. To check the photocatalytic activity of the multilayer films we measured photo-voltage and photocurrent for light-ON regime in

6.3 Characterization of the films and photocatalytic activity measurements

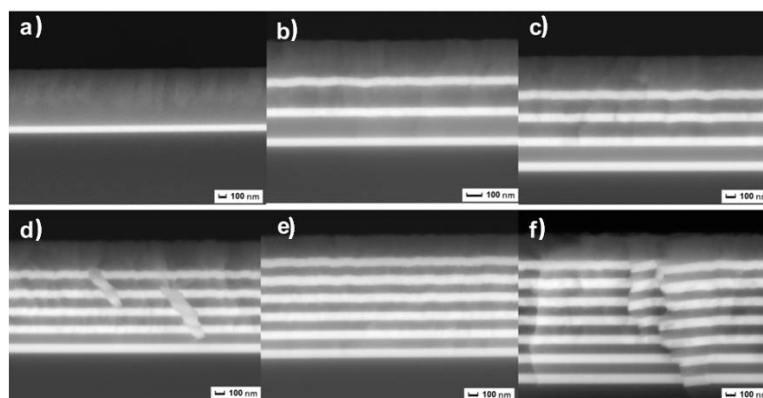


Figure 6.4: SEM Images, in back scattering mode, of ITO/Cr9-doped TiO_2 multilayer films - a) single bilayer, b) 3-bilayers, c) 4-bilayers, d) 5-bilayers, e) 6-bilayers, and f) 7-bilayers

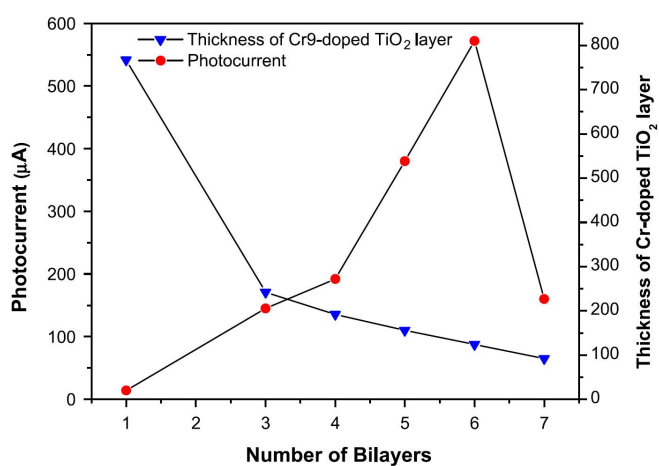


Figure 6.5: Photocurrent and thickness of each Cr9-doped TiO_2 layer as a function of number of bilayers -

6. TiO_2 -DOPED CR/ITO MULTILAYER THIN FILMS BY R.F. SPUTTERING

photo-electrochemical cell by using ITO/Cr9-doped TiO_2 multilayer films as photo-anode. Each ITO layer in the multilayer films is directly connected to the platinum cathode and so as soon as the electrons are injected from the Cr9-doped TiO_2 layers into the ITO layers, they are immediately transferred to the cathode. The photo-voltage measured on all the multilayer films (about 1.4-1.5 V) is greater than that required to split the water molecule. The measured photocurrent as a function of number of bilayers is reported in fig. 6.5.

As the number of ITO/Cr9-doped TiO_2 bilayers increases the photocurrent increases and reaches the maximum value with 6-bilayers (572 μA). However, with 7-bilayers the photocurrent decreases to the value of 160 μA . The photocurrent value measured with 6-bilayers Cr9-doped TiO_2 film (572 μA) is about two times higher than that obtained with pure TiO_2 (290 μA) with same total thickness of TiO_2 . When semiconductors having different energy bands are brought in contact with each other, a band bending occurs near the interface to make Fermi level equal on both sides. This band bending generates an interface space charge layer, having thickness of several tens of nanometer, where a large electric field is developed. When photoelectrons are generated in this interface region (or very near) they are instantaneously pushed out to the adjacent semiconductor due to the driving force provided by the electric field and the electron-hole separation is definitely obtained, a process well known in p-n semiconductor junctions. In the present ITO/ TiO_2 system, the interface region presents electrical features that are similar to previously described pen junction thus providing an efficient route for the e-h separation. Hence by adopting a multilayer structure, we are able to produce many interfaces of ITO/ TiO_2 which establish fast transport channels along with efficient e-h separation. electron flow in the multilayer films and how the number of bilayers affects the generation of the photocurrent.

6.4 Discussion on sample characterization

Our results show that the photocurrent obtained with single bilayer of ITO/Cr9-doped TiO_2 is very low. In this single bilayer film there is only one interface of ITO/Cr9-doped TiO_2 at the bottom with the thick layer of Cr9-doped TiO_2 (750 nm) over it. Most of the photoelectrons are generated in the bulk of the doped- TiO_2 where they have to travel some distance within the TiO_2 itself before entering the space charge

6.4 Discussion on sample characterization

region of the interface to feel the driving field for final injection into ITO. In Cr9-doped TiO_2 the probability of e-h recombination is much higher because of the presence of recombination sites associated to the Cr^{3+} ions. By depositing 3-bilayers film the photocurrent increases significantly from $14 \mu A$ (for single bilayer film) to $145 \mu A$. In this film, the previous Cr9-doped TiO_2 layer having thickness of 750 nm was divided into three layers of 250 nm by introducing two more ITO layers. The resulting film now contains five ITO/ TiO_2 interfaces where space charge layer is formed and the decreased thickness of the Cr9-doped TiO_2 layers assures that the photo-generated electrons have to travel a short distance into TiO_2 (the unshielded region) before being injected into the ITO layer where recombination is definitely hindered. Another relevant point to be considered is that in single bilayer film the photoelectrons, generated in the Cr9-doped TiO_2 layer, to avoid recombination have to move only along one direction towards the ITO layer placed at the bottom of the layered structure. On the contrary, in 3-bilayers film the Cr9-doped TiO_2 layer is sandwiched between the two ITO layers and so the photoelectrons can move along either of two directions to avoid recombination. All these reasons favor the increment of the photocurrent in the 3-bilayers film.

In addition we observe that by increasing the bilayers number there is an almost linear increment in the photocurrent, mainly attributed to the better conditions for charge separation and transport with reduced number of recombination processes: here we have to further underline the key role of number of ITO/ TiO_2 interfaces. The measured photocurrent reaches the maximum value ($572 \mu A$) with 6-bilayers film; the measured photocurrent is significantly higher than that measured with single bilayer film ($14 \mu A$). For 6-bilayers film, the thickness of Cr9-doped TiO_2 layer (125 nm) in each bilayer may be lower than the total thickness of the space charge layer of the pertinent interface. Thus photoelectrons generated in the Cr9-doped TiO_2 are already in space-charge region where the electric field provides them the driving force to instantaneously inject into the ITO layers: this means that the 6-bilayers film creates the best conditions for charge separation. In addition, this film is able to absorb more visible light than pure TiO_2 due to the band narrowing caused by Cr^{3+} energy levels, hence generating higher amount of photoelectrons. With 7-bilayers film the photocurrent decreases (fig. 6.5); we suggest this might be due to the poor crystallinity of very thin films of TiO_2 (92 nm).

6. TiO_2 -DOPED CR/ITO MULTILAYER THIN FILMS BY R.F. SPUTTERING

Takahashi et al. [31] showed indeed that with sol-gel deposited TiO_2 film the photocurrent increases by decreasing the TiO_2 layer thickness and reaches maximum value at particular thickness. Below this thickness the photocurrent decreases drastically and, as indicated by the authors, this is attributed to the low crystallinity achieved with thinner films. Nasr et al. [18] also reported a similar trend in the photocurrent as a function of TiO_2 thickness but they did not explain the reason behind the reduced photocurrent with thinner TiO_2 layers. For the moment with our XRD setup it is difficult to acquire the spectra of such a thin layer of TiO_2 .

The reduced probability in charge recombination processes observed with multilayer films can be further analyzed by studying the photocurrent kinetics curve. Fig. 6.6A shows the schematic diagram of photocurrent transient curve.

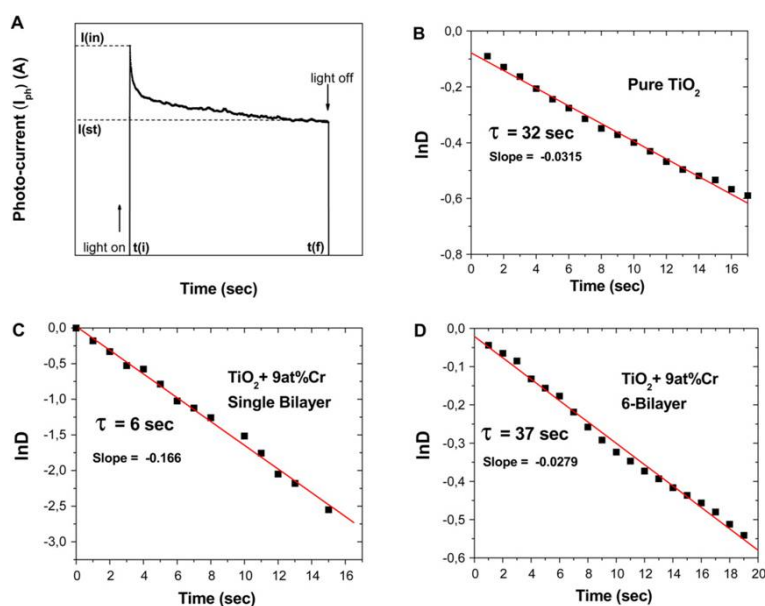


Figure 6.6: A) Schematic representation of the photocurrent transient curve. Normalized plot of current-time dependence for: B) pure TiO_2 , C) single bilayer, and D) 6-bilayers of ITO/Cr9-doped TiO_2 multilayer film -

The initial anodic photocurrent spike is denoted by $I(i)$. This current signals the separation of the electron-hole pairs by movement of holes towards the semiconductor surface where they are trapped or reduced by the species in the electrolyte, while the electrons are transported to the back contact. After $I(i)$ has been attained, then a continuous decrease of the photocurrent with time is observed until a steady-state

photocurrent, $I(st)$, is reached. The photocurrent decay indicates that charge recombination processes are occurring. The holes reaching the semiconductor surface may, instead of capturing electrons from the electrolyte, accumulate at the surface and recombine with electrons from the conduction band, i.e. the decay is determined by the rate at which minority carriers trapped at surface states capture majority carriers [32]. The photocurrent transient can be defined by the following kinetic equation [33] (eq. 6.3):

$$D = \exp\left(-\frac{t}{\tau}\right) \quad (6.3)$$

where D is defined as (eq. 6.4):

$$D = \frac{I(t) - I(st)}{I(in) - I(st)} \quad (6.4)$$

Here, τ is the transient time constant, $I(t)$ is the current at time t , $I(in)$ is the current at $t = 0$, and $I(st)$ the stationary current.

Figs. 6.6B, C, and D illustrate the $\ln(D)$ vs. time plot for pure TiO_2 film, single bilayer, and 6-bilayers of ITO/Cr9-doped TiO_2 films respectively. The slope of this plot provides s which is related to the time for charge recombination processes in the films. The measured s for Cr9-doped TiO_2 with single bilayer film is about five times smaller than that for the undoped TiO_2 . Specifically, the photocurrent decays within a few seconds in Cr-doped TiO_2 is due to recombination of the photo-generated charges on defects associated to the Cr^{3+} ions. On the contrary, with 6-bilayers the transient time constant is about the same as for undoped TiO_2 film where there are no defect sites. This again proves that by introducing space charge regions in form of ITO/ TiO_2 interfaces and by decreasing the thickness of TiO_2 layer favors charge separation, and recombination processes are suppressed even if recombination sites such as Cr^{3+} are still present.

After optimizing the thickness of the Cr-doped TiO_2 in the multilayer films, it is necessary to study the effect of the number of bilayers on the photocurrent. Thus we deposited different number of ITO/ TiO_2 bilayers by keeping constant the thickness of Cr9-doped TiO_2 and ITO layers (125 and 80 nm respectively). The photo-voltage and photocurrent measured in light-ON regime with these multilayer films are reported in table 6.2.

6. TiO_2 -DOPED CR/ITO MULTILAYER THIN FILMS BY R.F. SPUTTERING

number of ITO/ TiO_2 bi-layers	Photo-voltage (V)	Photocurrent (μA)
1	1.321	92
2	1.329	190
4	1.393	315
6	1.4	572
7	1.345	551

Table 6.2: Photo-voltage and photocurrent measured for different numbers of ITO/ TiO_2 bilayers

All the multilayer films were able to produce photo-voltage greater than 1.3 V irrespectively on the number of bilayers. On the contrary, the photocurrent increases with the number of bilayers and reaches a nearly constant value for the highest number of bilayers (6 and 7). A saturation effect is clearly expected on physical basis but what is important here is that the photocurrent value depends not only on thickness but also on the number of bilayers, i.e. on the ability of the multilayer structure to efficiently avoid charges recombination. Here, another important point is that with 7-bilayers there is not a dramatic decrease of the photocurrent as observed in fig. 6.5. This supports the point that the low crystallinity achieved with very thin films is deleterious to photocurrent generation.

The photocatalytic activity of the 6-ITO/Cr9-doped TiO_2 bilayers was finally tested by measuring the amount of H_2 generated by water-splitting in photo-electrochemical cell and compared to pure TiO_2 . Fig. 6.7 shows the H_2 evolution, as function of time, from water-splitting by irradiating the multilayer and pure TiO_2 films with light (250 W tungsten halogen lamp) which contains mostly visible light and includes a very small portion of UV light (1%).

The amount of the photocatalytically produced H_2 increases linearly with the exposure time. The H_2 production completely stops after termination of light irradiation: this proves that H_2 is only produced photocatalytically. The constant production rate observed in the present case is simply due to the employ of TiO_2 photocatalyst in form of thin film in an apparatus [27] where H_2 and O_2 evolve separately. During the measurement, the same amount of surface area (13.75 cm^2) is exposed to the light for both the films. The H_2 generation rate was measured to be $24.4 \pm 0.1 \mu\text{mol}/h$ for 6-bilayers

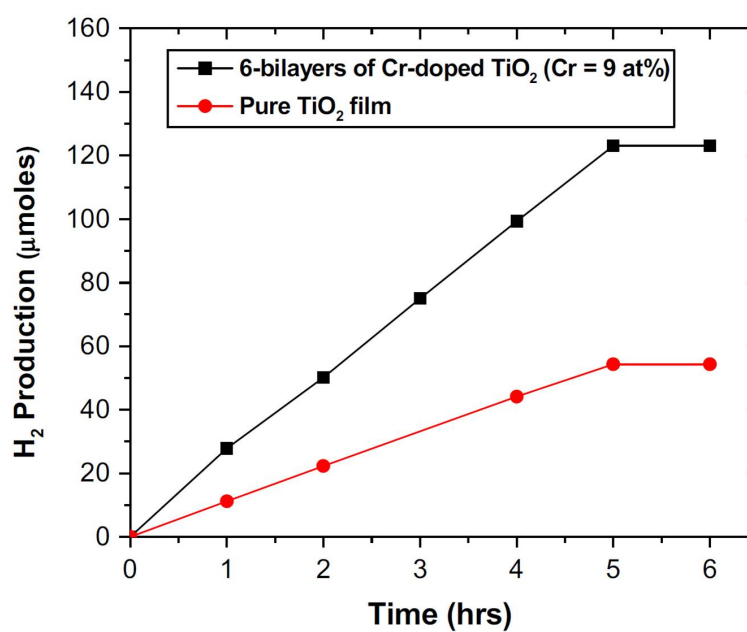


Figure 6.7: Hydrogen evolution, as a function of time, from water-splitting by using sputter-deposited pure TiO_2 and 6-bilayers of ITO/Cr9-doped TiO_2 multilayer film in photoelectrochemical cell containing two electrolytes of different pH - (see procedure in ref. [26])

6. TiO_2 -DOPED CR/ITO MULTILAYER THIN FILMS BY R.F. SPUTTERING

based Cr9-doped TiO_2 multilayer film and is about two times higher than that measured with pure TiO_2 film ($12.5 \pm 0.1 \mu mol/h$). The greater H_2 generation rate with Cr9-doped TiO_2 multilayer film is definitely attributed to an increased absorption of visible light, larger than pure TiO_2 , and to reduced charge recombination processes because of the number of space charge ITO/ TiO_2 interfaces in multilayer films. However, a comment must be included now to explain the hydrogen production results. Indeed, while the photo-generated electrons are easily collected by the established electrical contact to produce the measured photocurrent, the positive holes that are produced inside the Cr-doped TiO_2 layers sandwiched by the ITO films, may arrive at the TiO_2 irradiated surface that is in contact with water. We suspect that holes migrate through the bottom deposited layer towards the irradiated front surface where H_2O molecules get oxidized. This holes mobility is a new aspect, regarding the photo-electrochemical cells, that should be further investigated. Therefore the above results prove that:

- There is an enhanced visible light absorption in Cr-doped TiO_2 because of the formation of wide Cr^{3+} energy levels into the band gap;
- There is a better photo-generated charge separation by introducing space charge layers in form of ITO/ TiO_2 interfaces;
- Holes mobility towards the irradiated surface layer is a relevant new process that should be further investigated.

References

- [1] AL. Dicks. *J. Power Sources*, 61:113, 1996. 97
- [2] P.K. Cheekatamarla and C.M. Finnerty. *J. Power Sources*, 160:490, 2006. 97
- [3] M. Momirlan and T.N. Veziroglu. *Renew. Sustain. Energy. Rev.*, 6:141, 2002. 97
- [4] T. Bak, J. Nowotny, M. Rekas, and C.C. Sorrell. *Int. J. Hydrogen Energy*, 27:991, 2002. 97
- [5] H. Zhang, X. Quan, S. Chen, H. Zhao, and Y. Zhao. *Sep. Purif. Technol.*, 50:147, 2006. 98
- [6] H. Yamashita, M. Harada, J. Misaka, M. Takeuchi, B. Neppolian, and M. Anpo. *Catal. Today*, 84:191, 2003. 98
- [7] M. Anpo, S. Dohshi, M. Kitano, Y. Hu, M. Takeuchi, and M. Matsuoka. *Annu. Rev. Mater. Res.*, 35:1, 2005. 98
- [8] A. Fujishima, X. Zhang, and D.A. Tryk. *Surf. Sci. Rep.*, 63:515, 2008. 98
- [9] M. Ni, M.K.H. Leung, D.Y.C. Leung, and K. Sumathy. *Renew. Sustain Energy Rev.*, 11:401, 2007. 98
- [10] W.Y. Choi, A. Termin, and M.R. Hoffmann. *J. Phys. Chem.*, 84:13669, 1994. 98
- [11] M.I. Litter and J.A. Nav'ro. *J. Photochem. Photobio. A Chem.*, 98:171, 1996. 98
- [12] M.A. Khan, S.I. Woo, and O.B. Yang. *Int. J. Hydrogen Energy*, 33:5345, 2008. 98
- [13] J. Zhu, Z. Deng, F. Chen, J. Zhang, H. Chen H, and M. Anpo et al. *Appl. Catal. B Environ.*, 62:329, 2006. 98
- [14] A. Xu, J. Ng, X. Zhang, H. Bai, and D.D. Sun. *Int. J. Hydrogen Energy*, 35:5254, 2010. 98
- [15] M. Radecka, M. Rekas, A. Trenczek-Zajac, and K. Zarrzewska. *J. Power Sources*, 181:46, 2008. 98

REFERENCES

- [16] E.A. Kozlova, T.P. Korobkina, A.V. Vorontsov, and V.N. Parmon. *Appl. Catal. A Gen.*, 367:130, 2009. 98
- [17] R. Abe, K. Sayama K, and H. Arakawa. *Chem. Phys. Lett.*, 379:230, 2003. 98
- [18] C. Nasr, P.V. Kamat, and S. Hotchandani. *J. Phys. Chem. B*, 102:10047, 1998. 99, 110
- [19] S.R. Morrison. New york. *Plenum Press*, 1984. 99
- [20] Y. Chi, H. Fu, L. Qi, K. Shi, H. Zhang, and H. Yu. *J. Photochem. Photobio. A Chem.*, 195:357, 2008. 99
- [21] K.K. Akurati, A. Vital, J.P. Dellemann, K. Michalow, T. Graule, and D. Ferri et al. *Appl. Catal. B Environ.*, 79:53, 2008. 99
- [22] J. Shang, W. Yao, Y. Zhu, and N. Wu. *Appl. Catal. A Gen.*, 257:25, 2004. 99
- [23] R. Sasikalaa, A. Shirolea, V. Sudarsana, T. Sakuntalab, C. Sudakarc, and R. Naikc et al. *Int. J. Hydrogen Energy*, 34:3621, 2009. 99
- [24] E. Beyers, E. Biermans, S. Ribbens, K. De Witte, M. Mertens, and V. Meynen et al. *Appl. Catal. B Environ.*, 88:515, 2009. 99
- [25] F.C. Gennari and D.M. Pasquevich. *J. Am. Ceram. Soc.*, 82:1915, 1999. 102
- [26] J. Domaradzki. *Thin Solid Films*, 497:243, 2006. 102, 104, 113
- [27] Y. Djaoued, S. Badilescu, P.V. Ashrit, Y. Djaoued, S. Badilescu, P.V. Ashrit, D. Bersani, P.P. Lottici, J. Robichaud, D. Bersani, P.P. Lottici, and J. Robichaud. *J. Sol-Gel Sci. Tech.*, 24:255, 2002. 103, 112
- [28] T. Umebayashi, T. Yamaki, H. Itoh, and K. Asai. *J. Phys. Chem. Solids*, 63:1909, 2002. 104
- [29] R. Dholam, N. Patel, M. Adami, and A. Miotello. *Int. J. Hydrogen Energy*, 34: 5337, 2009. 105
- [30] R. Dholam, N. Patel, M. Adami, and A. Miotello. *Int. J. Hydrogen Energy*, 33: 6896, 2008. 106

REFERENCES

- [31] M. Takahashi, K. Tsukigi, T. Uchino, and T. Yoko. *Thin Solid Films*, 388:231, 2001. 110
- [32] A. Hagfeldt, H. Lindstrom, S. Sodergren, and S.E. Lindquist. *J. Electroanal. Chem.*, 381:39, 1995. 111
- [33] M. Redecka, M. Wierzbicka, S. Komornicki, and M. Rekas. *Physica B*, 348:160, 2004. 111

REFERENCES

7

Synthesis and characterization of Pb nanowires

7.1 Introduction

Metal-NWs have superconducting, magnetic, catalytic, and sensing properties of considerable practical importance [1]. In particular Pb NWs have the ability to cause size-based variation in critical superconductor temperature [2], have high corrosion resistance as electrode in acid batteries [3], and their high surface area and reactivity enhance the electrochemical degradation of pollutants[4].

Pb-NWs are mainly synthesized by templating into the nano-pores of anodic alumina or track-etched polycarbonate membrane using electro-deposition [5, 6]. This is a complicated method involving several steps to firstly synthesize the nanoporous membrane as a template and then etch the membrane to obtain free-standing NWs. Elemental Pb-NWs can also be produced by solution-phase approach but their inability to attain vertical alignment, restrict them for possible application [7]. The most common approach to grow NWs is by catalyst-assisted vapor-liquid-solid (VLS) mechanism but it suffers from major disadvantages because of contamination by catalyst material in the NWs and this method is mainly restricted to non-metallic NWs.

Stress-assisted growth of NW is more simple and low-cost approach with possibility of large-scale production at room temperature [8, 9, 10].

We synthesized Al-films with Pb NWs by radio frequency (RF) magnetron sputtering where compressive stress, induced in the co-deposited film, provides the driving

7. SYNTHESIS AND CHARACTERIZATION OF PB NANOWIRES

force for the NWs growth at room temperature and humidity produces sites for NWs extrusion.

7.2 Results and Discussion

Composite Al-films with embedded Pb atoms were synthesized by RF-magnetron sputtering in a vacuum chamber with base pressure $< 3 \times 10^{-5} Pa$. Al (99.5 % pure) disc partially covered with small Pb-metal discs were used as sputtering target. We use Ar (99.99 %) as working gas. The substrates were washed thoroughly with acetone and deionized water before loading them into the sputtering chamber.

Before film deposition, the target was pre-sputtered for 10 min in order to remove any surface contamination.

We varied several deposition parameters in order to understand the process of NWs growth: sample-target distance, deposition time, Pb concentration, and substrate material.

The results obtained varying these parameters lead us to focus our attention on the role of oxygen and ambient atmosphere on NWs growth. So we deposited new films on Si substrate keeping constant the working Ar gas pressure, the deposition time and the sample-target distance for all the samples. Then we kept the as-deposited samples in different environments after the deposition. Finally we analyzed the differences between the films stored in different conditions.

The surface morphology of the sputter-deposited samples was studied by scanning electron microscope (SEM-FEG, JSM 7001F, JEOL) equipped with energy-dispersive spectroscopy analysis (EDS, INCA PentaFET-x3) to determine the composition of the samples. The structural characterization of the sputter-deposited films was carried out by X-ray diffraction (XRD) technique (Cu K_α radiation, $\lambda = 1.5414 \text{ \AA}$) in Bragg-Brentano ($\theta - 2\theta$) configuration. The chemical features of the film have been analyzed with X-Photoelectron Spectroscopy (XPS) (SCIENT ESCA 200, with monochromatic Al K_α radiation, $= 8.340 \text{ \AA}$) equipped with hemispherical analyzer.

7.2.1 Pb concentration

A working Ar gas pressure P_{Ar} of 1.5 Pa and a RF power of 150 W were used during all the deposition. We use Si(100) substrate, kept at room temperature. Finally the

sample-target distance d_{t-s} was set at 7 cm for the deposition of all the samples. The number of Pb pieces on the Al target was varied in order to vary the atomic concentration of Pb in the film.

Samples having Pb total concentration c_{Pb} of 1 at. %, 7 at. %, 25 at. % have been obtained, as shown respectively in fig 7.1, 7.2 and 7.3.

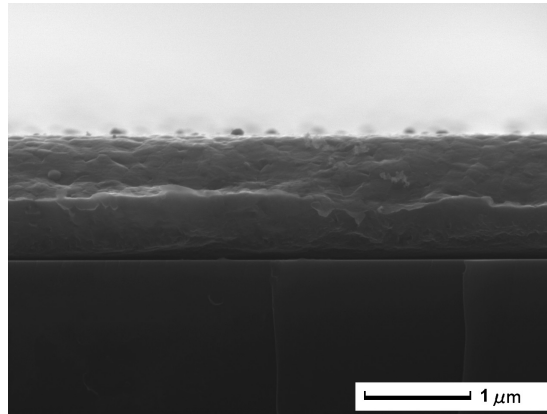


Figure 7.1: AlPb film: low Pb Concentration - Cross-section SEM image of Al-Pb film with concentrations: 1 at. % of Pb.

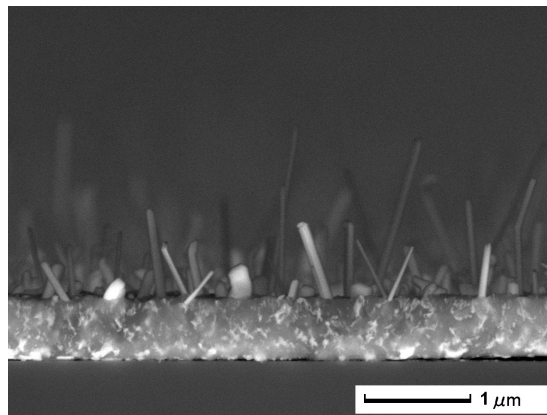


Figure 7.2: AlPb film: mid Pb Concentration - Cross-section SEM image of Al-Pb film with concentrations: 7 at. % of Pb.

Before transferring to the SEM analysis chamber, some composite films were kept in air, also for more than 24 h (without air exposition, Pb-NWs are not observed as we will see below). Note that at 25 at.% of Pb, the NWs grow at the bottom of the Al film after detachment from the Si substrate. Film with the lowest concentration of

7. SYNTHESIS AND CHARACTERIZATION OF PB NANOWIRES

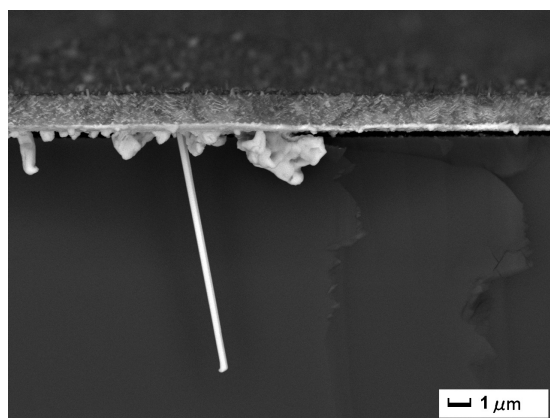


Figure 7.3: AlPb film: high Pb Concentration - Cross-section SEM image of Al-Pb film with concentrations: 25 at. % of Pb.

Pb (fig.7.1) doesn't show any NWs on the surface. Film with medium concentration (fig.7.2) clearly shows the presence of a lot of NWs of different length and orientation on the surface. On the contrary, increasing the Pb concentration up to 25 at.% no NWs grew on the surface (fig. 7.3). In this case, Pb segregates near the bottom of the Al matrix forming a continuous layer of Pb. When the film starts detaching from the substrate we can see Pb whiskers and hillocks extrusion from the bottom of the film.

7.2.2 Focus on nanowires

The broad view of SEM image (fig. 7.4) shows that Pb NWs appear on the surface of the Al film by uniformly covering large area.

The higher magnification image (fig.7.5) clearly shows that NWs are in form of almost circular rods with diameter in the narrow range of 60-100 nm. We can also see extrusion marks (fig.7.6) on the NWs that are typical of stress-induced growth thus suggesting that stress relief is the driving force for whisker growth also in the in-situ growth[9].

The height of the NWs varies significantly throughout the film surface with no correlation between diameter and length of the NWs that are randomly oriented over the film surface.

An EDS analysis was performed on crossing NWs scrapped out from the surface (fig. 7.7) to have an indication on the elemental composition of the NWs.

The results obtained are summarized in the following table 7.1:

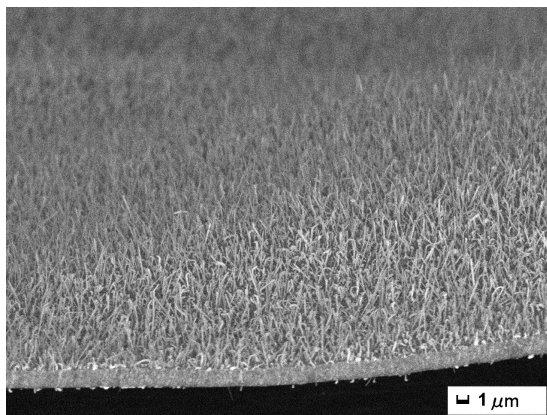


Figure 7.4: In plan general view of AlPb film - SEM cross-section micrograph of Pb NWs grown on the surface of the AlPb film(back-scattered electrons)

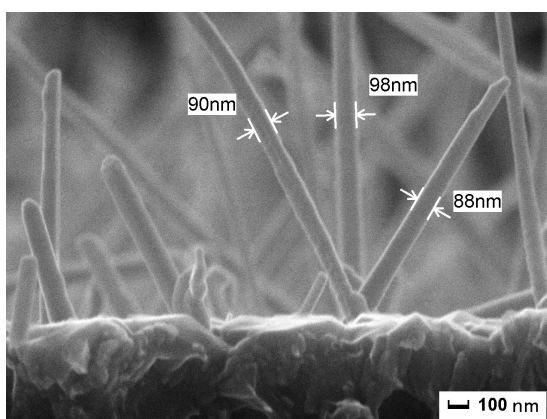


Figure 7.5: Lateral view - SEM cross-section micrograph of Pb NWs grown on the surface of the AlPb film

Spectrum	Atomic % O	Atomic % Pb
Spectrum 1	78.2	21.8
Spectrum 2	99.8	0.2
Spectrum 1 - Spectrum 2	73.9	26.1

Table 7.1: Quantitative results of EDS analysis - The difference between Spectrum 1 and Spectrum 2 gives the NWs composition.

7. SYNTHESIS AND CHARACTERIZATION OF PB NANOWIRES

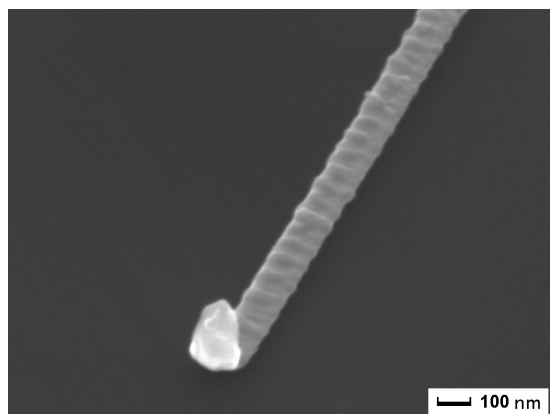


Figure 7.6: Magnified NW - SEM cross-section micrograph of Pb NWs grown on the surface of the AlPb film

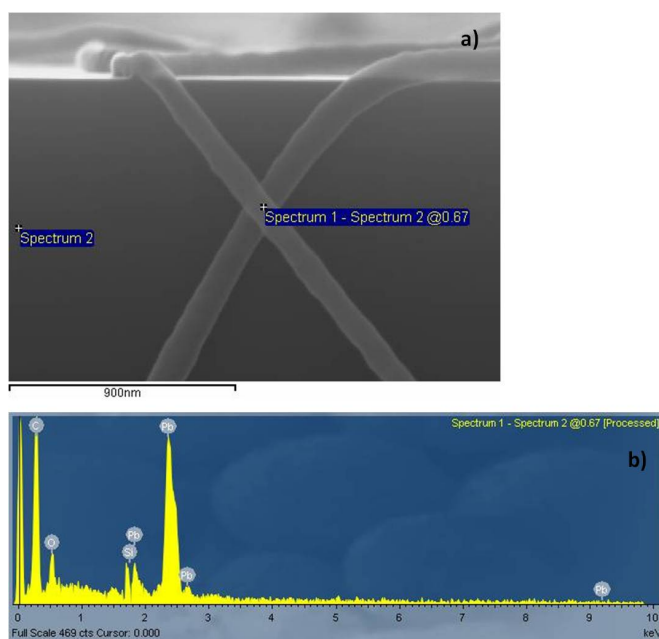


Figure 7.7: Elemental composition of NWs - a) two isolated NWs b) EDS spectrum difference between spectrum taken on the crossing area of NWs (spectrum 1) and spectrum of the bulk (spectrum 2)

To better observe the initial growth of the NWs we prepared a sample with the same P_{Ar} and d_{t-s} of the previous ones, but we use c_{Pb} around 2 % at. and a deposition time of 20 minutes. More important we exposed the sample to air only for few hours before analyzing it with SEM (as we will discuss the exposure to ambient atmosphere is essential for NWs growth). NWs appear to be extruded through the grain boundaries of Al (fig. 7.6).

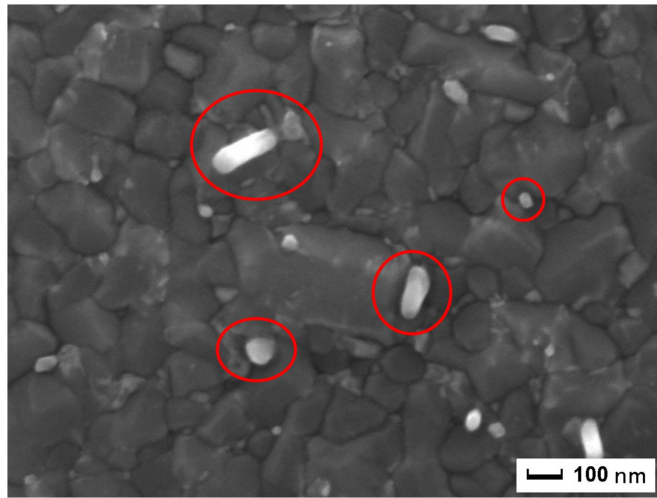


Figure 7.8: AlPb: focus on grain boundary - SEM image of AlPb film, with the extrusion region of the NWs highlighted

7.2.3 Substrate material

We performed the deposition for 90 minutes on four substrates of different material: silicon, copper, quartz, and stainless steel. We kept the same values of P_{Ar} and d_{t-s} than for the previous samples, and we choose the Pb concentration leading to NWs grown on Si substrate, that means $c_{Pb}=7$ at. %. After the depositions the samples were left in the air, as before, and then analyzed by SEM.

As shown in figures 7.9, 7.10, 7.11,7.12 NWs grew regardless of substrate.

7.2.4 Deposition time

We varied the deposition time keeping the same deposition parameters used before and choosing Si (100) as substrate: 1, 3, 5, 7, 10, 15, 20, 40, 60 min (see images from fig.

7. SYNTHESIS AND CHARACTERIZATION OF PB NANOWIRES

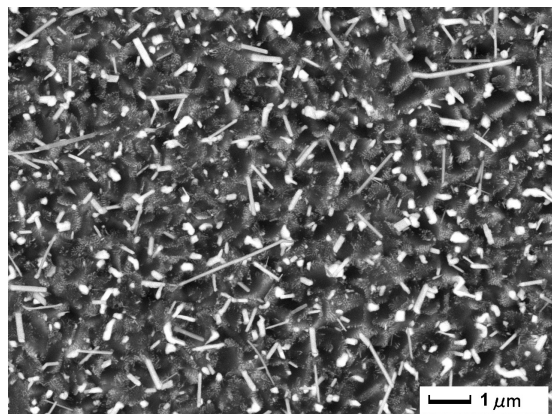


Figure 7.9: Copper substrate - SEM micrograph of Al-Pb film deposited on copper

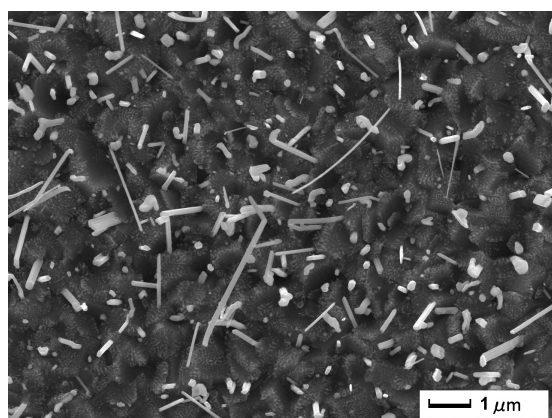


Figure 7.10: SiO₂ substrate - SEM micrograph of Al-Pb film deposited on quartz

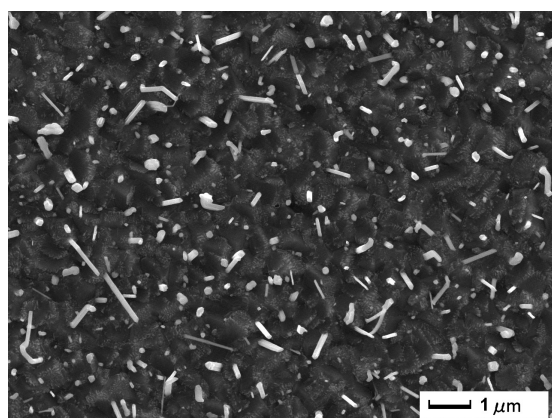


Figure 7.11: Silicon substrate - SEM micrograph of Al-Pb film deposited on Si(100)

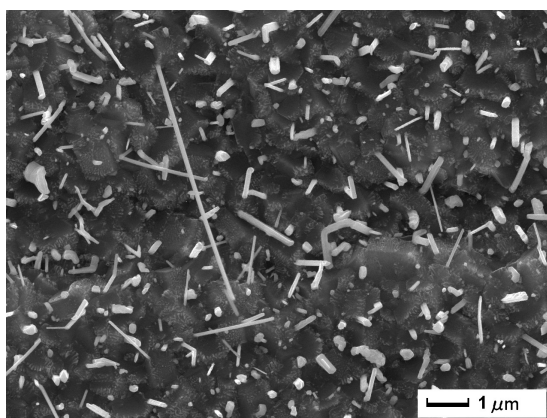


Figure 7.12: Stainless steel substrate - SEM micrograph of Al-Pb film deposited on SS

7.13 to 7.20). Again, we left the samples in air for few hours and then analyzed them by SEM.

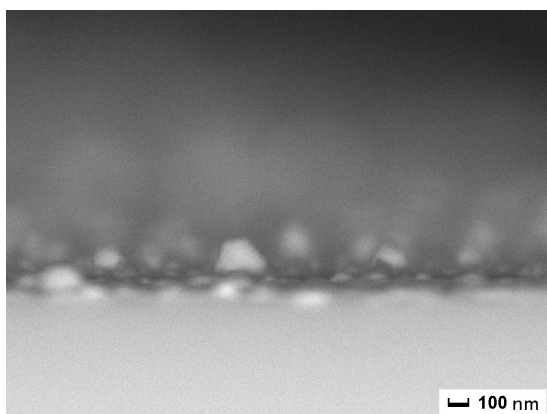


Figure 7.13: AlPb film: 1min deposition time - SEM micrograph of Al-Pb film (back-scattered electrons)

For 1 min deposition we found only nano-sized Pb agglomerations (fig. 7.13). Increasing the deposition time, NWs start to appear on the surface and for 60 min deposition we obtained NWs having maximum length up to 25 μm (fig. 7.20).

7.2.5 Al/Pb sputtering deposition

To assess that co-sputtering is essential to form Pb NWs, we deposited pure Pb film over previously deposited Al film on Si substrate. We load one Al target and one Pb

7. SYNTHESIS AND CHARACTERIZATION OF PB NANOWIRES

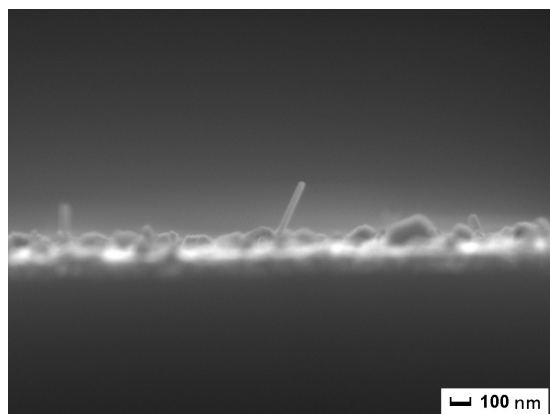


Figure 7.14: AlPb film: 3min deposition time - SEM micrograph of Al-Pb film

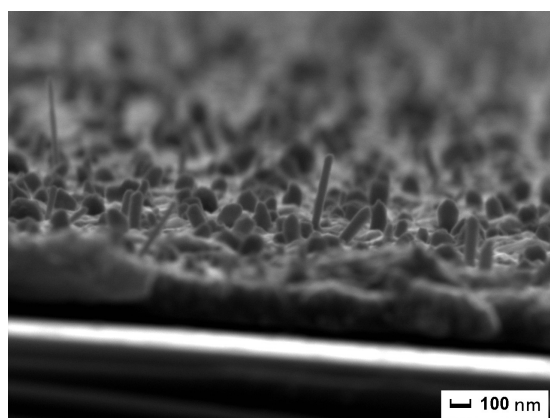


Figure 7.15: AlPb film: 5min deposition time - SEM micrograph of Al-Pb film

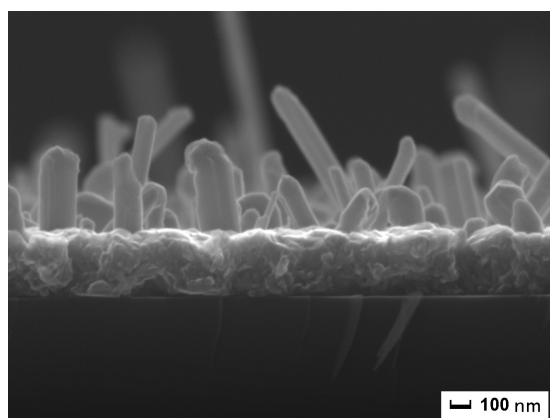


Figure 7.16: AlPb film: 7min deposition time - SEM micrograph of Al-Pb film

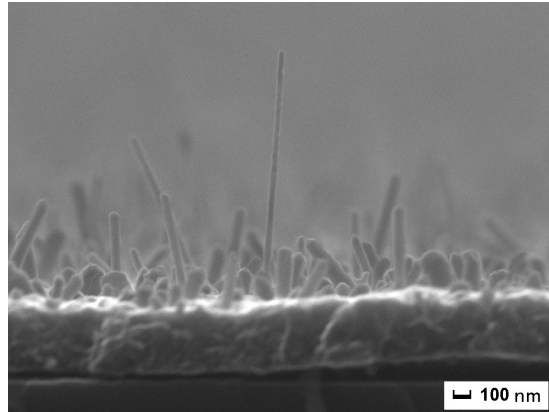


Figure 7.17: AlPb film: 10min deposition time - SEM micrograph of Al-Pb film

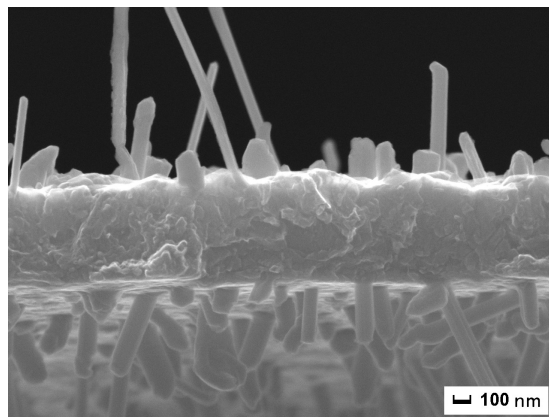


Figure 7.18: AlPb film: 15min deposition time - SEM micrograph of Al-Pb film

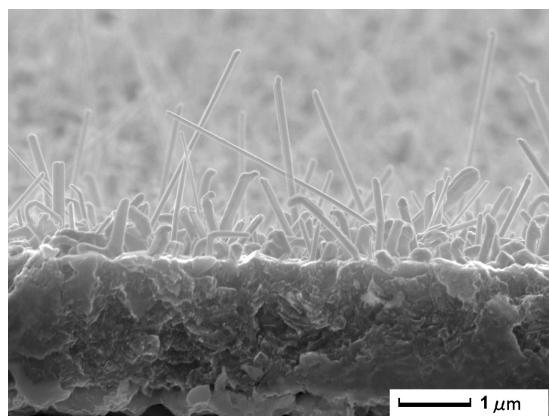


Figure 7.19: AlPb film: 40min deposition time - SEM micrograph of Al-Pb film

7. SYNTHESIS AND CHARACTERIZATION OF PB NANOWIRES

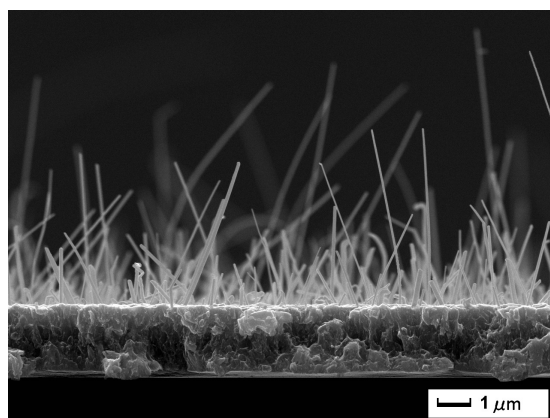


Figure 7.20: AlPb film: 60min deposition time - SEM micrograph of Al-Pb film

target on the sputtering chamber, so that we can perform the two-layer deposition without breaking the vacuum. We use $P_{Ar}=1.5$ Pa, $d_{t-s}=7$ cm and Si (100) substrate, for the deposition of both Al and Pb. The Al was deposited on the Si for 20 minutes, then the Pb was deposited on the Al film for 7 min.

Only big whiskers (7.21) or hillocks (fig. 7.22) of Pb were observed at SEM on the surface without any Pb NWs. The extrusion marks on the wire are evident and the hillock in some cases could suggest the shape of the grain boundary. Moreover on the top of each pillar there is a defined geometrical structure (fig. 7.23).

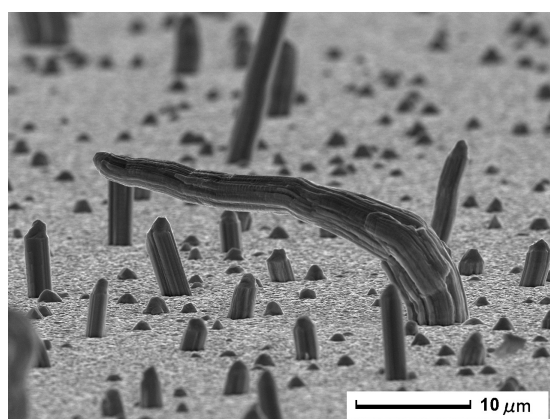


Figure 7.21: Pb whisker on Al: - SEM micrograph of whisker of pure Pb film deposited on Al film

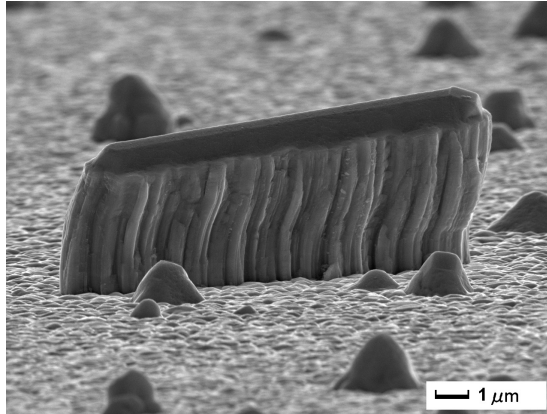


Figure 7.22: Pb hillock on Al: - SEM micrograph of hillock of pure Pb film deposited on Al film

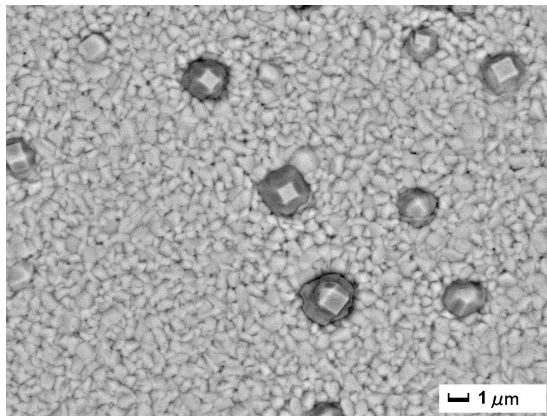


Figure 7.23: Top view of Pb on Al: - SEM micrograph of surface of pure Pb film deposited on Al film

7. SYNTHESIS AND CHARACTERIZATION OF PB NANOWIRES

7.2.6 Pb doped Al

To better understand the role of co-presence of Al and Pb in the film, we used Pb as matrix element and Al as dopant. The result observed at SEM was completely different from that of the AlPb films. The film is mainly composed of grains of lead, probably covered by the Al, as seen in fig. 7.24.

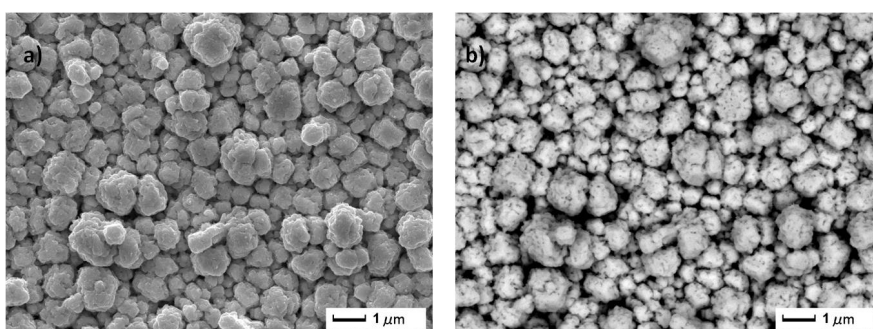


Figure 7.24: Pb film doped Al: surface - SEM micrograph of surface of pure Pb film deposited on Al film: a)secondary electrons, b)back-scattered electrons

We observe the presence of some pillar of lead having length of tens of m (fig. 7.25). The top of the wire looks similar to the surface of the film, revealing that the wires grow from the bottom.

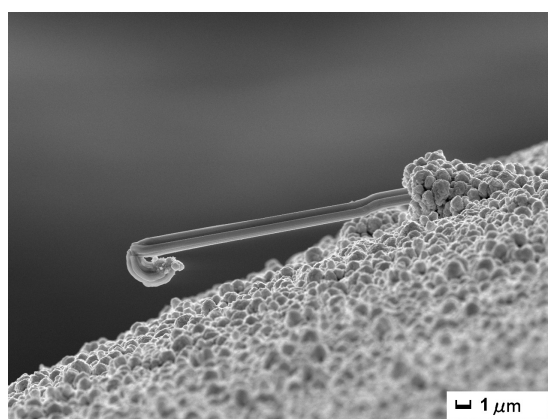


Figure 7.25: Pb film doped Al: micro-structures - SEM micrograph of pillar of Pb grown on the surface of the AlPb film

7.2.7 XRD results

Figure 7.26 displays the XRD pattern of Al-film with Pb-nanowires synthesized by RF-sputtering. The parameters used for the deposition of this samples are: $P_{Ar} = 1.5 \times 10^{-2}$ mbar, $d_{t-s} = 7$ cm and $c_{Pb} = 7$ at. %. The figure 7.26 reveals the polycrystalline structure of metallic Pb and Al. In addition, we note the absence of any peak related to Pb oxides excluding the presence of crystalline metallic Pb oxide nanowires.

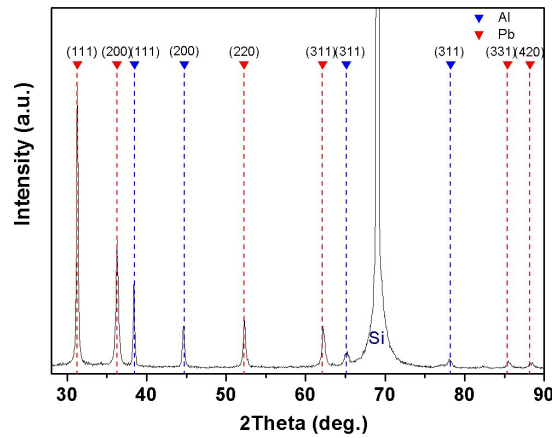


Figure 7.26: XRD of AlPb films -

7.2.8 XPS results

To gain additional insight on the obtained NWs, we have analyzed the sample surface with X-ray photoelectron spectroscopy.

The XPS analysis confirms the presence of Al oxide (fig. 7.27a), just in form of Al_2O_3 (peak located at 75.65 eV)[11] (we will see below how just this Al oxide is relevant in permitting the growth of the Pb NWs). Pure metallic Al is signalled by the peak located at 72.85 eV[12].

Metallic Pb (fig.7.27b) is signalled by the $Pb4f^{7/2}$ peak located at 136.9 eV[13]. Pb oxide (fig.7.27b) is suggested by the presence of the peak at 139.9 eV that however is shifted by about 1 eV with respect to the literature value probably because of local charging effects during analysis. Since charging is not observed with Al, we may suggest that a local charging occurs on the NWs. The absence of peak shift for metallic Pb may suggest that Pb surface oxide along the external surface of Pb NWs is not uniform.

XPS detects photoelectrons that are emitted from the surface or just below the surface

7. SYNTHESIS AND CHARACTERIZATION OF PB NANOWIRES

(up to about 5 nm) of the material being analyzed. The fact that we see the Al metallic peak in XPS spectra implies that the Al oxide layer is not thicker than about 5 nm.

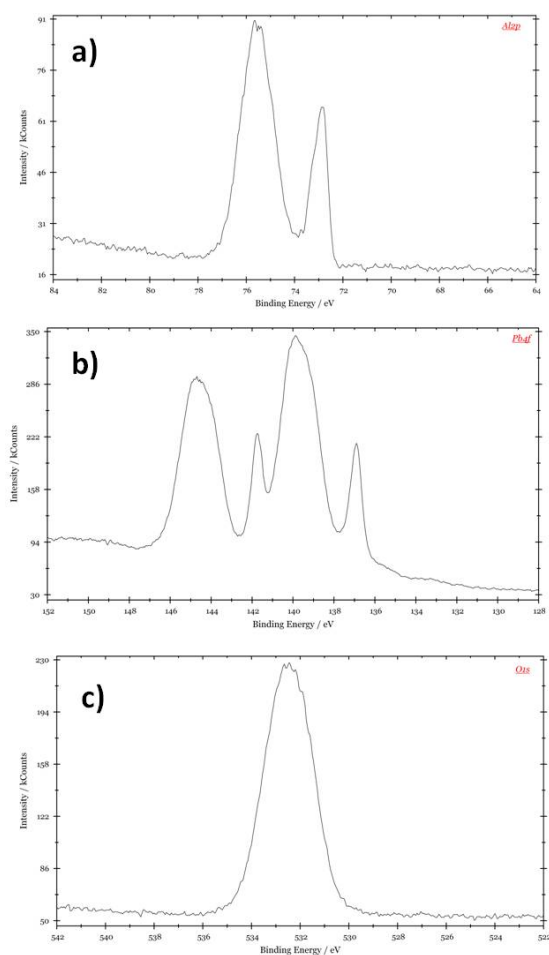


Figure 7.27: XPS spectrum related to the: - a) Al_{2p} peaks for oxide and metallic Al, b) Pb_{4f} peaks for oxide and metallic Pb, and c) O_{1s} peaks .

7.3 Discussion on deposition parameters influence on NWs formation

Inference on the basic process behind the NWs growth can be made observing the case studies provided.

Recently, Sn NWs were grown by co-sputtering deposition of Si-Sn film and heated at 180°C[8]. The large difference in thermal expansion coefficient (TEC) between Si and

7.3 Discussion on deposition parameters influence on NWs formation

Sn generates compressive stress in the composite film which acts as the driving force for the NWs growth.

Similarly, Bi NWs were grown on the SiO_2 substrate by stress-induced due to large difference in TEC.[9] But in our case there is very small difference in the value of TEC of Al ($23 \times 10^{-6} K^{-1}$) and Pb ($28 \times 10^{-6} K^{-1}$) and NWs grow at room temperature that means that thermal compressive stress can certainly be excluded.

Chemical compressive stress can be induced in the film by chemical reaction between different elements leading to the formation of intermetallic phase whose volume expansion creates the required stress to initiate the growth of NWs. Cheng et al [10] showed the self-extrusion of Te NWs from Si-Sb-Te thin film due to the incomplete chemical decomposition of $Si_2Sb_2Te_5$ phase in the film. Al and Pb are immiscible at any temperature for any concentration and so the stress created by chemical reaction between them is certainly not possible in our case.

The density and size of the Pb nanostructures change by varying the concentration of Pb into the Al matrix. Film with 1 at. % concentration of Pb doesn't show NWs because the amount of Pb is too low to support the growth of NWs by extrusion. For 7 at. % Pb concentration, stress builds up in the film and its relief lead to NWs extrusion. With 25 at. %, Pb atoms segregate to form a continuous layer at the interface between the film and the substrate. The stress is released by extrusion of whiskers and hillocks from the bottom of the film after detachment, a process that is comparable to Pb whiskers formation on the surface of a pure Pb film over Al film.

As shown in the related section, the choice of substrate doesn't influence the growth of NWs, so possible chemical reactions or differences in thermal expansion coefficient between substrate and film have no influence on NWs growth. This proves that extrusion of the NWs is due to relaxation of the stresses induced in the film during deposition.

The maximum length of NWs increases with RF-sputtering deposition time, ranging from about 50 nm (3 mins deposition) to tens of μ m (60 mins deposition), because by increasing the thickness of the deposited film, an increased amount of Pb is initially present that contributes to the NWs growth.

We assume that the stress is generated by the Al-Pb co-sputtering deposition. A stress, typical of sputtering deposition, is present due to the mechanical atomic peening by sputtered energetic particles.

Moreover sputtered atoms ejected into the gas phase can mix easily in the Ar plasma,

7. SYNTHESIS AND CHARACTERIZATION OF PB NANOWIRES

so when they condense on the substrate a supersaturated alloy of the two elements can be formed [14]. However Al and Pb are immiscible in solid phase with a positive heat of mixing, so the Al-Pb alloy can only exist in a metastable form. Thus the film is stressed and to attain equilibrium, a thermodynamically driven segregation takes place [15] which results in a phase separation between Al and Pb to lower the Gibbs free energy.

The film produced by sputtering deposition is polycrystalline which means that the favourable sites for Pb segregation are dislocation, grain boundary, stacking fault or interface between different materials [16]. In addition, it is well known that Pb impurities in Al segregate and simulations show that in presence of aluminum grain boundaries Pb tends to segregate along the boundary [17]. A clear indication of this is found in fig. 7.8. A residual stress is present in the as deposited film. Indeed Pb has an higher atomic radius than Al so the segregation of Pb at grain boundary causes the build-up of stress.

That is not the case of pure Pb deposited on a layer of Al, where the formation of larger wires and hillock is observed. In case of Pb deposited over Al film the dimension of the whiskers is limited only by the balance between the gain in strain energy reduction and the formation of the surface of the whisker [18].

7.4 Different storage conditions

To investigate more in detail the mechanisms involved on the NWs growth, we deposited seven Al-Pb film with $P_{Ar}=1.5$ Pa, $d_{t-s}=7$ cm and $c_{Pb}=7$ at. %:

1. one piece was immediately analyzed with SEM,
2. a second piece was kept in ambient condition (53% RH) for 24 h
3. the third piece was kept in vacuum condition (10^{-3} mbar) for 24 h,
4. the forth piece was kept in argon atmosphere for 24 h (1 atm),
5. the fifth piece was kept in oxygen atmosphere for 24 h (1 atm),
6. the sixth piece was annealed at $100^{\circ}C$ in vacuum condition (10^{-3} mbar) for 2 h,

7. the seventh piece was kept in a desiccator containing silica gel at 17% RH.

The storage chamber is evacuated with a scroll pump before putting inside oxygen and sample. In this way the sample is stored in a dry ambient. The SEM images of the seven pieces are presented from fig 7.28 to fig. 7.34 respectively.

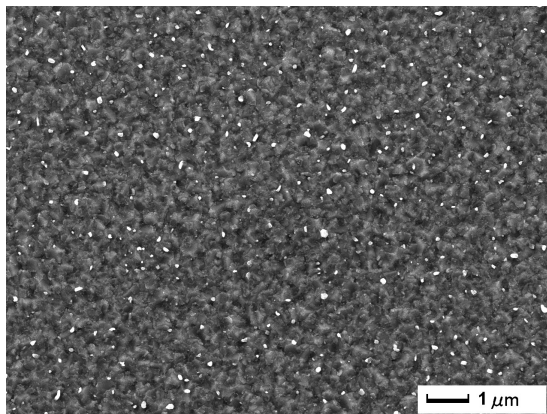


Figure 7.28: AlPb film: as-deposited sample: - SEM micrograph of the sample immediately after deposition

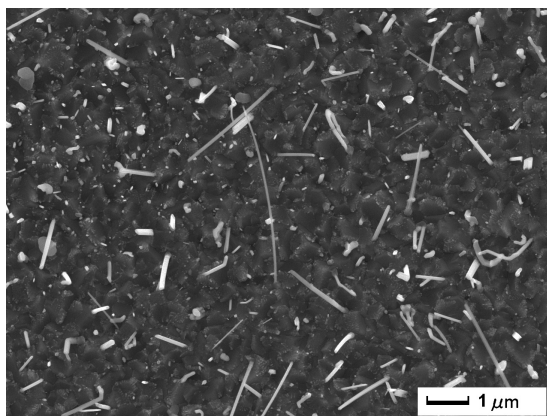


Figure 7.29: AlPb film: ambient atmosphere: - SEM micrograph of sample kept in air at 53% RH for 24 h after deposition

It is clearly visible that only nanoparticles of Pb with similar size of NWs are formed during the sputtering process (fig. 7.28) and these Pb seeds only grow in form of NWs after exposure to the ambient condition (1 bar pressure and 53% RH) for 24 h (fig. 7.29). The Al-Pb film kept in vacuum shows a very low number of NWs with short length (fig. 7.30). Al-Pb films stored in inert gas (Ar) atmosphere (1 bar of pressure

7. SYNTHESIS AND CHARACTERIZATION OF PB NANOWIRES

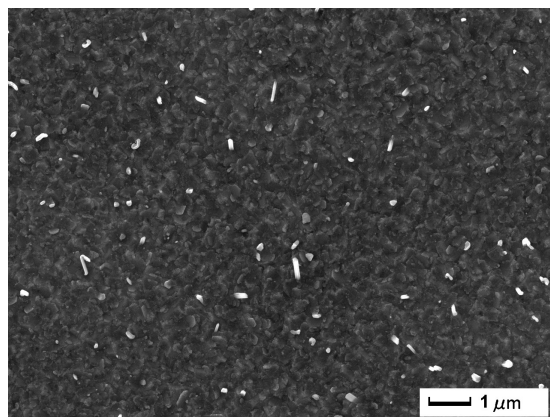


Figure 7.30: AlPb film: low vacuum: - SEM micrograph of sample kept in low vacuum for 24 h after deposition

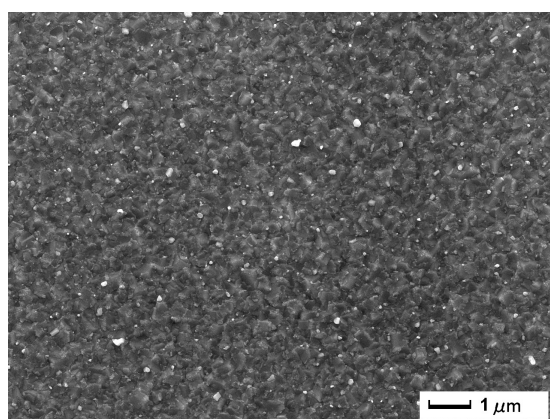


Figure 7.31: AlPb film: argon atmosphere: - SEM micrograph of sample kept in 1 bar of Ar for 24 h after deposition

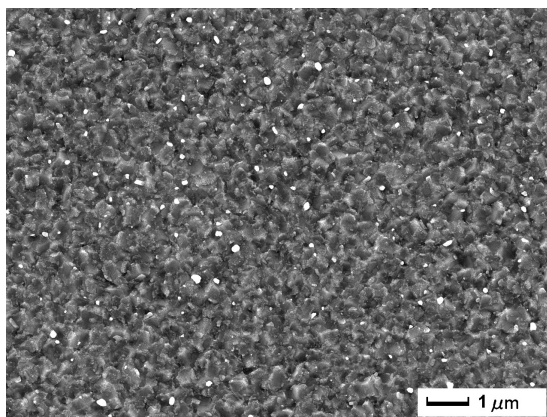


Figure 7.32: AlPb film: oxygen atmosphere: - SEM micrograph of sample kept in 1 bar of O_2 for 24 h after deposition

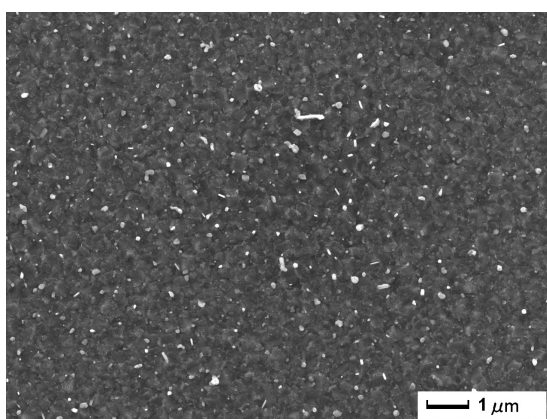


Figure 7.33: AlPb film: annealing in vacuum: - SEM micrograph of sample annealed at $100^\circ C$ for 2 h at low vacuum

7. SYNTHESIS AND CHARACTERIZATION OF PB NANOWIRES

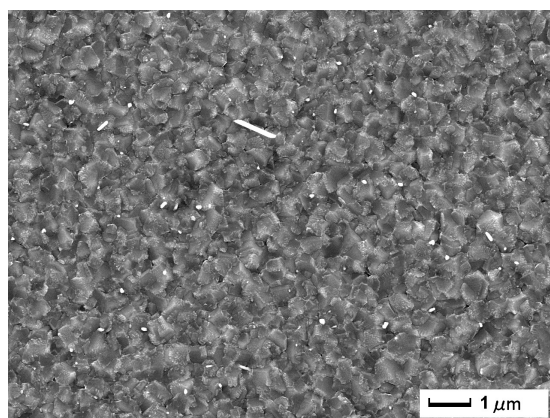


Figure 7.34: AlPb film: dry atmosphere: - SEM micrograph of sample kept in air at 17% RH for 24 h after deposition

for 24 h), showed almost no NWs (fig. 7.31) A few NWs were observed after vacuum-annealing of film at 100°C (fig. 7.33). The Al-Pb film kept in oxygen atmosphere (1 bar pressure for 24h) shows almost no NWs (fig. 7.32) as with samples stored in air at 17% RH (fig. 7.34). Note that water vapor is present in very small quantity in the as-deposited samples because the chamber was evacuated before entering the gas.

7.5 Discussion on different storage conditions

The previous results consistently prove that NWs do not grow during the sputter deposition but they are extruded outside in the ambient atmosphere by the relaxation of stress that could be induced in the film.

We want to focus on the fact that NWs growth occurs only for samples left in the environment where the corrosion is most likely to happen.

When the samples are left in air a layer of protective oxide forms on the surface of the film, as showed by the XPS analysis. To comes out from the surface the NWs have to break this oxide layer. Segregation of Pb atoms to grain boundaries can lead to grain boundary rupture due to temper brittleness, creep embrittlement, stress relief cracking of weldments, hydrogen embrittlement, environmentally assisted fatigue, grain boundary corrosion and some kinds of intergranular stress corrosion cracking [19]. In particular, any environments that can provide hydrogen, such as humid air or salt solution, can lead to stress corrosion cracking of susceptible alloys [20].

Corrosion of aluminium alloys is essentially a microgalvanic process between the phases of the alloy and the matrix alloy [21]. This corrosion is likely to start near areas of exposed base material, where a galvanic element can enhance the corrosion process. The electrochemical corrosion is strongly dependent upon the relative humidity.

In our case the difference in EFM between Pb and Al can lead to localized galvanic corrosion [22] when an oxidizing electrolyte, i.e. water vapor, is present. The rupture of the oxide layer allows the system to release the existing stress.[23]

Indeed without this protective layer the free surface is an effective source and sink of vacancies. The oxide layer prevents the uniform relaxation of the stress over the grain boundary or at the entire film surface. At the same time the oxide layer contributes to the build-up of stress in the film preventing the diffusion of atoms at the surface [22, 24, 25]. Thus the locally confined stress relief permitted by the rupture of the oxide layer allows the continuous growth of NWs supported by the excess energy in the binary immiscible system. Our reported results are in agreement with recent works on growth of Sn whisker in coatings of Sn on Cu [26, 27, 28].

7.6 In-situ NWs growth

We are also able to observe in-situ SEM NWs growth. Al-7at.% Pb film is loaded in the SEM chamber after exposure to air to study the in-situ growth. NWs grew during e-beam irradiation, as shown in the evidenced region of the film surface 7.35.

Figure 7.36 shows the NWs growth during exposure to electron beam at the bottom of the film after detachment from the substrate. It is easy to study the evolution of a single NW (marked by colored circle in the fig. 7.36) on the bottom of the film because of the lower density of NWs with respect to the surface of the film.

We measured the increase of the length of single NW with time, chosen among those having the highest length. The rate of NWs growth under the e-beam irradiation is higher than in air and follows a time-square root law as reported in fig. 7.37. However, after about 25 minutes the growth stops. The line is obtained by fitting the experimental points (symbols) with the equation:

$$length\ of\ NW = (Dt)^{1/2} + L_0 \quad (7.1)$$

7. SYNTHESIS AND CHARACTERIZATION OF PB NANOWIRES

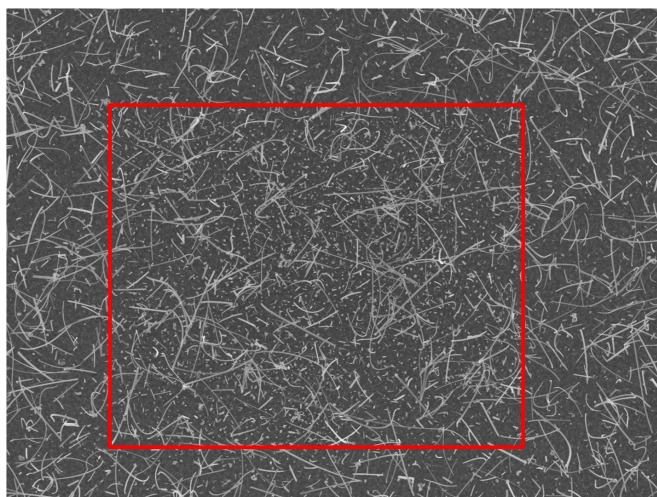


Figure 7.35: E-beam irradiated area of the AIPb films: - the region irradiated by electron beam has been evidenced.

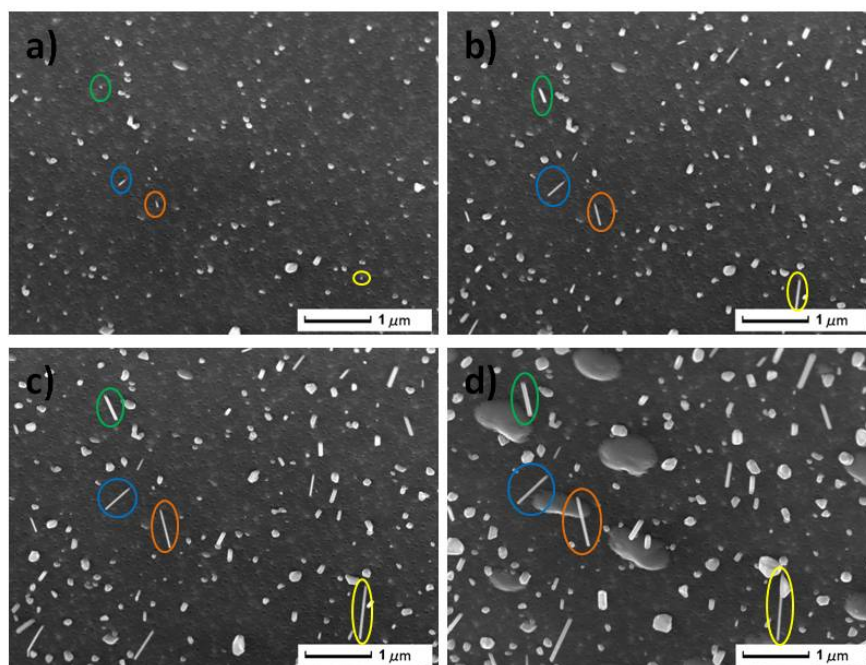


Figure 7.36: In-situ NWs growth - Each color identify a single NWs at time: a)0 sec, b)73 sec, c)266 sec, and d)1241 sec

7.7 Discussion on NWs in-situ SEM growth

The fit reveals that the growth of the NWs follow a square root law, characteristic of diffusion process. The parameter D can be interpreted as the diffusion coefficient of Pb atoms. A second parameter L_0 is needed because the initial value of the length before irradiation is not zero, but the one measured at 0 second. The value of the parameter D , of about $5 \times 10^{-12} (cm^2 \div sec)$, is appropriate to diffusion process in solid state near room temperature, as we will discuss in the next section.

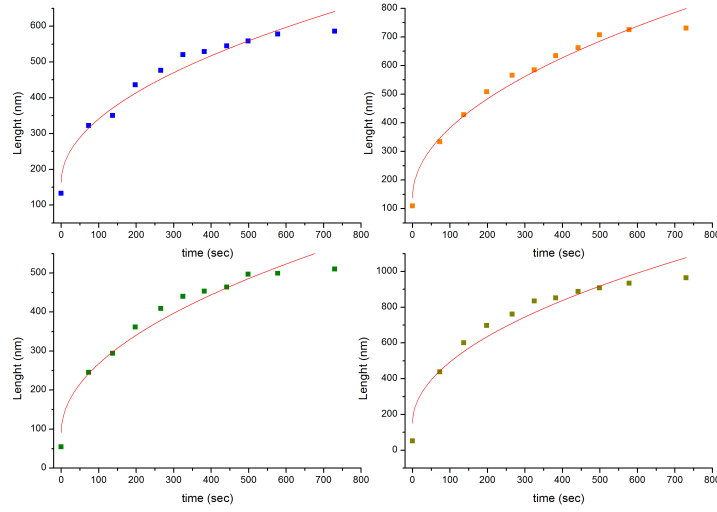


Figure 7.37: Measured length (symbols) of a single NW vs. e-beam irradiation time - Colors are the same used to identify the NWs in fig. 7.36. The line is obtained by fitting the experimental points with equation 7.1

7.7 Discussion on NWs in-situ SEM growth

To try to explain in a consistent framework all the obtained results, we have to look at existing models on NWs growth based on stress mechanisms. In recent year a stress-induced oxidation mechanism has been proposed for NWs growth[29, 30]. According to this theory the driving force is the stress generated by the volume expansion due to the formation of a metal oxide after oxidation in air. The role of O and the associated volume expansion can occur at much different time scale than that for the whisker extrusion[29]. Oxygen adsorbed on the surface can first diffuse along the surface, then

7. SYNTHESIS AND CHARACTERIZATION OF PB NANOWIRES

reaching the bulk of the film moving through the Al grain boundaries. This means that oxidation can be the reason for stresses generation [29, 30].

The growth of the NWs into a SEM chamber is explained by the presence of residual O_2 . However in our case the NWs grew during the SEM analysis have length equal or greater than the existing ones on the surface of the film. If the oxygen diffusion was the cause for the stress generation, than the NWs grew in-situ should be smaller than that grew in air because in SEM chamber the amount of oxygen is clearly lower than in atmosphere. In addition the growth of NWs obeys to a $(time)^{1/2}$ law (eq. 7.1) that suggests atomic diffusion process. Indeed, the value of the diffusion coefficient D is of the order of $10^{-11}cm^2/sec$, a value appropriate for atomic diffusion in solid state at temperature not much greater than the ambient one.

Considering the above points, the following mechanism of NWs growth is suggested: Pb initially dispersed inside the Al matrix during co-sputtering deposition process, possibly segregates (a diffusion process) at the Al grain boundaries to support the growth of NWs that are extruded through stress relaxation if the surface oxide is broken by external forces (electron-beam or mechanism like corrosion as suggested in [31]). Electron beam can break the oxide layer thus providing a free surface to relieve stress that increases the growth rate of NWs.

Indeed, under electron irradiation, along with heating effects produced by the e-beam (energy of 15 keV), oxide decomposition is favoured by electronic sputtering. Electron-stimulated oxygen desorption has already been observed for aluminum oxides and lead oxide under electron beam irradiation [32, 33, 34]. Moreover electron beam irradiation can enhance the Pb diffusion speed [10].

7.8 Conclusion

A thermodynamically driven segregation lead to separation of Al and Pb by the diffusion of Pb possibly along the grain boundaries of the polycrystalline aluminum film during deposition. As soon as the film is exposed to environment atmosphere a protective oxide layer forms on the surface preventing further diffusion of Pb to relax stress but rather increasing the buildup of stress. Moisture in air causes a localized galvanic corrosion at the Al-Pb interface able to locally break the oxide layer leading to stress relief through free surface. Figure 7.38 summarizes the relevant features of the Pb-NWs

growth we have addressed. The diffusion of almost all Pb atoms from bulk to NWs exhausts the driving force for NWs growth that so stops. In vacuum, the oxide layer can be broken by the electron beam of a SEM thus providing a free surface to relieve stress that increases the growth rate of NWs.

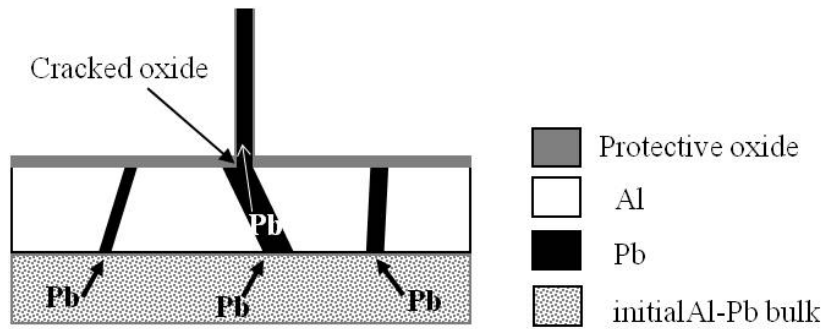


Figure 7.38: Schematic representation of NWs growth -

REFERENCES

References

- [1] Y. Sun, B. Gates, B. Mayers, and Y. Xia. *Nano Lett.*, 2:165, 2002. 119
- [2] S. Michotte, L. Piraux, S. Dubois, F. Paillou, G. Stenuit, and J. Govaerts. *Physica C*, 377:267, 2002. 119
- [3] R. Inguanta, E. Rinaldo, S. Piazza, and C. Sunseri. *Electrochem. Solid-State Lett.*, 13:K1, 2010. 119
- [4] H.S. Awad and N.A. Galwa. *Chemosphere*, 61:1327, 2005. 119
- [5] Z.L. Xiao, Catherine Y. Han, U. Welp, H.H. Wang, W.K. Kwok, G.A. Willing, J.M. Hiller, R.E. Cook, D.J. Miller, and G.W. Crabtree. *Nano Lett.*, 2:1293, 2002. 119
- [6] G. Yi and W. Schwarzachera. *Appl. Phys. Lett.*, 74:1746, 1999. 119
- [7] Y. Wang, X. Jiang, T. Herricks, and Y. Xia. *J. Phys. Chem. B*, 108:8631, 2004. 119
- [8] X. Xiao, A.K. Sachdev, D. Haddad, Y. Li, B.W. Sheldon, and S.K. Soni. *Appl. Phys. Lett.*, 97:141904, 2010. 119, 134
- [9] Y.-T. Cheng, A.M. Weiner, C.A. Wong, M.P. Balogh, and M.J. Lukitsch. *Appl. Phys. Lett.*, 81:3248, 2002. 119, 122, 135
- [10] Y. Cheng, X.D. Han, X.Q. Liu, K. Zheng, Z. Zhang, T. Zhang, Z.T. Song, B. Liu, and S.L. Feng. *Appl. Phys. Lett.*, 93:183113, 2008. 119, 135, 144
- [11] I. Olefjord, H.J. Mathieu, and P. Marcus. *Surf. Interface Anal.*, 15:681, 1990. 133
- [12] K. Domen and T.J. Chuang. *J. Chem. Phys.*, 90:3318, 1989. 133
- [13] K.S. Kim, T.J. O'Leary, and N. Winograd. *Anal. Chem.*, 45:2214, 1973. 133
- [14] H.S. Chou, J.C. Huang, and L.W. Chang. *Surf. Coat. Technol.*, 205:587, 2010. 136
- [15] H.-D. Männling, D.S. Patil, K. Moto, M. Jilek, and S. Veprek. *Surf. Coat. Technol.*, 146 - 147:263, 2001. 136

-
- [16] Hondros and M.P. Seah. *Int. Met. Rev.*, 22:262, 1977. 136
- [17] C.C. Koch. *Nanostructured Materials: Processing, Properties and Applications*, Second Ed. William Andrews Publishing:Norwich NY, 2007. 136
- [18] K.N. Tu, Chih Chen, and Albert T. Wu. *J. Mater. Sci: Mater. Electron*, 18:269, 2007. 136
- [19] M.P. Seah. *J. Catal.*, 57:450, 1979. 140
- [20] Guides to Good Practice in Corrosion Control. *National Physical Laboratory*, <http://www.npl.co.uk/upload/pdf/stress.pdf>. 140
- [21] K. Nisancioglu. Proceedings of icaa3 trondheim. *NTH and SINTE*, 3:239, 1992. 141
- [22] J. Osenbach, R.L. Shook, B.T. Vaccaro, B.D. Potteigner, A.A. Amin, K.N. Hooghan, P. Suratkar, and P. Ruengsinsub. *IEEE Trans. Electron. Packag. Manuf.*, 28:36, 2005. 141
- [23] J.W. Osenbach, J.M. DeLucca, B.D. Potteiger, A. Amin, R.L. Shook, and F.A. Baiocchi. *IEEE Trans. Electron. Packag. Manuf.*, 30:23, 2007. 141
- [24] K.N. Subramanian. *Lead-Free Electronic Solders*, first ed. Springer-Verlag, 2007. 141
- [25] E. Chason, N. Jadhav, W.L. Chan, L. Reinbold, and K.S. Kumar. *Appl. Phys. Lett.*, 92:171901, 2008. 141
- [26] J. Zhang and J. Zhang. *Appl. Mech. Mater.*, 44:2691, 2011. 141
- [27] B. Illés, B. Horváth, and G. Harsányi. *Surf. Coat. Technol.*, 205:2262, 2010. 141
- [28] C.C. Wei, P.C. Liu, and C. Chen. *J. Appl. Phys.*, 102:043521, 2007. 141
- [29] M. W. Barsoum, E. N. Hoffman, R. D. Doherty, S. Gupta, and A. Zavaliangos. *Phys. Rev. Lett.*, 93:206104, 2004. 143, 144
- [30] E.N. Hoffman, M.W Barsoum, W. Wang, R.D. Doherty, and A. Zavaliangos. Proceedings of the fifty-first iee holm conference on electrical contacts. *Chicago IL*, page 121, 2005. 143, 144

REFERENCES

- [31] J. W. Osenbach, J. M. DeLucca, B. D. Potteiger, A. Amin, and F. A. Baiocchi. *J Mater Sci: Mater Electron*, 18:283, 2007. 144
- [32] I. Vandendael, T. Hauffman, Y. Van Ingelgem, and H. Terryn A. Hubin. *Surf. Interface Anal.*, 42:897, 2010. 144
- [33] N. Sergeev, V.K. Kumykov, and V.A. Sozaev. *Bull. Russ. Acad. Sci. Phys.*, 72: 1120, 2008. 144
- [34] Y.C. Choi, J. Kim, and S.D. Bu. *J. Korean Phys. Soc.*, 51:2045, 2007. 144

Concluding remarks and perspectives

Because of their appealing properties, nanostructures have attracted much attention in the field of catalysis. In particular we were interested in catalysts to be used for hydrogen production and wastewater treatment. Our main aims have been:

- i) to understand the role of deposition parameters in PLD technique in order to improve the properties of Co-B and Co oxide NPs to be used as catalyst for hydrogen production from chemical hydride and for photodegradation of methylene blue solution respectively
- ii) to improve the properties of TiO_2 thin films produced by R.F. sputtering deposition, in order to obtain a better photocatalytic activity when using films as anode in a photo-electrochemical cell
- iii) to investigate new simple and cheap technique to obtain nanostructures.

We synthesized thin films of C-supported Co-B nanoparticles by PLD to be used as catalysts in hydrolysis of AB and SBH to produce H_2 . Co NPs obtained in a single-step deposition are well-dispersed and partially embedded within B-based film matrix. The small size of Co NPs is a benefit for catalytic activity and the B film around the NPs prevents them to coalesce. Moreover, by just varying the laser fluence in PLD it was possible to tune both size and density of Co NPs. Rough C-films, to serve as substrate for Co-B NPs deposition, were also prepared by PLD. Measurement on hydrogen production from AB and SBH using the C-supported Co-B films was performed showed that the deposition parameters have actually a great influence on catalytic activity.

8. CONCLUDING REMARKS AND PERSPECTIVES

We deposited Cobalt oxide NPs by PLD in oxygen atmosphere. Several deposition parameters have been varied in order to tailor the properties of the deposited NPs. Core/shell cobalt oxide NPs has been formed in a single step process without post annealing treatment. Dependence of NPs crystalline phase over deposition conditions has been investigated and discussed. Co_3O_4 was used as catalyst for photodegradation of organic dyes in waste water treatment application because of its thermodynamic stability and desired catalyst properties. Experiments have been performed to test the photocatalytic properties of the synthesized NPs for degradation of methylene blue solution under light irradiation.

Multilayer ITO/ TiO_2 -doped-Cr thin films has been produced by R.F. sputtering deposition. The doping of TiO_2 with Cr (9 at.%) results in an increase of the optical absorption efficiency with respect to undoped TiO_2 . However, in photo-electrochemical cell, negligible photocurrent was measured with a single bilayer ITO/Cr-doped- TiO_2 , because of the high recombination rate of the photo-generated charges. To reduce the charge recombination rate, multilayer films with different numbers of ITO/Cr-doped- TiO_2 have been prepared. These multilayer structures significantly contributed to reduce the charge recombination rates.

Pb NWs were grown in a single step by co-sputtering of an Al bulk target partially covered with Pb-metal pieces on its surface and without using extra catalyst. We proposed a phenomenological description of the NWs growth process. The driving force for growth of NWs is provided by compressive stress induced in these composite thin films during RF-sputtering co-deposition. Here indeed Pb segregates through atomic diffusion process at the grain boundary of Al to support the growth of the extruded NWs. The presence of most air is needful to initiate the NWs growth. In the film exposed to environment atmosphere a protective oxide layer forms on the surface, thus preventing the Pb atoms to reach the surface of the films and so increasing the stress in the deposited film. Moisture in air or electron beam in vacuum are able to locally break the oxide layer leading to stress relief through free surface thus permitting NWs growth. Experiments are in progress to obtain spontaneous growth of other soft metal NWs by Al-soft metal co-sputtering deposition. A first result has already been obtained using Sn instead of Pb. Sn NWs are observed to growth from the surface of the deposited Al-Sn films, however the density of Sn NWs on the surface is lower than

for Pb. Optimization of the deposition parameters is needed to improve the extrusion of Sn NWs. These NWs are intended to enhance H_2 production in electrolyzers.

8. CONCLUDING REMARKS AND PERSPECTIVES

Appendix A

R.F. Sputtering deposition

The deposition of thin films by R.F. sputtering follows four steps:

- evaporation of atoms from the target
- flight of the atoms from the target to the substrate
- condensation of atoms on the substrate
- nucleation and film growth

Sputtering occurs whenever any particle strikes a surface with enough energy to dislodge an atom from the surface. The sputter yield Y is just the ratio of the number of emitted particles per incident particle. The sputtering process is shown schematically in Fig. 1. The incident particle impacts the surface or near-surface atoms of the solid with sufficient energy to break bonds and dislodge atoms. If, during this process, one or more atoms are removed from the solid, they are considered to be sputtered atoms. Incident particle energies of hundreds eV, needed for sputtering, are much easier to arrange for ions as compared to neutral atoms. Ions respond to electric fields and potentials and it is very straightforward to configure an acceleration voltage of a few hundred volts within a vacuum chamber.

Sputtering can be described considering four general energy ranges, from near the binding energy to many MeV.

Very low energies ($0 < E < 20 \div 50eV$) the impinging ion has an energy too low to dislodge and emit atoms from the target, so $Y=0$.

A. R.F. SPUTTERING DEPOSITION

Knock-on energy regime ($50\text{eV} < E < 1\text{KeV}$) the incident ion generates a collision cascade. This process is based on momentum and energy transfer from the incident ion to one or more atoms on the surface. The surface atoms then collide with sub-surface atoms with consequent momentum and energy transfer. By collision cascades atoms can transfer a momentum perpendicular to the target surface. Atoms in the cascade which have acquired a momentum and an energy to get out from the target, may reach the substrate.

High energies regime ($1\text{KeV} < E < 10\text{KeV}$) there is a high density of collision cascades involving a great number of atomic layers

Ion implantation regime ($E > 10\text{KeV}$) the incident ions travel deep into the target before causing a significant number of collisional events. The energy is transferred to the atoms in the sub-surface, that are not able to exit from the target.

The kinetic energy distribution of sputtered atoms peaks at a few eV to 10 eV and then decreases as $1/E^2$. The angular emission distribution for sputtered atoms is often described as a cosine distribution.

In sputtering deposition the ions are generate in a plasma, formed by ionization process of a neutral gas. The simplest sputtering system consist in an anode (substrate) and a cathode (target) loaded into a vacuum chamber (see fig. A.1).

Argon gas is injected into the R.F. chamber, where it is weakly ionized by cosmic radiation. When a high potential difference (of the order of 100V) is applied between the target and the substrate, the electrons in the gas accelerate and ionize neutral Ar atoms. The as formed ions are accelerated and collide with the other atoms and ions in the chamber, giving rise to emission of secondary electrons. The secondary electrons are again accelerated by the applied voltage, and in turn ionize others atoms, so that the plasma is self-sustained. The sputtered ions can ballistically or diffusively arrive at the substrate (depending on the gas pressure inside the chamber) and condense there, forming the film.

For insulating target or for target having oxide layer on the surface, the Ar^+ ions may accumulate on the target surface, making it positively charged. The other Ar^+ in the plasma are thus repelled by Coulomb repulsion and Y abruptly decreases.

To avoid this problem, instead of applying a DC voltage to the cathode, a voltage oscillating at radio frequency (RF) is applied. In a R.F. sputtering the power supply

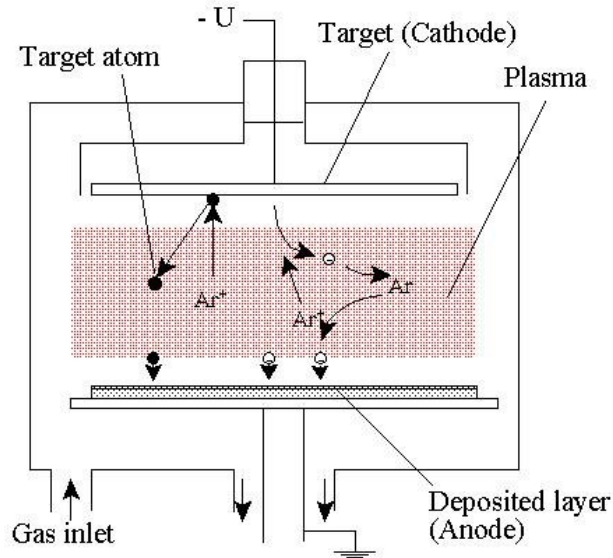


Figure A.1: Schematic of the sputtering deposition apparatus -

is operated at high frequency. The most common frequency is 13.56 MHz. In this way, for a small part of the rf cycle, the cathode and anode are electrically reversed. This eliminates charge buildup on an insulating surface, allowing insulators to be sputtered or metals to be sputtered in reactive environments. The rf diode system requires impedance matching to operate most efficiently. This matching network, often located in a matchbox immediately adjacent to the vacuum system, helps to optimize the transfer of power from the power supply which is designed to see a load of 50 ohms.

Magnetron can be used to generate plasma more efficiently. A series of magnets with alternating polarity are attached to the back side of the target in a circular fashion. The magnets create curved magnetic field lines which confine the secondary electrons to them. The highly concentrated electron gas collides with the ions near the target and create a denser plasma without the need for higher pressures.

A. R.F. SPUTTERING DEPOSITION

Appendix B

Scanning electron microscopy

Scanning Electron Microscopy (SEM) is a technique where a focused beam of electrons strikes a sample giving rise to several signals containing information relative to the sample's surface topography and composition.

The scheme of a SEM is showed in fig. B.1.

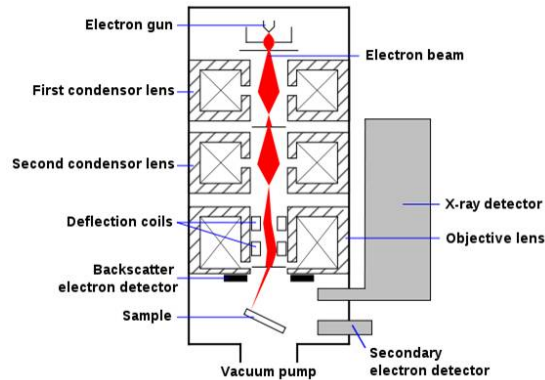


Figure B.1: Schematic diagram of a SEM -

An electron gun produce a beam of electrons with similar energy. This is accelerated and passes through a series of electromagnetic lenses and apertures. These are needed to decrease the diameter of the beam spot from $30\ \mu\text{m}$ to about 30\AA and the value of current from $50\text{--}150\ \mu\text{A}$ to few pA. A final lens deflects the beam in the x and y axes so that it scans in a raster fashion over a rectangular area of the sample surface. When an electron beam hits a sample a large amount of signals are generated coming from reflected electrons, secondary electrons, Auger electrons, transmitted electrons,

B. SCANNING ELECTRON MICROSCOPY

cathodoluminescence and X-rays. The SEM reveals essentially three signals: the secondary electrons, the back-scattered electrons and the X-rays (when a X-ray detector is present).

The secondary electrons (SE) are generated from inelastic collision between the electrons in the beam and the atomic electrons of the sample. The first can transfer to the atomic electrons an amount of energy sufficiency to be ejected from the atoms. They have a low energy, between 5 and 10 eV, so only the electrons produced near the surface can escape from the samples. The escaped electrons are called SE. The SE give information on the material topography. The main cause of the image contrast is the existing angle between the incident beam and the surface.

Backscattering electrons (BSEs) are produced by the collision of the electrons in the beam with the nucleus of the atoms in the specimen. The scattering can be considered elastic so the electrons (BSEs) exit from the surface with an high energy. BSEs contains information on chemical composition of the elements in the specimen. The number of BSEs increase with the atomic number Z of the atoms, so a material with an high Z will appear more bright on the image than a material having a lower Z .

X-rays arise from two different mechanism: Bremsstrahlung and fluorescence. In the first case the incident electrons, decelerated by the electric field of the atoms, emit X-rays. These will have a continuous spectrum, not useful for the purpose of the analysis. In the second case an electron of the beam is inelastically scattered by an inner-shell electron in the specimen. The latter acquires enough energy to escape from the atoms, leaving a vacancy in its inner shell. The other atomic electrons than fill that vacancy produce the emission of an X-rays. The energy of the emitted X-rays is characteristic for each element and each atomic transition of the element. An energy-dispersive spectrometer (EDS) in the SEM chamber measures the number and the energy of the emitted X-rays. The EDS spectrum contains information on the elemental composition of the sample and on the concentration of each element in the specimen.

Appendix C

Transmission electron microscopy

Transmission Electron Microscopy (TEM) is a technique where an electron beam interacts and passes through a specimen. TEM exploits three different interactions of electron beam-specimen: unscattered electrons (transmitted beam), elastically scattered electrons (diffracted beam) and inelastically scattered electrons. When incident electrons are transmitted through the thin specimen without any interaction occurring inside the specimen, then the beam of these electrons is called transmitted. The transmission of unscattered electrons is inversely proportional to the specimen thickness. Areas of the specimen that are thicker will have fewer transmitted unscattered electrons and so will appear darker than the thinner areas. Another part of the incident electrons, are elastically scattered by atoms in the sample. These scattered electrons are then transmitted through the remaining portions of the specimen. The electron scattering follows the Bragg's law:

$$2d\sin\theta = n\lambda$$

where λ is the wavelength of the rays, θ is the angle between the incident rays and the surface of the crystal and d is the spacing between layers of atoms. All incident electrons have the same energy (thus wavelength) and enter the specimen normal to its surface. So all the electrons scattered by the same atomic spacing will be scattered by the same angle. The as formed scattering pattern gives information about the orientation, atomic arrangements and phases present in the area being examined. Each spot corresponds to a specific atomic plane.

Finally, electrons can be inelastically scattered from the atoms in the sample. These electrons are then transmitted through the rest of the specimen. Inelastically scattered

C. TRANSMISSION ELECTRON MICROSCOPY

electrons can be utilized in two ways: Electron Energy Loss Spectroscopy (EELS) and Kikuchi Bands. Elemental composition and atomic bonding state can be determined by analyzing the energy with the spectroscope attached under the electron microscope (Electron Energy Loss Spectroscopy). It is possible to select a part of the enlarged electron microscopic image and so analyze a very small region of the sample. Moreover, element distribution in specimen can be visualized. Kikuchi lines appear in transmission electron diffraction patterns of relatively thick crystals due to Bragg reflection of the inelastically scattered electrons. They are alternating light and dark lines that are related to atomic spacings in the specimen.

A very simplified geometry of TEM is shown in figure C.1.

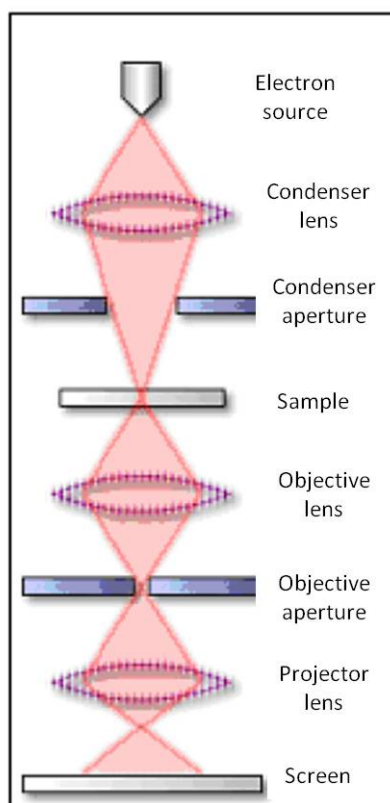


Figure C.1: Schematic diagram of a TEM -

The electron gun, formed by an electron source and an electron-accelerating chamber, produces a beam of electrons whose kinetic energy is typically between 100 and 300 keV. The electron beam is confined by the two condenser lenses, passes the con-

denser aperture and strikes the sample surface. Parts of the electrons are transmitted depending upon the thickness and electron transparency of the specimen.

The transmitted electrons pass through the objective lens. The objective lens forms the image display. Diffraction pattern and image are both formed in the imaging process (see fig. C.2). The apertures following the objective lens, the objective and selected area aperture are used to choose the elastically scattered electrons that will form the image of the microscope (see fig. C.2). The intermediate lens is then focused on either the image plane (for the image), or the back focal plane (for the diffraction pattern). A series of projector lenses are then used to magnify the image formed by the intermediate lens onto a viewing screen (a fluorescent screen or a monitor).

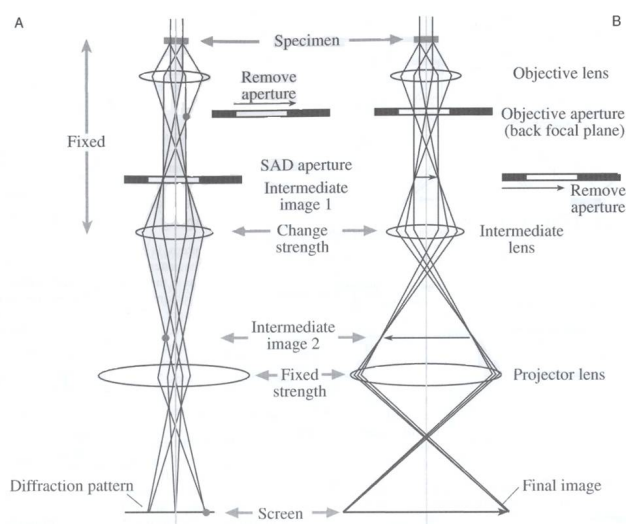


Figure C.2: The two principal modes of TEM operation -

Different types of images are obtained in TEM by both using the apertures properly and the different types of electrons. Scattered electrons give the diffraction patterns, while if the unscattered beam is selected, we obtain the Bright Field (BF) image. Dark Field Images are attained if diffracted beams are selected by the objective aperture. Analysis can be done with EDX (Energy Dispersive X-ray), EELS (Electron Energy Loss Spectrum), EFTEM (Energy Filtered Transmission Electron Microscopy), etc data.

In the BF mode the image results from a weakening of the direct beam by its interaction with the sample. Therefore, mass-thickness and diffraction contrast contribute to image formation. Mass-thickness contrast originates elastic scattering of electrons.

C. TRANSMISSION ELECTRON MICROSCOPY

Elements with higher atomic number Z will scatter more electrons than low- Z elements. Therefore fewer electrons from the dark region fall onto the screen, so the region appears darker in a Bright Field image. As the thickness of the specimen increases the elastic scattering and so the contrast increase. However a too thick a specimen gives too much inelastic scattering reducing the resolution. The diffraction process may be thought of as reflection by a set of crystal planes oriented at a specific Bragg angle relative to the incident beam, as described before. In BF mode the diffracted electrons leaving the lower surface of a crystalline specimen are intercepted by the objective aperture and prevented from contributing to the image.

Whereas conventional BF-TEM usually utilizes only the central electron beam, the phase contrast method relies on the interference of the diffracted beams with the direct beam. Phase contrast imaging is the basis for the so called high-resolution TEM (HRTEM). Phase contrast images are formed by removing the objective aperture or by using a very large objective aperture, so that both the transmitted beam and the diffracted ones contribute to the image. The electrons leaving the bottom surface of a thin electron microscope specimen have small phase differences arising from scattering in the specimen. When they recombine to form the image the existing phase differences are converted into intensity differences in the image. Phase contrast imaging can allow for resolutions of less than 10 \AA that is important in lattice resolution studies and investigations of the early stages of short-range order and amorphous materials.

Electron energy loss spectrometry (EELS) measures the change in kinetic energy of electrons after they have interacted with a specimen. Because these electrons are responsible for creating (in an inelastic collision) the inner-shell vacancies that give rise to characteristic X-rays (and Auger) electrons, they carry atomic-number information in the form of the amount of energy that they have transferred to the specimen. It provides information such as the interacting atoms, chemical bonding and valence and conduction band electronic properties. EELS is a very powerful technique capable of providing chemical and electronic information from particular areas in the sample combining it with a scanning transmission electron microscope (STEM).

When a primary electron enters a TEM it has the probability of being scattered inelastically by an inner-shell electron in the sample, causing the latter to undergo a transition to a higher-energy orbit and leaving the atom with an electron vacancy in its inner shell. One of the other atomic electrons then fills the formed vacancy making

a downward transition from a higher energy level. In this de-excitation process X-ray is emitted with the amount of an energy equal to the difference between two shells. Each element has a unique atomic structure allowing unique set of peaks on its X-ray spectrum. An EDS (as for SEM) detector can be loaded in TEM to measure the number and energy of the X-rays emitted from a specimen and thus obtain elemental composition information.

TEM can be equipped with a scanning TEM (STEM) attachment. In STEM, a tiny, convergent electron beam is scanned over a defined area of the sample. The peculiarity of STEM is that the different signals generated from the same sample area can be collected simultaneously giving complementary information about the sample. The rastering of the beam across the sample makes these microscopes suitable for analysis techniques such as mapping by energy dispersive X-ray (EDS) spectroscopy and electron energy loss spectroscopy (EELS).

C. TRANSMISSION ELECTRON MICROSCOPY

Appendix D

X-ray Photoelectron Spectroscopy

XPS (X-ray Photoelectron Spectroscopy) is a surface-sensitive analysis technique. XPS gives quantitative information about the elemental composition of the surface of all kinds of solid material (insulators, conductors, polymers). XPS spectra are obtained by irradiating a material with a monochromatic X-rays beam (of energy around 1.5 keV) while simultaneously measuring the kinetic energy and number of electrons that escape from the first surface layer of the material being analyzed. The electrons ejected from the surface are energy filtered via a hemispherical analyser (HSA) before the intensity for a defined energy is recorded by a detector. The sample analysis is conducted in a vacuum chamber, under the best vacuum conditions achievable.

Bombarding a sample in vacuum with X-rays gives rise to the emission of electrons. If monochromatic X-rays are used the energy of the emitted electrons K_e is given by:

$$K_e = h\nu - B_e - \phi$$

where $h\nu$ is the photon energy of X-rays beam, B_e the binding energy of the atomic orbital from which the electron originates and ϕ is the work function. In XPS the photon is absorbed by an atom in a molecule or solid, leading to ionization and the emission of a core (inner shell) electron. By measuring the number of these electrons as a function of kinetic (or binding) energy, an XPS spectrum is obtained. The binding energies are characteristic of specific electron orbitals in specific atoms, so the presence of peaks at particular energies indicates the presence of a specific element. However the exact binding energy of an electron depends also on the chemical environment of the

D. X-RAY PHOTOELECTRON SPECTROSCOPY

atoms. Changes local chemical environment produce small shifts in the peak positions in the spectrum that is called chemical shifts . So the position of the peaks has to be interpreted to obtain information on the chemical state of the elements in the sample. The number of detected electrons is a measure for the elemental concentration. To generate atomic percentage values, peak areas are divided by the relative element sensitivity factors (usually tabulated and dependent on the analyzer used) and normalized over all of the elements detected.

In the case of conducting samples, for which the detected electron energies can be referenced to the Fermi energy of the spectrometer, an absolute energy scale can be established, thus aiding the identification of species. However, for non-conducting samples the problem of energy calibration is significant. Electrons leaving the sample surface cause a potential difference to exist between the sample and the spectrometer resulting in a retarding field acting on the electrons escaping the surface. Without redress, the consequence can be peaks shifted in energy. Charge compensation designed to replace the electrons emitted from the sample is used to reduce the influence of sample charging on insulating materials, but nevertheless identification of chemical state based on peak positions requires careful analysis.

Some of the photoinduced electrons travel out from the surface without losing any energy, while some of them lose energy owing to inelastic collisions. For this reason XPS spectra show a characteristic background. The shape of the spectrum background or baseline is affected by inelastic energy loss processes, secondary electrons and nearby peaks. A reasonable approximation is essential for a qualitative and quantitative analysis of XPS data especially if several components interfere in one spectrum. In many cases the Shirley model turned out to be a successful approximation. The analytical expression for the Shirley background is:

$$U(E) = \int_E^{\infty} F(E') dE' + c$$

where $U(E)$ is the background function, E is the kinetic energy of the spectra and $F(E)$ is the primary function resulting from the experimentally obtained function $M(E)$ and $U(E)$ as $F(E) = M(E)U(E)$.